Low-Noise AlInAsSb Avalanche Photodiodes

A Dissertation

Presented to

the faculty of the School of Engineering and Applied Science

University of Virginia

---

in partial fulfillment
of the requirements for the degree

Doctor of Philosophy

by

Madison Elizabeth Woodson

August 2017

APPROVAL SHEET

This Dissertation
is submitted in partial fulfillment of the requirements
for the degree of
Doctor of Philosophy

Author Signature: _____

This Dissertation has been read and approved by the examining committee:

Advisor: Joe C. Campbell _____

Committee Member: Andreas Beling _____

Committee Member: Archie Holmes, Jr. _____

Committee Member: Steve Bowers _____

Committee Member: Patrick Hopkins _____

Committee Member: _____

Accepted for the School of Engineering and Applied Science:

Craig H. Benson, School of Engineering and Applied Science

August 2017

Acknowledgements

I would like to thank, first and foremost, Professor Joe C. Campbell for his continuous support and acumen, for encouraging me to excel beyond what I thought I was capable, and for his stories that offered solace and guidance along the way.

Besides my advisor, I would like to express my gratitude to the rest of my committee for their thoughtful and incisive questions that pushed me to delve to greater depths in my research. I would also like to thank Dr. Malathi Veeraraghavan, whose kindness and wisdom kindled a confidence and drive in me that I could not have succeeded without.

I am indebted to my entire research group and our colleagues at the University of Texas, for their hard work, insight, and collaboration, but most of all to Dr. Min Ren, for being such an approachable and helpful mentor and friend, for answering even my most naïve questions with a smile, and for never complaining when I borrowed his books without asking.

I would like to thank Tom Rodgers, my high school physics teacher, for instilling in me a passion for a field which has humbled me ever since and for teaching me the quiet élan that comes only from climbing a mountain you were once too weak to summit.

Finally, of course, I am grateful for the unwavering support and encouragement of my family and friends, for all their help in keeping me going, and for shaping my ambition and curiosity.

Abstract

Avalanche photodiodes (APDs) have been used for a wide range of commercial, military, and research applications in realms ranging from optical communications to imaging to single photon detection. Their primary advantage relative to p-i-n photodiodes is that the APD's gain can provide higher sensitivity, at the cost of additional noise. This excess noise motivates the study of low noise materials, as well as structures with inherently lower noise.

My studies of the $Al_xIn_{1-x}As_ySb_{1-y}$ materials system began with an investigation into an impact ionization engineering device called a staircase photodiode, in collaboration with students at the University of Texas at Austin, who recently developed a process for growing the materials system $Al_xIn_{1-x}As_ySb_{1-y}$ through molecular beam epitaxy (MBE). This staircase structure was designed alongside a control structure composed of a simple, homojunction photodiode made from the $Al_{0.7}In_{0.3}As_{0.3}Sb_{0.7}$ material. With successful, low-noise results from the staircase photodiode, I was motivated to investigate the noise properties of the control structure. When the control showed low noise as well, we expanded our studies into homojunction APDs composed of varying aluminum concentrations of $Al_xIn_{1-x}As_ySb_{1-y}$. The results of these homojunction APDs gave low noise and low dark current for some devices, while other devices exhibited absorption at longer wavelengths with higher dark current. We used the information from the homojunction studies to design and fabricate an SACM APD, which uses one material layer for absorption and another for multiplication. This helped us achieve a low-noise, low dark current APD that can absorb at telecommunication wavelengths (1.3 μm to 1.6 μm). Other studies branched off these, including investigations into multi-step staircase structures and characteristics of digital alloy material APDs versus random alloy material APDs.

In this dissertation, I demonstrate the efficacy of the $Al_xIn_{1-x}As_ySb_{1-y}$ materials system, for use in low-noise APDs. This materials system offers low noise materials for efficient carrier multiplication, as well as narrow bandgap materials which can absorb out to communications wavelengths. The material has a direct bandgap up to 80% Al concentration, allowing for shorter absorption regions and thus higher bandwidths.

Glossary of Terms

α	Absorption coefficient
α	Electron ionization coefficient
APD	Avalanche Photodiode
β	Hole ionization coefficient
B	Bandwidth
BOE	Buffered Oxide Etch
C	Capacitance
d	Depletion width
d	Device diameter
DUT	Device Under Test
E	Energy

	E_g	Direct energy bandgap
	E_{the}	Ionization threshold energy, electrons
	E_{thh}	Ionization threshold energy, holes
	E_{Hthe}	Hard ionization threshold energy, electrons
	E_{Hthh}	Hard ionization threshold energy, holes
	E_p	Phonon energy
	E_C	Conduction band energy
	E_V	Valence band energy

SACM APD	Separate Absorption, Charge, and Multiplication Avalanche Photodiode
ε_0	Permittivity of free space
ε_r	Relative permittivity
F(M)	Excess noise factor
GBP	Gain-Bandwidth Product
GSG	Ground-Signal-Ground
h	Planck constant
$\hbar$	Reduced Planck constant
I	Current

ICP	Inductive Coupled Plasma	
k	Boltzmann constant	
k	Impact ionization ratio, k-factor, k-value	
	I_{BG}	Current generated by background illumination
	I_{dark}	Dark Current
	I_{DM}	Component of dark current multiplied through impact ionization
	I_p	Photocurrent
	I_{p0}	Primary photocurrent
	I_{total}	Total current
LIA	Lock-in Amplifier	
LIDAR	Light Detection And Ranging	
λ	Wavelength	
M	Multiplication gain	
m^*	Effective electron mass	
μ	Mobility	
MBE	Molecular Beam Epitaxy	
MC	Monte Carlo	
ML	Monolayer	
N	Noise power	
	N_d	Dark noise power
	N_p	Photo noise power
	N_{p0}	Photo noise power at unity gain
	N_t	Total noise power
NFM	Noise Figure Meter	
n	Refractive index	
η	External quantum efficiency	
P	Input optical power	
q	Elementary charge	
QE	Quantum Efficiency	
R	Resistance	
	$R_{contact}$	Contact resistance

	R_{eq}	Equivalent resistance
	R_L	Load resistance
	R_S	Series resistance
	R_{sheet}	Sheet resistance
$\mathcal{R}$		Reflectance
R		Responsivity
r		Device radius
σ		Conductivity
RIE		Reactive-Ion Etching
SIMS		Secondary Ion Mass Spectroscopy
SNR		Signal-to-Noise Ratio
SPAD		Single Photon Avalanche Diode
SSPD		Superconducting Single Photon Detector
T		Temperature
τ		Transit time
TIA		Trans-Impedance Amplifier
TLM		Transmission Line Measurement
V		Voltage
	V_{bi}	Built-in voltage
	V_{bd}	Breakdown voltage
w		Depletion region width or thickness
v_s		Saturation velocity (average of electron and hole)
ν		Frequency

List of Tables and Figures

Contents

Chapter 1 Introduction

1.1. Motivation and State of the Art

At its crux, a photodiode is a semiconductor device that converts an optical signal to an electrical one through the photoelectric effect, in which the absorption of light generates an electron-hole pair. Photodiodes are useful for a wide range of applications, from military to commercial to research. Numerous technologies push for faster, more reliable exchange of data, particularly since the advent of public access to internet in 1993, ballooning data transmission to unprecedented volumes [1] [2].
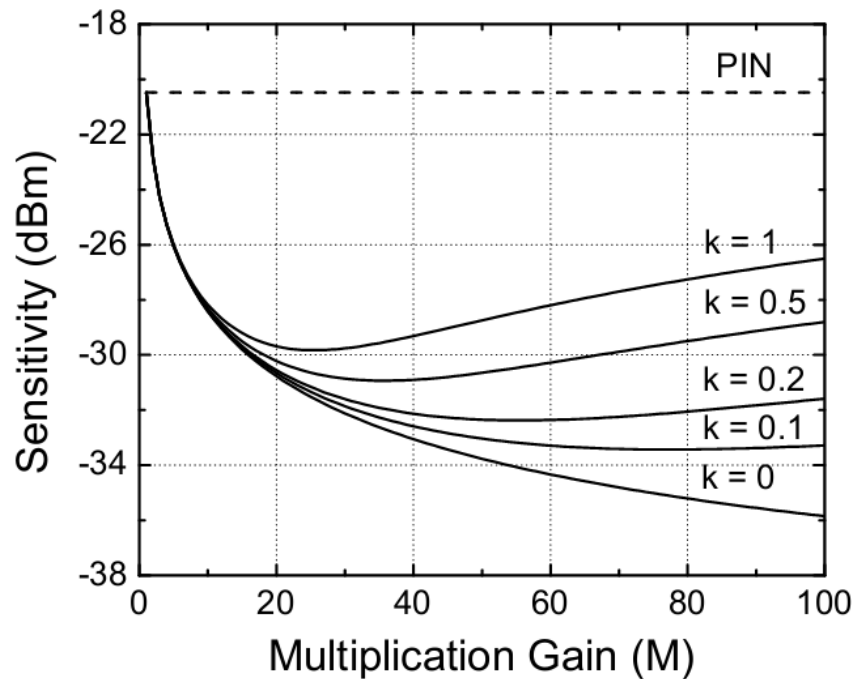
Figure 1-1: Theoretical sensitivity vs. gain for p-i-n photodetector and APDs with various k-values

Avalanche photodiodes are solid-state devices that can be used to both detect and amplify weak optical signals, making them especially useful in fields such as optical communications [3], imaging [4] [5], and single photon detection [6] [7]. Their primary advantage relative to p-i-n photodiodes is that the APD gain can provide higher sensitivity, i.e. detection of lower signal

magnitude, as is shown in Figure 1-1, which illustrates the theoretical sensitivity versus multiplication gain for both a p-i-n photodetector and five APDs with k-values ranging from 0 to 1 [8].

Another competing technology in these areas is the photomultiplier tube (PMT), which gives extremely low-noise gain, but is typically a bulky, fragile, and expensive device that operates at high voltages, and is not solid state. In a PMT, incident light strikes a photocathode in a vacuum, releasing electrons that are multiplied across a series of dynodes and collected at an anode. Through iterations of conventional PMTs, a new photodetector called a micro-PMT has been developed, which provides the same low sensitivity of a conventional PMT, but at a much smaller and lighter scale [9] [10]. Compared to photomultiplier tubes, however, APDs are smaller still than even a micro-PMT, and require lower bias voltage. More importantly, APDs are significantly more robust and less expensive than PMTs [11] [12].

Gain in an avalanche photodiode originates from a process called impact ionization. When a carrier, either an electron or hole, has gained sufficient energy from the electric field of an APD, the carrier has a chance of initiating impact ionization. In this process, the aforementioned carrier has sufficient energy to collide with the lattice, knocking an electron from its bound state and promoting it from the valence band into the conduction band. This process creates a new electron-hole pair: a free electron in the conduction band, and a free hole in the valence band. Now both the original carrier and its respective electron or hole (called the primary electron-hole pair) and the newly-formed (secondary) electron-hole pair continue to gain energy from the electric field, and can undergo further impact ionization events. Subsequent ionization events can result in many carriers that were initiated by a single photon, hence the term "avalanche" photodiode.

Impact ionization is the origin of gain in an APD; it is the reason APDs can achieve higher sensitivity than p-i-n detectors: it provides signal amplification, at the cost of additional ("excess") noise. Ignoring holes for simplicity, if a single electron is injected into the multiplication region of an APD and impact ionizes nine times, ten electrons will be collected, assuming no recombination or other scattering effects. Ten collected electrons for one injected electron gives a ratio, or gain, of ten. However, each injected electron will not necessarily net the same gain; in fact, there is some variance in the gain of individual carriers. Impact ionization is a stochastic process that results in higher shot noise, due to the inherent randomness of avalanche multiplication. This increase in shot noise motivates the study of low-noise materials and structures in order to improve the performance of APDs. The minimization of this excess shot noise can be achieved through either material selection or through specific band diagram design.

1.1.1 Impact Ionization and k-Factor

Minimizing excess noise through material selection works through minimizing feedback and thus the inherent randomness of the impact ionization process. Within a semiconductor, electrons and holes are both capable of initiating impact ionization events. Thus, each carrier injected into the multiplication region of an APD experiences a probability of impact ionizing once, several times, or not at all. The random nature of impact ionization guarantees variation in the multiplication gain of multiple carriers injected into an APD. Understanding the variation in gain, and thus excess noise, of an APD requires understanding the concept of ionization coefficients.
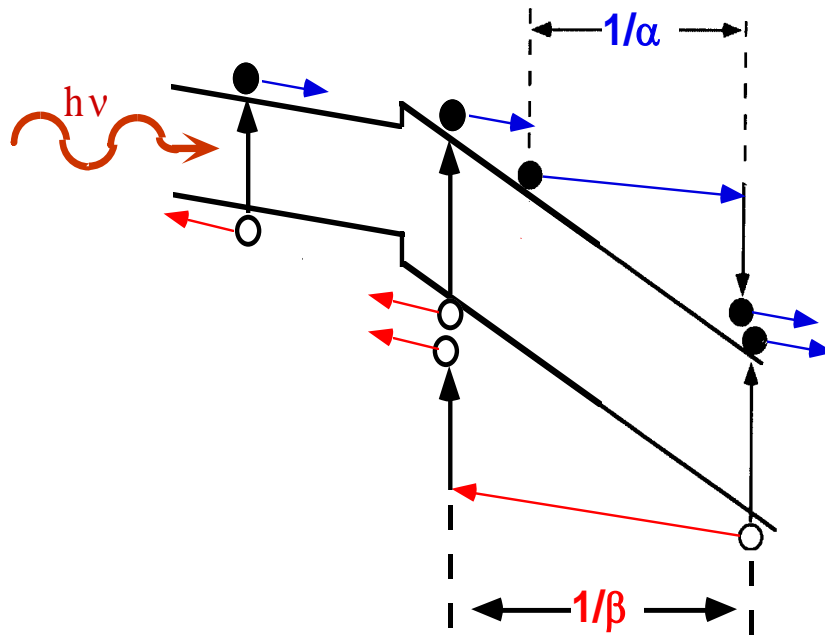
Figure 1-2: Conceptual band diagram of an APD illustrating electron and hole ionization coefficients.
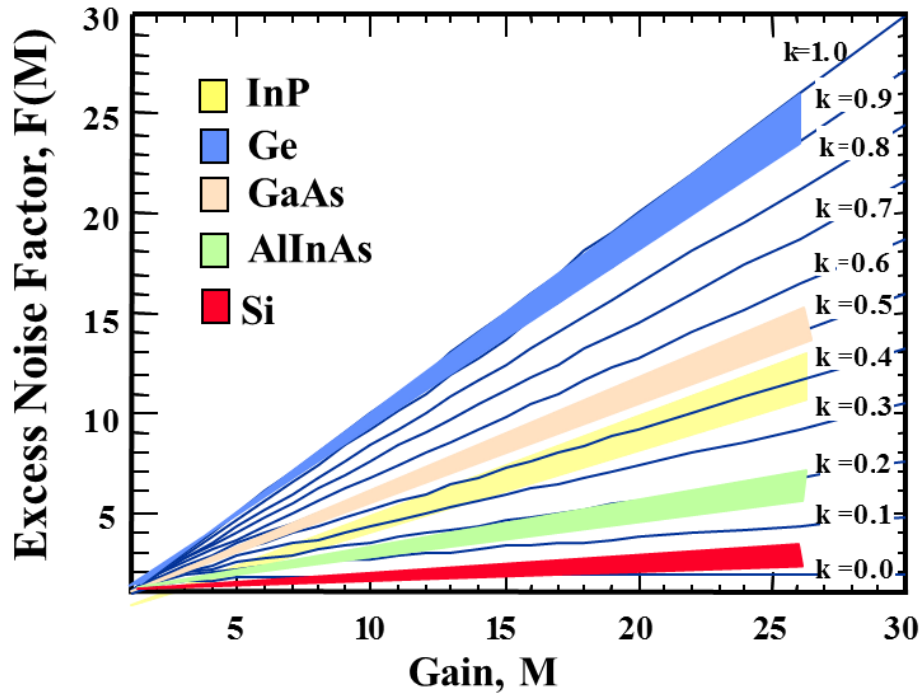
Figure 1-3: Excess noise versus gain for a range of k-values. Shaded areas denote corresponding k-values for different materials **[13]**.

The electron and hole ionization coefficients, α and β, are material parameters related to the probabilities of electrons and holes impact ionizing in a given material, which, in turn, are related to the band structure. The electron ionization coefficient, α, describes the inverse of the average distance an electron travels before impact ionizing; the hole ionization coefficient, β, describes the inverse of the average distance a hole travels before ionizing, as shown in Figure 1-2. The ratio of these two coefficients is the impact ionization ratio, or k-factor [13]. This figure of merit helps to describe how random, and thus, how noisy, the gain is for a given APD. The excess noise values and k-factor ranges are shown in Figure 1-3 for several materials, including silicon, germanium, and indium phosphide. The k-value of a material varies with electric field strength; as electric field increases in a material, the k-factor tends toward unity.
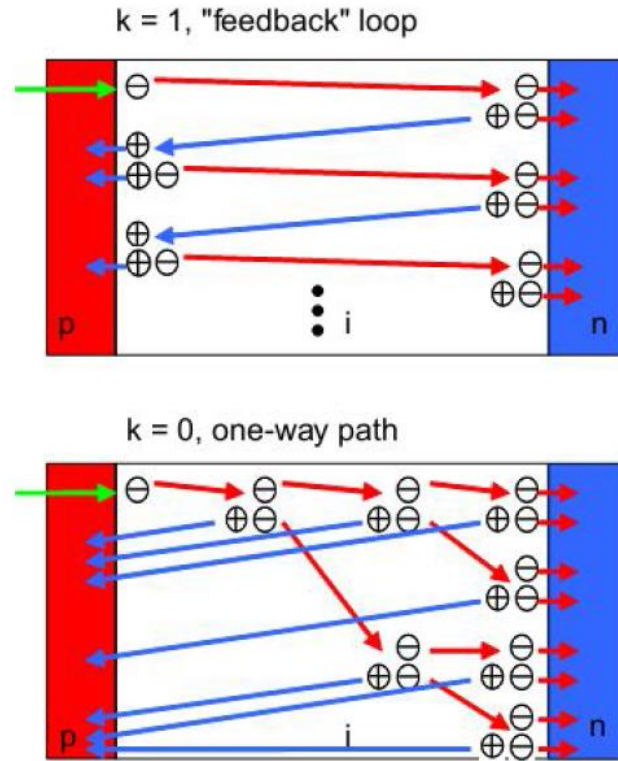
Figure 1-4: Conceptual illustration of impact ionization events in high k-value (top) and low k-value (bottom) materials **[14]**.

In materials with a high k-factor, impact ionization events are equally likely to be initiated by an electron as by a hole. The top illustration in Figure 1-4 represents a p-i-n photodiode made from a material where k = 1. As the electron travels through the depletion region, it gains kinetic energy. Eventually, it has sufficient kinetic energy as to potentially generate an electron-hole pair. The hole from this pair can create a second electron hole pair. The electron can generate a third electron hole pair, and so on. Owing to the feedback inherent in this system, this process is both lengthy and highly stochastic. An example of such a material is germanium, which is rarely used as a multiplication material in an APD due to its high k-value.

In materials with a low k-factor, on the other hand, the large asymmetry between the electron and hole ionization coefficients means that impact ionization events are initiated by only one type of carrier, either electrons or holes. Materials with a low k-factor have less feedback,

creating a faster, more deterministic gain. In the bottom illustration of Figure 1-4, which represents a p-i-n photodiode made from a low k-value material, it is clear that as the injected electron travels through the depletion region, it triggers a chain of electrons creating new electron hole pairs. However, the holes do not impact ionize. This makes for a much faster, more deterministic process. An example of such a material is silicon, which has a k-value less than 0.1. In silicon, electrons are much more likely to initiate impact ionization events than holes. As a result, silicon photodiodes are a popular subject of research.

In APDs with a thin multiplication layer, in order for the carriers to achieve the same gain as that of an APD with a thick multiplication layer, the electric field has to be higher. Therefore, one would expect the excess noise characteristics of APDs with thin multiplication layers to mimic materials with high k values. However, the opposite case is observed; thinner multiplication regions achieve lower effective k-values. This phenomena has been demonstrated for many materials, including InP [15] [16], GaAs [17] [18] [19], InAlAs [20], AlGaAs [16] [21], and SiC [22]. The non-local nature of impact ionization helps to explain the phenomenon [19]. "Dead space" is the minimum distance a carrier must travel in order to gain sufficient energy from the electric field to initiate impact ionization. When the ratio of dead space to multiplication region thickness is sufficiently high, a carrier is less likely to instigate a gain that is substantially larger than the average gain. In other words, the variance in the gain is minimized, and thus yields lower excess noise. Thus, devices have been designed with lower effective k-values through the use of thin multiplication regions. Impact ionization engineering takes the design of device band diagrams a step further.

1.1.2 Impact Ionization Engineering

"Impact ionization engineering" (I^2E) uses careful design of the photodiode band structure. Through impact ionization engineering, it is possible to keep gain deterministic by localizing the points where carriers impact ionize, minimizing excess noise. Conventionally, efforts to reduce excess noise have driven the study of new materials and fine-tuning the electric field profile. Excess noise, in these cases, is limited by material choice. On the other hand, impact ionization engineered devices use heterojunctions to localize impact ionization to distinct points in the structure. The I^2E technique has proved effective in many cases [23] [24] [25].

One example of an I^2E device was designed by Yuan et. al. [23]. This structure utilizes GaAs/$Al_xGa_{1-x}As$ heterojunctions to provide greater localization of impact ionization than can be achieved in spatially uniform structures. By placing thin multiplication layers with low thresholds for impact ionization next to regions with high ionization thresholds, impact ionization is enhanced at the junctions between the two materials and suppressed in the materials themselves. A schematic of this structure is shown in Figure 1-6. Impact ionization is enhanced at the twin, shaded multiplication layers and suppressed in the center region. Yuan et. al. achieved noise lower than either a GaAs or an $Al_xGa_{1-x}As$ homojunction structure, as is shown in Figure 1-5, which plots the noise of the two homojunction structure and three I^2E devices over the excess noise values of varying k-factors according to McIntyre's local field model [13]. Another example of an impact ionization engineering device is the staircase photodiode, which is discussed at length in chapter 2.
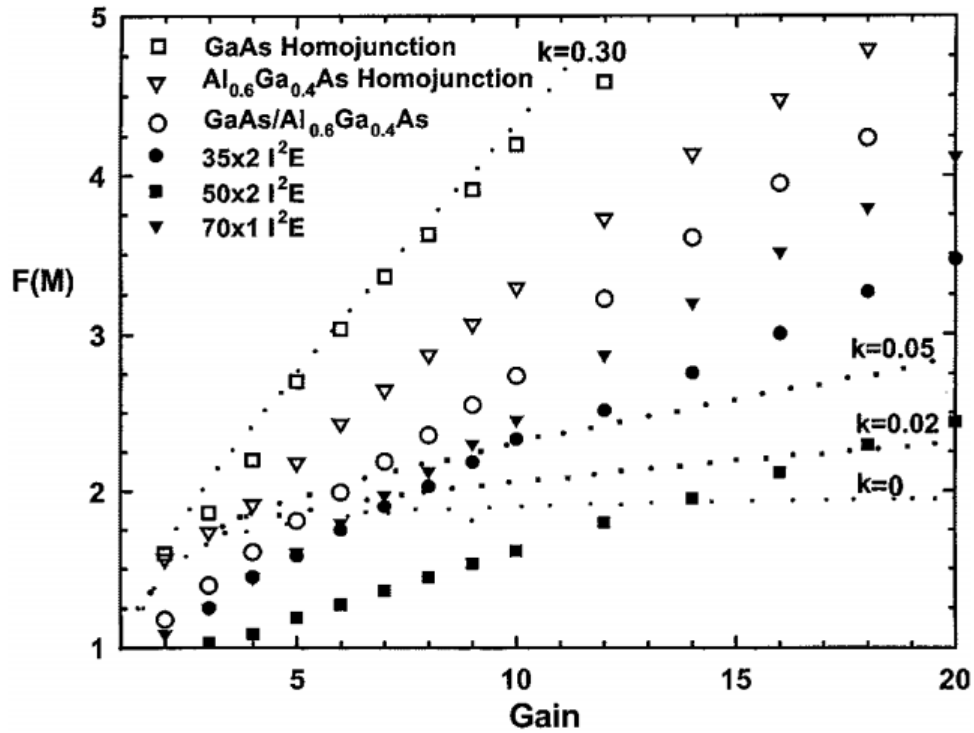
Figure 1-5: Measured excess noise factors for the I^2E devices and two homojunction APDs for comparison. Symbols show the measured excess noise factors; the dotted lines represent the excess noise calculated for several k-values.
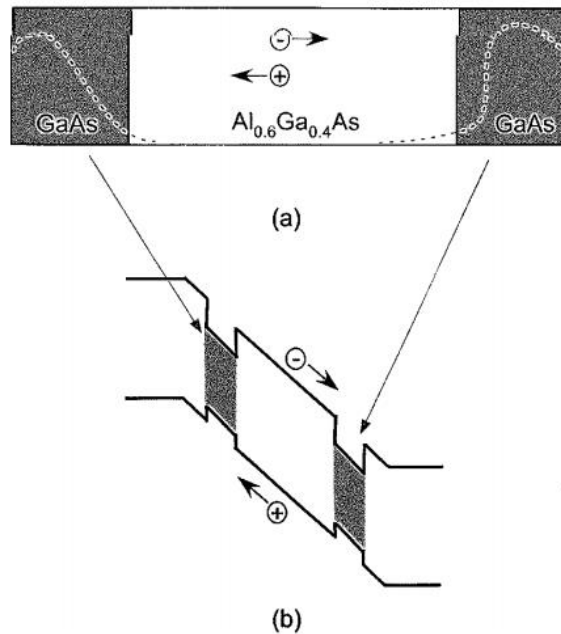
Figure 1-6: (a) Schematic and (b) band structure of the I2E device designed using the GaAs/Al$_x$Ga$_{1-x}$As material system.

1.2. APD Characteristics and Measurement Techniques

An avalanche photodiode is, in essence, a reversed biased diode in which the electric field is sufficient to initiate impact ionization, a process by which accelerated carriers generate additional electron-hole pairs through collisions that excite valence band electrons to the conduction band. These new carriers also travel through the electric field, gaining energy, and releasing more bound electrons, and so on.

$$SNR = \frac{\frac{1}{2}(q\eta P/h\nu)^2 M^2}{2q(I_{ps} + I_{BG} + I_{DM})F(M)M^2\Delta f + 4kTB/R_{eq}} \tag{1.1}$$

The quality of an APD is determined by a number of factors, which can be summed up generally in the signal to noise ratio, described in equation (1.1) [26]. In this equation, η represents external quantum efficiency, P is the input optical power, I_{ps} and I_{BG} represent the currents generated by the optical and background illumination, respectively. I_{DM} represents the component of the dark current that is multiplied through impact ionization (also known as the primary dark current), M is the avalanche gain, F(M) is the excess noise factor, B is the bandwidth, T is the temperature, and R_{eq} is the equivalent resistance of the device.

A high-quality APD will have low noise, which involves lowering the excess noise factor and leakage, or dark, current. Meanwhile, high signal to noise ratio requires high quantum efficiency, and high gain. The focus, therefore, in designing a high-quality APD involves balancing all of these factors, while keeping the noise such that it is always dominated by the circuit and not the APD itself.

1.2.1. Dark Current

The term dark current describes the leakage current in an APD, or, in other words, the amount of current flowing through the device under zero illumination. Dark current is caused by three factors: diffusion, recombination-generation, and tunneling. Dark current due to diffusion can be reduced by operating the device in a cooled environment, which reduces the thermal energy available to carriers, or by making use of wider bandgap materials, where applicable. Generation-recombination can be avoided by improving material quality and using lower doping levels. Wide bandgap materials are also less susceptible to dark current caused by this mechanism. Additionally, the use of surface passivation helps to eliminate dangling bonds and thus reduces recombination-generation-based dark current. Tunneling, too, is affected by material quality and doping level. Tunneling becomes prominent at high electric field, and thus dark current can be mitigated with longer depletion regions and wide-bandgap materials where possible. Optimizing all these parameters is crucial for designing a device with minimal dark current. I measured the current-voltage (I-V) characteristics of the dark current with an HP4145 semiconductor parameter analyzer, under no illumination.

In addition to measuring the dark current of a single-sized device, size-dependence studies can be employed in order to determine whether bulk or surface effects dominate the dark current. These studies are performed by measuring a set of photodiodes of varying diameters and plotting dark current versus diameter at a given bias. Bulk mechanisms scale linearly with the area, or, in other words, they scale quadratically with device diameter. Surface effects scale linearly with the device diameter. Similarly, by plotting the dark current versus gain for a single photodiode and generating a best-fit line, one can determine coefficients for the multiplied dark current and surface leakage current, according to equation (1.2), where I_D is the total dark

current, I_{DB} is the multiplied dark current, and I_{DS} is the surface leakage current. Typically, bulk-dominated dark current indicates an issue with crystal quality, while surface-dominated dark current suggests a non-optimal fabrication process.

$$I_D = I_{DS} + I_{DB} \times M \tag{1.2}$$

1.2.3. Avalanche Gain

The avalanche gain of a simple p-i-n APD can be understood by examining a current-voltage (I-V) curve, which plots the photocurrent versus the reverse bias. Figure 1-1-7 shows that at low reverse bias, the photocurrent increases as the electric field increases across the depletion region. Once the region is fully depleted, the photocurrent is relatively independent of bias. In this region, referred to in the figure as the p-i-n bias range, one can define the primary photocurrent, and thus the unity-gain bias. At higher bias, the photocurrent moves into the avalanche breakdown region, where carriers begin to gain sufficient energy to impact ionize. The gain of the device at a particular bias is defined as the ratio of the photocurrent at this bias to the primary photocurrent, and can be calculated using equation (1.3), in which the subscript "0" represents the value of the current at the unity-gain point.

$$M = \frac{I_{photo}}{I_{photo0}} = \frac{I_{total} - I_{dark}}{I_{total0} - I_{dark0}} \tag{1.3}$$

In my research, I used an HP4145 semiconductor parameter analyzer to measure I-V characteristics for both photocurrent and dark current, and then used this data to calculate gain.
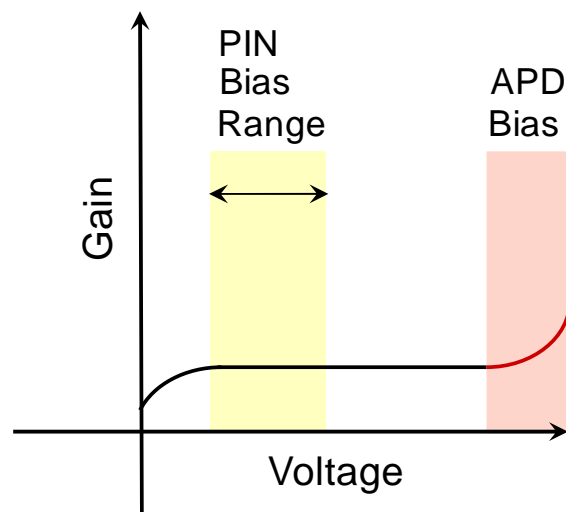
Figure 1-1-7: Conceptual gain versus voltage curve for a photodiode.

In their applications, APDs are typically operated under a bias feedback loop and/or with a temperature controller. Thus, it reduces receiver complexity and cost if the APD gain is relatively stable for temperature changes. This temperature dependence of the gain can be characterized by the gain temperature coefficient, $\Delta V/\Delta T$ [27]. Similarly, receiver complexity can be reduced for APDs that have temporally stable gain, in other words, for APDs whose gain is constant over extended periods of time. We study temperature dependence in our low temperature chamber, which is cooled with liquid nitrogen, and couple light onto the mesa active area for illumination. Both temperature and temporal stability are conducted on vibration isolation tables to minimize coupling fluctuations.

1.2.4. Excess Noise

As I alluded to in the section describing impact ionization, the randomness of the impact ionization gain mechanism generates noise, called excess noise. The excess noise factor, F(M), in a sense describes the variance in gain (σ_M), as shown by equation 1.4, caused by the randomness of carrier transport on the microscopic level. Using the local field model for a uniform electric field, the excess noise factor can also be expressed in terms of the k-factor, as shown in equation (1.5) [13].

$$F(M) = \frac{\langle M^2 \rangle}{\langle M \rangle^2} = 1 + \frac{\sigma_M^2}{\langle M \rangle^2} \tag{1.4}$$

$$F(M) = kM + (1 - k)\left(1 - \frac{2}{M}\right) \tag{1.5}$$
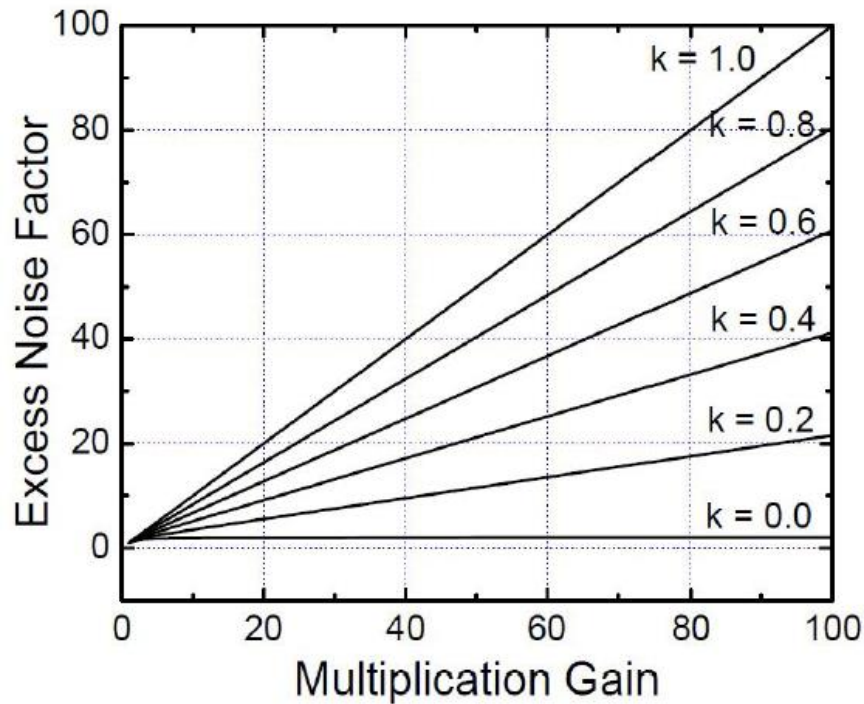
Figure 1-8: Excess noise factor as a function of multiplication gain for varying k-values.

It becomes clear from these equations that the excess noise increases with gain, for nonzero k-values. With no gain, however, the excess noise drops to 1; in other words, there is no excess noise. It is worth noting that excess noise increases with gain more quickly for devices with higher k-values. This point is well illustrated in Figure 1-3, in which excess noise factor is plotted versus gain for a range of k-values.

In order to measure the noise of our devices, we employ the local field model for noise power spectral density, expressed in equation (1.6), where R is the total impedance of the device under test and the measurement system. The device is first biased to its unity gain point, where $M = 1$. At this point, we can establish the values for gain, excess noise, and photocurrent, leaving only the total impedance to solve for, where S=2qIR.

$$S = 2qIM^2F(M)R \hfill (1.6)$$

By taking the ratio of the noise power of the device to the unity noise power, one can solve for the excess noise factor using equation 1.7. Here, N_p represents the photo noise power at a given frequency, which is determined from the total noise power and the dark noise power. N_{p0} represents the photo noise power at unity gain, for the same frequency. The excess noise can be plotted for a range of gain values, and these points can be fit to an effective k-value.

$$F(M) = \frac{N_p}{N_{p0}M^2} \hfill (1.7)$$

The noise figure meter is used to determine both the dark noise power (N_d) and total noise power (N_t). Using these two values, one can calculate the photo noise power, N_p. A Keithley 2400 is used to bias the device and determine the dark current and total current at each point, and thus the gain of the device according to equation (1.3). By combining the gain, photo

noise power, and photo noise power at unity gain, equation (1.7) can be used to determine the

excess noise factor of the device.
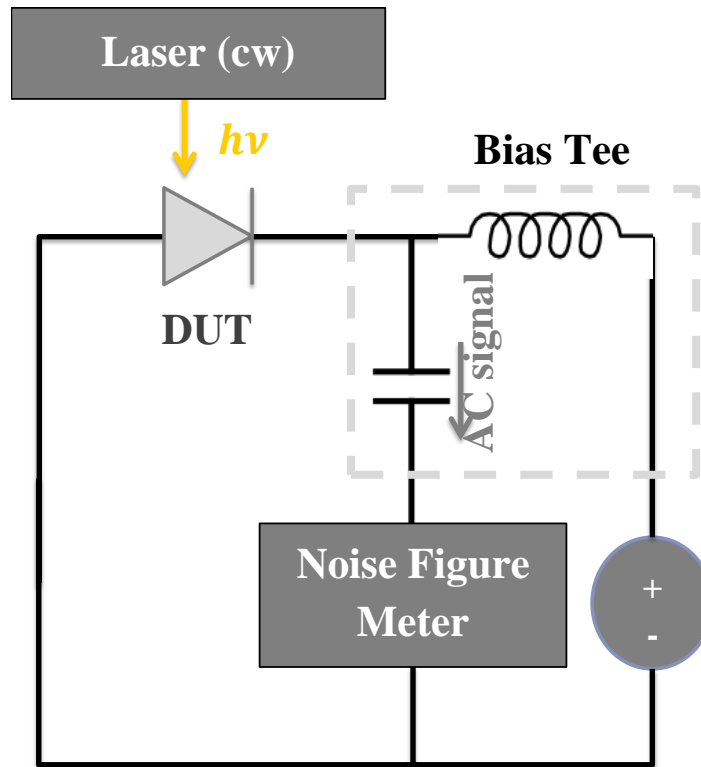
Figure 1-9: Diagram of experimental setup for excess noise measurement.

In my studies, I measure excess noise using an HP 8970 noise figure meter with a bias tee

to separate the DC bias and RF signal. A schematic of the measurement setup is shown in Figure

1-9. The device under test is illuminated with a visible-wavelength He-Ne laser with the light

spot fixed at the center of the mesa. Illumination on the side of the mesa would result in mixed

injection, and thus, inaccurate excess noise measurements.

1.2.5. Quantum Efficiency and Responsivity

The external quantum efficiency is the ratio of collected carriers to incident photons for a particular wavelength, in effect describing the probability that a single incident photon will generate an electron-hole pair that will contribute to the device current. Several factors determine the quantum efficiency of a photodetector. A photon may fail to be absorbed due to reflection at the surface of the detector, which motivates the implementation of anti-reflection coatings, which can help increase quantum efficiency. Surface recombination of carriers is another effect that can decrease quantum efficiency, and is typically mitigated through a surface passivation coating. Thirdly, the quantum efficiency is wavelength-dependent, and thus is typically measured over a range of wavelengths.

The wavelength dependence of the quantum efficiency originates primarily in the wavelength-dependence of the absorption coefficient. For sufficiently long wavelength values, the photon energy is too small to be absorbed; the photon energy is smaller than the bandgap energy, and thus the material is transparent. On the other end of the spectrum, for a sufficiently short wavelength, the photons are absorbed too near the surface, and often recombine before they can be collected. These two boundaries define a range of wavelengths over which the photodiode is operational. Thus, this aspect of the quantum efficiency is dependent on the material of the absorption region of the device and its respective bandgap.

Equation (1.7) shows the theoretical quantum efficiency for a photodiode, where $\mathcal{R}$ represents the optical power reflectance at the surface, ζ represents the fraction of electron-hole pairs that contribute to the detector current (without recombining), α represents the absorption coefficient, and d is the thickness of the absorbing region.

$$\eta = (1 - \mathcal{R})\zeta[1 - \exp(-\alpha d)] \tag{1.7}$$

$$i_p = \eta q \Phi = \frac{\eta q P}{h\nu} = RP \tag{1.8}$$

$$R = \frac{\eta q}{h\nu} = \frac{\eta \lambda}{1.24} \tag{1.9}$$

The responsivity of a photodiode device is closely related to its quantum efficiency. This parameter relates the electric current that flows through the device to the optical power of the light incident on it. Responsivity is linearly proportional to the quantum efficiency and the free-space wavelength of the incident light. Responsivity, which has the units of A/W, can be calculated using equation 1.8 or 1.9, where Φ represents the electron flux in the photodetector circuit, q represents the elementary charge, and P represents the incident optical power.
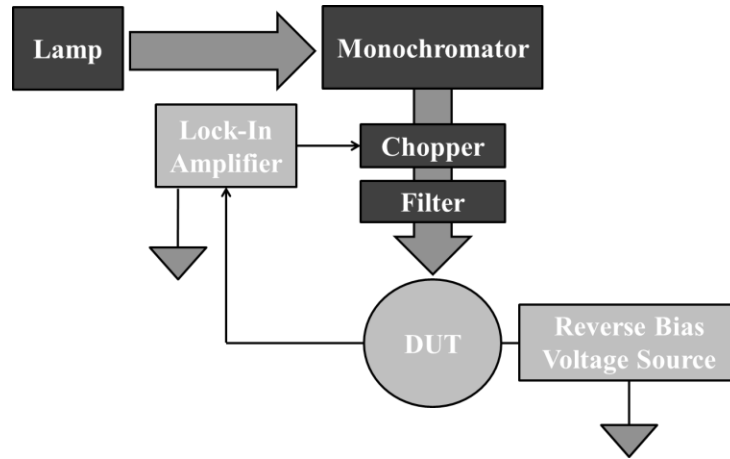
Figure 1-10: Block diagram of experimental setup for quantum efficiency and responsivity measurements.

In this work, I used a tungsten-halogen light source to generate a continuous light spectrum, in conjunction with a monochromator, which converted the broad-spectrum light into a narrow wavelength band. A lock-in amplifier and optical chopper were used to isolate the signal from the background noise. A block diagram of this setup is shown in Figure 1-10. In order to calibrate the quantum efficiency measurement setup, I used a packaged silicon photodetector with a known spectral response to normalize my data. Longer wavelengths were calibrated using a packaged InGaAs photodetector, again with a known spectral response.

1.2.6 Bandwidth

The 3 dB bandwidth of a device describes the frequency where the output RF power decreases by 3 dB compared to its low-frequency value. The bandwidth of a device can be limited by two factors: the RC time constant and the carrier transit time. The transit-time-limited bandwidth of a p-i-n device can be expressed as equation (1.10), where d represents the depletion width of the device and v_s represents the average of the electron and hole saturation velocities. The RC-limited bandwidth of a p-i-n device is expressed by equation (1.11), where ε is the dielectric constant of the i-region, C is the junction capacitance, R_S is the series resistance of the device (including the resistivity of the contact metal and the sheet resistance), R_L is the load resistance (typically 50 Ω), and A is the device area. The RC and transit-time bandwidth components can be combined to estimate the bandwidth, using equation (1.12)

$$f_{transit} = 0.5 \times \frac{v_s}{d} \tag{1.10}$$

$$f_{RC} = \frac{1}{2\pi RC} = \frac{d}{2\pi(R_s + R_L)\varepsilon A} \tag{1.11}$$

$$f_{3dB} \approx \sqrt{\frac{1}{\frac{1}{f_{RC}^2} + \frac{1}{f_{transit}^2}}} \tag{1.12}$$

Recall that in the previous section, the external quantum efficiency of a photodiode was proportional to the width of the depletion region. It follows that there is an inherent tradeoff between quantum efficiency and transit-time bandwidth. In a homojunction photodiode, where absorption and multiplication both occur in the i-region, a thicker i-region is required for high quantum efficiency, which in turn increases the carrier transit time, lowering bandwidth. The RC bandwidth of a device also increases with thicker i-regions, giving a trade-off also between RC bandwidth and transit-time bandwidth.

To overcome the RC limit of the bandwidth, it can become critical to fabricate structures with small mesa diameters, for lower capacitance values, with metals designed to lower the resistance of the device. A metal-semiconductor junction results in an ohmic contact only if the Schottky barrier height is less than or equal to zero. Thus, in designing contacts for APDs, it becomes necessary to employ a metal with a suitable work function with attention to Fermi pinning. Annealing can be used to further reduce resistivity. To measure contact resistance, I used transmission line measurements (TLM), in which I measured the resistance between a set of contacts separated by known distances. By plotting the measured resistances versus the separation distances, and adding a linear fit to the data, the R-intercept gives twice the contact resistance and the slope gives the sheet resistance of the semiconductor over the width of the contact. A sample of this technique is shown in Figure 1-11.
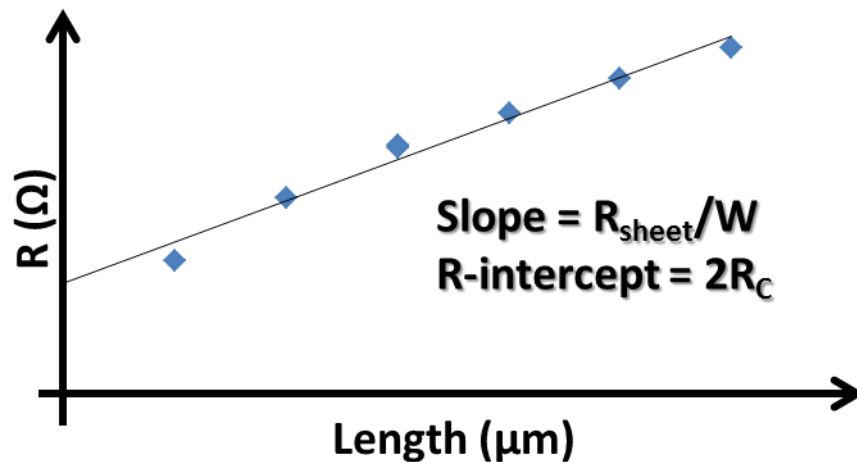
Figure 1-11: Sample measurement of sheet and contact resistance of a device using TLM technique.

There is a trade-off, also, between a photodiode's bandwidth and multiplication gain, which is described by the term gain-bandwidth product (GBP). As discussed in section 1.1.1, APDs that use materials with k-values larger than zero for multiplication regions experience impact ionizations from both electrons and holes. As a result, the impact ionization gain process

in this APD forms a feedback loop, which increases the amount of time necessary for the gain to "build-up," called the avalanche build-up time. Because of this build-up time, the speed of devices with high k-values, and thus, significant feedback, is much slower than devices with minimal feedback. This gives an inherent limitation to the amount of gain that can be achieved for a given bandwidth. Figure 1-12 shows the bandwidth as a function of multiplication gain for varying k-values, according to McIntyre's local field model [13]. For devices using multiplication materials with k-values close to zero, the bandwidth is relatively independent of gain, giving a high gain-bandwidth product. Materials with high k-values, however, are highly limited in terms of the gain achievable at a given bandwidth, resulting in a low gain-bandwidth product. This limitation further motivates the study of devices with low k-value multiplication materials.
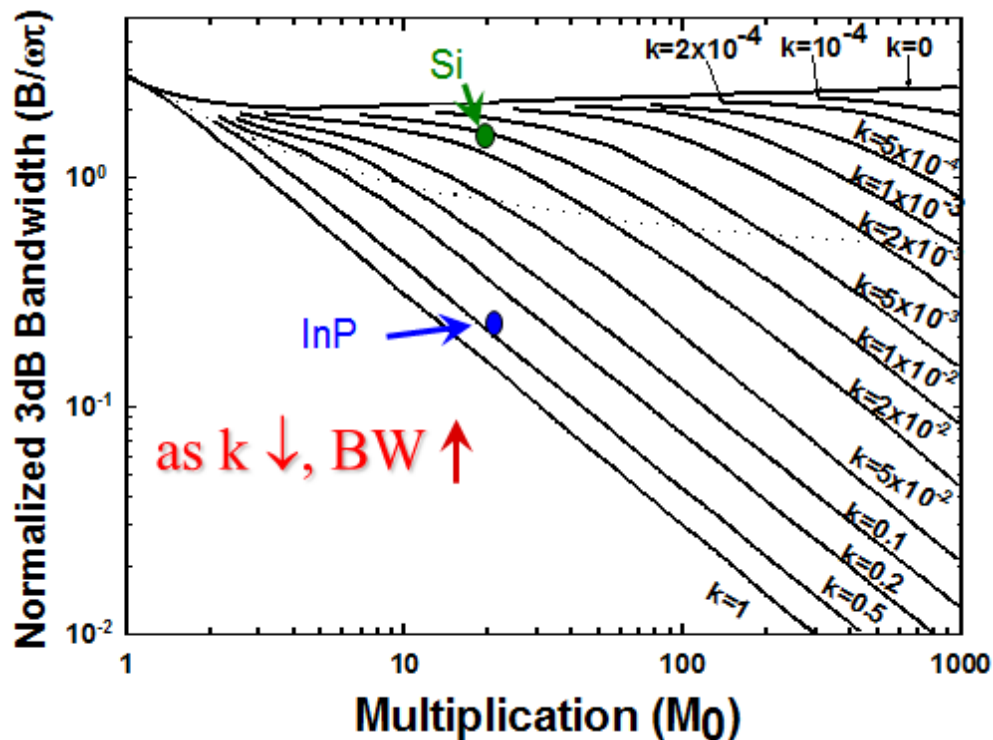
Figure 1-12: Bandwidth as a function of multiplication gain for varying k-values. **[8]**

1.3. Material Growth and Fabrication

1.3.1. Material Growth

Prior to these studies, lattice-matched growths of the AlInAsSb material system have achieved only as much as a 30% aluminum fraction [28] [29], though there has been mixed success growing material with up to a 60% aluminum fraction without lattice-matching due to a miscibility gap [30] [31]. While Vaughn et. al. were able to use a digital alloy technique to push Al fractions up as high as 40%, photoluminescence was only observed in Al concentrations as high as 30% [32]. Our collaborators at the University of Texas at Austin, however, were able to grow AlInAsSb quaternary material, lattice-matched to GaSb for Al fractions ranging from 0% to 80%.
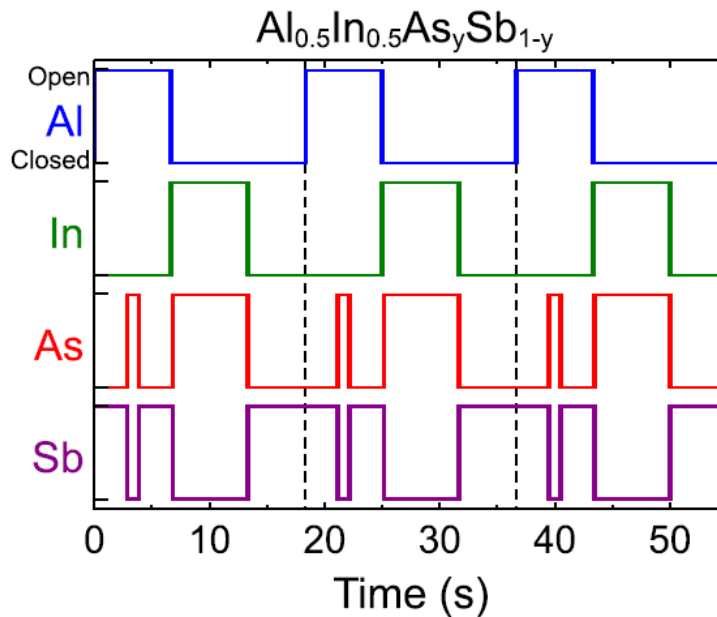
Figure 1-1-13: Shutter sequence for three periods of an AlInAsSb digital alloy **[31]**.

The samples in these studies were grown by Scott Maddox, a recent PhD graduate of Seth Bank's group at the University of Texas at Austin. The samples were grown on n-type Te-doped GaSb (001) substrates by solid-source molecular beam epitaxy at a growth temperature of 480°

C, as determined by blackbody thermometry (k-Space BandiT) [31]. In order to bypass the wide miscibility gap in the AlInAsSb material system, these layers were grown as a digital alloy of the binary alloys AlAs, AlSb, InAs, and InSb using a repeating shutter sequence: AlSb, AlAs, AlSb, InSb, InAs, and Sb, as is shown in Figure 1-1-13. Beryllium and tellurium were used as p- and n-type dopants, respectively. Further growth details and optical properties of the resulting material can be found in [31].

1.3.2. Standard Fabrication Process

The following process was the standard process used for the fabrication of AlInAsSb APDs. Modifications to and deviations from this process are described in detail in respective chapters. For wet-etched devices, circular mesas were defined using standard photolithography processes and wet-etched using an $HCl:H_2O_2:H_2O$ solution (1:1:10). Alternatively, to dry etch devices, a silicon dioxide hard mask was deposited using plasma-enhanced chemical vapor deposition (PECVD) and circular mesas were patterned with an AZ5214 photoresist. Samples were then etched in a reactive ion etching (RIE) chamber using inductive coupled plasma (ICP). Silicon dioxide hard mask thickness on the device was monitored with dummy silicon dioxide on silicon wafers, grown in the same PECVD chamber; measurement of SiO_2 thickness was performed using spectroscopic interferometry. Following the dry etch, excess SiO_2 was removed using buffered oxide etch (BOE).

Etching was terminated with a surface-smoothing treatment of bromine methanol. In order to improve passivation and thus reduce the surface leakage current, an SU-8 coating was spun on immediately after the surface treatment. Titanium/gold contacts were deposited by e-beam evaporation onto the mesa and the substrate. For some devices, the GaSb top contact layer was removed except under the p-type contacts, in order to eliminate its parasitic optical absorption. In these cases, AZ 300 was used to selectively etch the GaSb, which etches in most developers, prior to SU-8 coating [33].

1.4 Monte Carlo Simulation of APDs

Simulations of APD multiplication through Monte Carlo models have been reported for many materials and structures [34] [35] [36] [37]. Even simple Monte Carlo simulations can provide insight to the electric field profile, the absorption profile, and the band diagram of a device. The model I use was developed over the course of several generations of students, primarily Feng Ma and Wenlu Sun. In addition to these simple output parameters, the models also provide key information on impact ionization locations, individual carrier gains, excess noise factor, and the carrier velocities and band occupancies. This model is written in C++ and is run on the UVA HPC server. I have begun a draft of documentation for the code written by Feng Ma, and it is included in appendix A. The full code for both Wenlu Sun's and Feng Ma's models are available in their respective dissertations [14] [38].

The Monte Carlo models used in my work model the conduction and valence band as simple, spherical, non-parabolic bands, and include gamma, X, and L valleys, as well as heavy hole, light hole, and split-off valence bands. The models take into account several types of carrier scattering, including intervalley and intravalley phonon scattering, alloy scattering, and impurity scattering, the formulas of which were derived using Fermi's golden rule. In addition to these carrier scatterings, the model also accounts for impact ionization scattering, the phenomenon which includes gain in an APD, using the Keldysh formula [39]. Each carrier injected into the device, and each secondary carrier generated by impact ionization, is tracked until it recombines or is collected at the contact.

Both versions of the Monte Carlo code begin by reading in input parameters. The input files for both models consist of a set of device parameters and several sets of structural parameters. The device parameters define conditions that apply to the overall structure, including temperature, bias, and photon energy. The structural parameters must be defined for each layer in

the device, and give details about the material's band structure, layer thickness, doping level, etc.

Though the two use slightly different device parameters, both models use the same format for

structural parameters, which are detailed with sample inputs in Table 1.1. Device parameters

included in both models are given in

Table 1.2, and parameters exclusive to Sun's model are shown in Table 1.3.

Table 1.1: Structural parameters for Feng Ma and Wenlu Sun Monte Carlo models.

Parameter	Sample
Material name	InAs
Layer thickness (m)	10.0e-9
Doping concentration (m^{-3})	6.0e24
Absorption coefficient (m^{-1})	2e7
Threshold energy – electron (eV)	0.42
Hard threshold energy – electron (eV)	150
Threshold energy – hole (eV)	0.42
Hard threshold energy – hole (eV)	155
Parameter r in Keldysh's formula of an electron	1.00
Parameter r in Keldysh's formula of a hole	1.00
Parameter C_{ii} in Keldysh's formula of an electron	3.5e12
Parameter C_{ii} in Keldysh's formula of a hole	8e8
Bandgap of Γ valley ($E_C(\Gamma)$-E_V(HH)) (eV)	0.417
Bandgap of L valley (E_C(L)-E_V(HH)) (eV)	1.133
Bandgap of X valley (E_C(X)-E_V(HH)) (eV)	1.433
Energy position of heavy hole (eV)	0
Separation of heavy hole and light hole, E_V(HH) – E_V(LH) (eV)	0.2
Separation of heavy hole and split-off, E_V(HH) – E_V(SO) (eV)	0.39
Effective mass of gamma valley, relative to m_0, the free electron rest mass	0.026
Effective mass of L valley, relative to m_0	0.072
Effective mass of X valley, relative to m_0	0.224
Effective mass of heavy hole band, relative to m_0	0.333
Effective mass of light hole band, relative to m_0	0.027
Effective mass of split-off band, relative to m_0	0.14
Scaling factor of hole scattering rate	1.0
Static dielectric constant	15.15
High frequency dielectric constant	12.3
Bandgap of material (eV)	0.417

Composition used for calculation of alloy scattering rate	0
Scaling factor for alloy scattering rate	1.0e15
Material density	5680
Velocity of acoustic waves	2945
Acoustic phonon energy	0.011
Optical phonon energy	0.024
Intervalley phonon energy	0.013

Table 1.2: Device parameters for Feng Ma and Wenlu Sun Monte Carlo models

Parameter	Sample
Input file name	input.prm
Temperature (K)	300
Energy of injected photons (eV)	0.43
Scaling factor for impurity scattering	1
Change of energy-gap per temperature (eV)	0.05
Total number of injected carriers	1000
Duration time of simulation	1e-8
Time resolution (minimum value of time step)	1e-17
Applied reverse bias(V)	10.01
Increase of bias per step of simulation (V)	1.00
Built-in voltage (V)	0.5
Upper limit of gain value	100
Total number of bias steps for simulation	1

Table 1.3: Device parameters exclusive to Wenlu Sun Monte Carlo model

Parameter	Sample
Time interval (s)	2.0e-11
Mode	2
Quasi-charge	100
Frequency	1e9
DC current	1.749e-3

Following the input read-in, the programs differ slightly. While the older version of the Monte Carlo code immediately builds a mesh structure and calculates the electric field profile of the APD a single time, the code developed by Wenlu Sun iteratively recalculates the electric

field in the device. Flowcharts for each of these models are shown in Figure 1-14. By designing a program to calculate the electric field for each time interval, Sun developed a method of accounting for the space-charge effect, which changes the electric field within a high-power photodiode over time. To simulate large injected currents, a factor called "quasi-charge" was integrated, giving each carrier a charge several orders of magnitude higher than the elementary charge as an estimation technique.

Following calculation of the electric field within the device, carrier drift and scattering processes are iteratively calculated for each electron and hole in the device, according to physical models and input parameters. Results returned by the programs include an output current, individual and overall multiplication gains, spatial distribution of ionization events, and an excess noise factor calculated from the variance in gain distribution.

(a)

| Read-in parameters for each layer (material type, doping, thickness, band structure, etc.) and device parameters (temperature, bias, built-in voltage, etc.) |

↓

| Build up the mesh structure and calculate the electric field distribution inside the device structure. |

↓

| Simulate the carrier drift and scattering process for each carrier (both electrons and holes) until carrier recombines or is collected at the contact. |

↓

| Collect, calculate, and output all results, including gain, current, and noise. |

(b)

| Read-in structural and device parameters and build the grid structure of the device. |

↓

| Calculate the electric field profile of the device. |

↓

| Simulate carrier transport for all carriers, both electrons and holes. |

↓

| Calculate charge density; recalculate electric field profile. |

↓

| Increment by time interval. |

While time < maximum time (loop back)

↓

| Collect, calculate, and output all results, including gain, current, and noise. |

Figure 1-14: Flowchart of Monte Carlo simulation developed by (a) Feng Ma and (b) Wenlu Sun.

1.5. Thesis Organization

The focus of my thesis is on developing low-noise photodiodes from the AlInAsSb materials system. Chapter 1 explains the motivation for this work, as well as the figures of merit for photodiodes and the techniques for their measurement. In chapter 2, I discuss the simulation, fabrication, and measurement of a single-step staircase AlInAsSb photodiode, a concept developed by Federico Capasso et al. [40] [41] and realized in the AlInAsSb material system. Chapter 3 presents a study of the $Al_{0.7}In_{0.3}As_{0.3}Sb_{0.7}$ material used originally as a control for the staircase APD. The $Al_{0.7}In_{0.3}As_{0.3}Sb_{0.7}$ APD is of particular merit because it exhibits low-noise characteristics comparable to that of silicon, with a direct bandgap structure that provides a significantly higher absorption coefficient. Chapter 4 presents a systematic study of homojunction photodiodes fabricated from the AlInAsSb materials system for varying Al fractions. The materials vary in bandgap with Al concentration, allowing detection in wavelengths ranging from 0.4 um to beyond 1.6 um. Chapter 5 describes the development of a separate absorption, charge, and multiplication avalanche photodiode (SACM APD) from the AlInAsSb materials system, designed according to the study from chapter 4. Chapter 6 presents an investigation of the properties of a tunneling staircase photodiode, which was originally designed as a two-step staircase structure, but shows tunneling effects that enhance gain at low bias. In chapter 7, I present my studies of two different digitally-grown material systems juxtaposed with their random alloy counterparts, with particular attention to differences in the excess noise factor and responsivity. Finally, the dissertation concludes with proposed future research plans, summarized in chapter 8.

Chapter 2 Single-Step Staircase $Al_xIn_{1-x}As_ySb_{1-y}$ Photodiode

2.1. Introduction

In 1983, Capasso et. al. proposed the staircase APD [41], a novel structure designed to reduce the excess noise [42]. In a conventional APD, impact ionization occurs across the entire multiplication region. However, in the staircase APD, impact ionization is localized to sharp bandgap discontinuities. In small-bandgap III-V materials, the energy threshold for impact ionization is approximated as 1.5x the bandgap. With sufficient band offset, at these discontinuities, carriers can gain sufficient energy to have a very high probability of impact ionizing. In this way, these discontinuities function similarly to the dynodes of a photomultiplier tube. Since impact ionization is localized to discrete locations, the gain of each injected carrier is identical, creating a deterministic gain, and thus low noise. Figure 2-1 shows the calculated excess noise factors of several detectors: a conventional APD fabricated from a low-noise material, two different staircase APDs, and two PMTs. Both the PMT and staircase APD have noise plotted for two different structures: one with a single multiplication stage and one with three multiplication stages. As is apparent in the figure, even a detector fabricated from an extremely low-noise material with a k-value of 0, yields nearly twice the excess noise of a photomultiplier tube or a staircase APD, both of which provide nearly excess-noise-free gain. While a single-stage multiplication only provides a gain of two, expanding to multi-stage staircase photodiodes offers the advantage of minimal noise at higher gains.

Figure 2-2(a) shows the conceptual band diagrams of a staircase APD at flatband and under reverse bias. Though Capasso's staircase APD failed due to insufficient band offsets in the material system (AlGaAs/GaAs) [43] [44], it sparked curiosity and interest in the field.
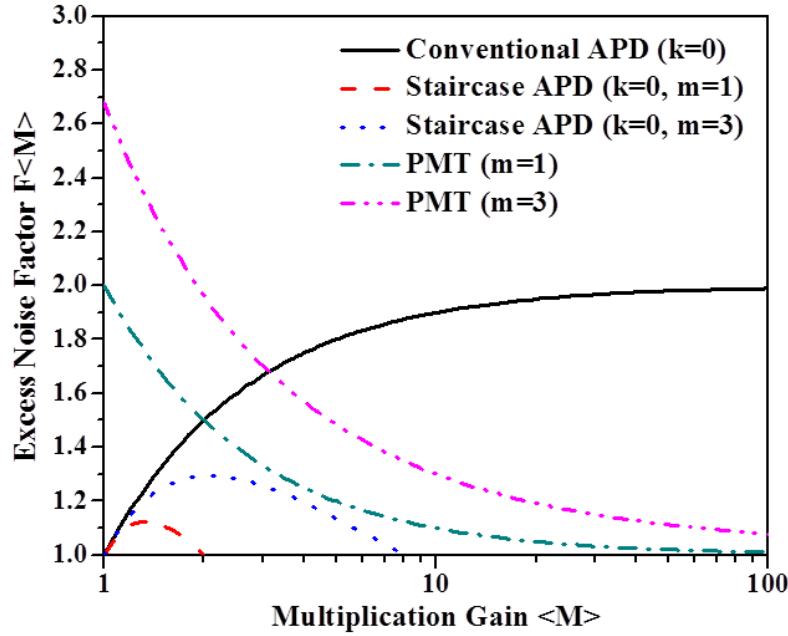
Figure 2-1: Ideal excess noise factors of a conventional APD (k=0), staircase APD, and PMT, where 'm' corresponds to the number of multiplication stages in the PMT or staircase APD.
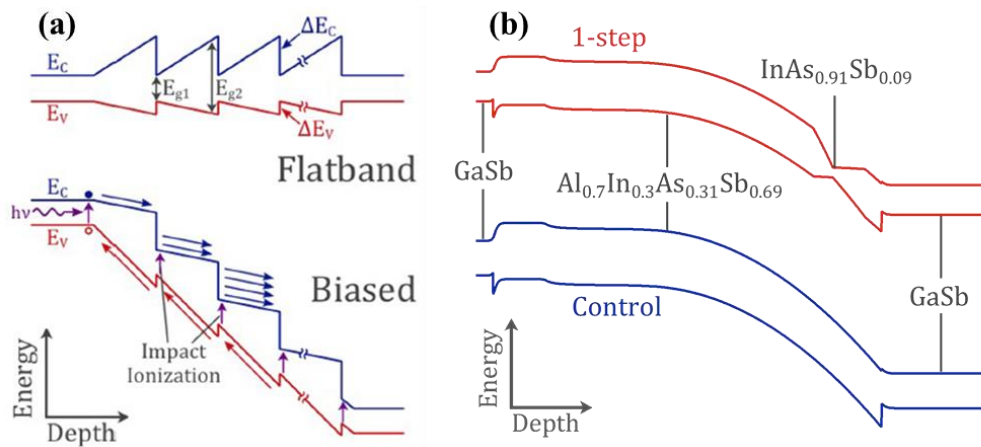
Figure 2-2: Conceptual band diagrams of (a) a staircase APD under no (top) and reverse (bottom) bias, and (b) the one-step and control structures at the staircase condition.

In our research, we developed a staircase APD based on the AlInAsSb material system. In this system, the wide bandgap injector is AlInAsSb, and the narrow bandgap multiplication region is InAsSb. Capasso's AlGaAs/GaAs system had a conduction band step height of 0.48 eV [40], only about a third of the energy of the narrow bandgap material, GaAs. In this staircase,

carriers don't gain enough energy at the conduction band discontinuity to impact ionize consistently [45]. The wide- and narrow-bandgap regions in the AlInAsSb system, however, have bandgaps of 1.16 eV and 0.25 eV, respectively, as measured by photoluminescence measurements conducted at the University of Texas [31]. This creates a significantly larger step, approximately 2.5× that of the narrow bandgap. Figure 2-2(b) shows conceptual band diagrams for a one-step staircase and control structures under bias. Since the bandgap discontinuity is over twice the energy of the narrow bandgap InAsSb layer, the new materials system provides a high probability of impact ionization at the discontinuity [45]. Noise is further mitigated by the low k-value of the constituent materials [46] [47].

2.2 Monte Carlo Simulations

Monte Carlo simulations of the AlInAsSb staircase APD were carried out using the model described in section 1.4. The input file used for these simulations is included in appendix B. Some parameters for this analysis, such as the band structure parameters, were derived from photoluminescence studies performed at the University of Texas [31]. Other parameters for the material have yet to be studied, and were estimated from weighted averages of the binary monolayer materials InAs, InSb, AlAs, and AlSb. Simulations of the device structure were performed for reverse biases sweeping from 1 V to tens of volts.
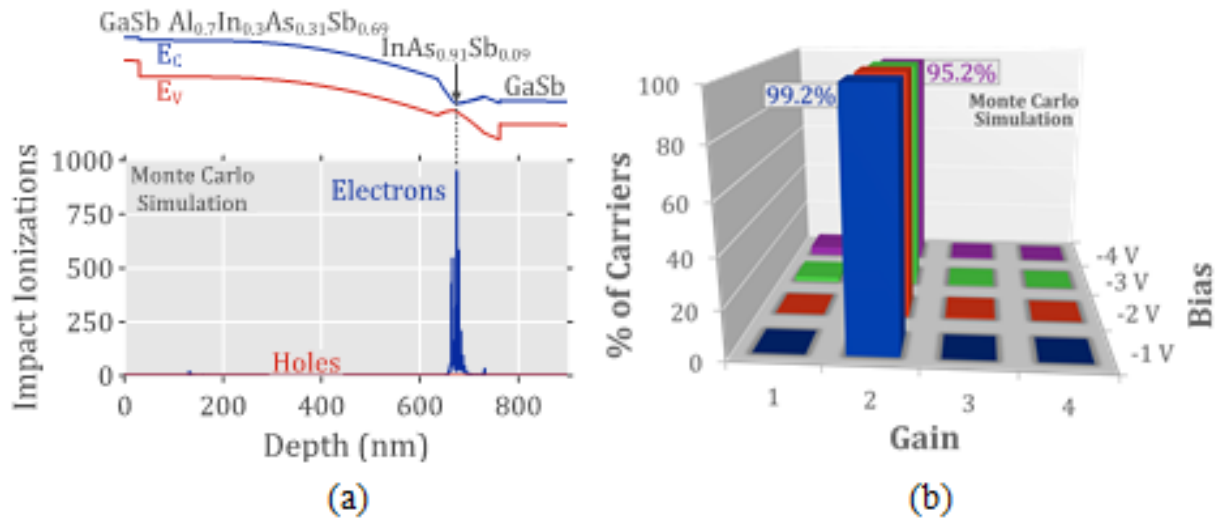
Figure 2-3: Monte Carlo simulations of a one-step AlInAsSb staircase APD at -2V bias (a) predict electron-only impact ionization, resulting in nearly ideal noise characteristics. Furthermore, the simulations predict an extremely sharp gain distribution independent of bias (b) with almost all electrons impact ionizing exactly once at a distinct location, resulting in a nearly excess-noise-free gain of about 2.

These simulations predicted that only electrons, localized primarily at the bandgap discontinuity, as summarized in Figure 2-3, would initiate impact ionization. Additionally, the simulations showed that once the bias was sufficient to flatten the graded layers of the staircase structure, the gain distribution was very sharp and independent of bias. The narrowness of this

distribution arose from nearly all of the electrons impact ionizing only once, giving a gain of two with nearly zero excess noise [41] [42]. Essentially, the Monte Carlo simulations predicted that the AlInAsSb staircase gain would be almost completely free of excess noise, making it possible to achieve much greater performance and bandwidth than traditional APDs.

2.3 Structure and Fabrication

To demonstrate the efficacy of the staircase APD gain mechanism in practice, Seth Bank's group at the University of Texas at Austin grew a one-step staircase APD and control structures on n+ GaSb, cross-sections of which are shown in Figure 2-4. The device on the left features a p++ GaSb layer, a p-layer of $Al_{0.7}In_{0.3}As_{0.3}Sb_{0.7}$, followed by an i-layer of the same material graded down in Al concentration to InAsSb, then back to $Al_{0.7}In_{0.3}As_{0.3}Sb_{0.7}$, on an GaSb n-layer, all on a n-doped GaSb substrate. The grading of the material from 70% to 0% Al creates the "step", i.e., the constriction point in the band diagram. The bottom GaSb layer serves as a substrate material that can be lattice-matched to AlInAsSb, and the top GaSb layer provides a low-work function material for ohmic contacts.
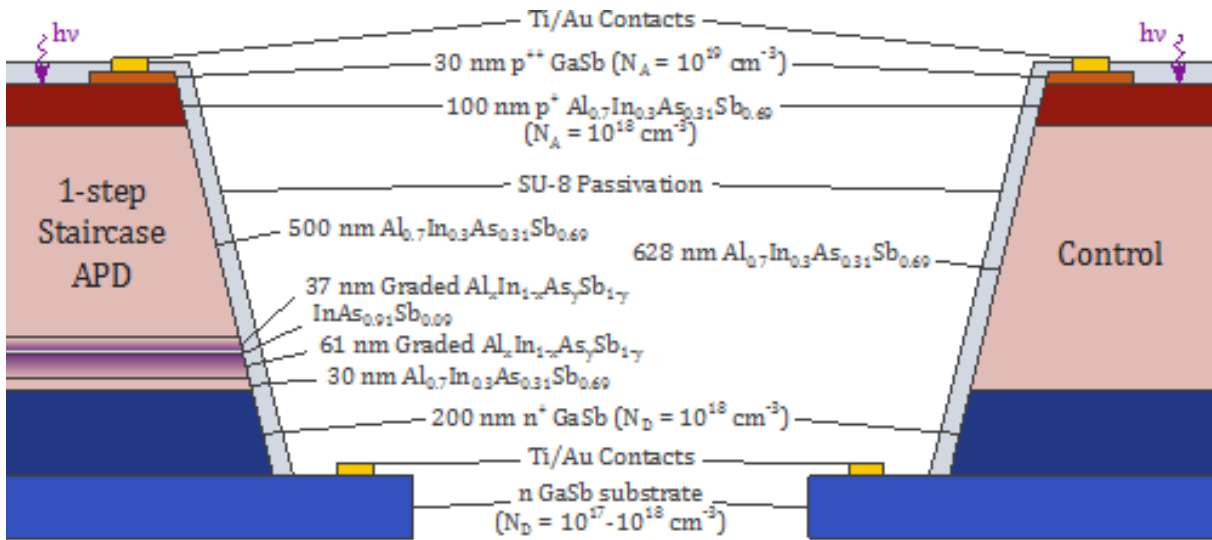
Figure 2-4: Schematic cross-sections of the one-step staircase APD and control AlInAsSb structures.

The control device on the right is substantially simpler, consisting only of a p++ GaSb layer, a p-layer of $Al_{0.7}In_{0.3}As_{0.3}Sb_{0.7}$, followed by an i-layer of the same material, and a GaSb n-

layer, all on a n-doped GaSb substrate, with no graded material. This structure was used as reference for the gain in the staircase structure.

Both structures include a top GaSb layer to reduce contact resistance, improve contact adhesion, and protect the underlying Al-containing layers from oxidation. Circular mesas were defined using standard photolithography and wet-etched using an $HCl:H_2O_2:H_2O$ (1:1:10) solution. Etching was terminated with a surface-smoothing treatment of bromine methanol. In order to improve passivation and thus reduce the surface leakage current, an SU-8 coating was spun on immediately after the surface treatment. Titanium and gold were deposited by e-beam evaporation onto the mesa and the substrate to form both the p- and n-type contacts.

2.4 Measurements

Initial studies focused on devices with AlInAsSb absorption regions that have a cutoff wavelength of 1.1 µm. To measure the gain of the staircase APD, a 543 nm He-Ne CW laser was chosen as the optical source, ensuring pure electron injection into the multiplication region. In order to determine the gain of this device, the photocurrent of the staircase APD was compared to that of the control. We repeated this process for 40 devices of each type, replicated over multiple growth and fabrication runs, in order to eliminate device-to-device variations.
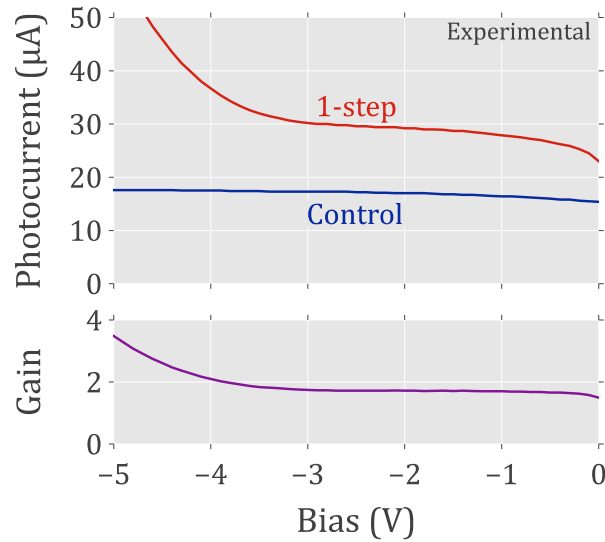
Figure 2-5: The one-step staircase APD exhibited enhanced photocurrent compared to the control at all reverse biases, and a gain of 1. 8± 0.2 from -1 V to -4 V. The measurement was performed on a 50 µm diameter mesa device at room temperature (300K) using a CW He-Ne laser operating at a wavelength of 543 nm.

Representative photocurrent curves for both the staircase and control structures are shown in Figure 2-5, under the same input optical power. The multiplication gain was found to be 1.8 ± 0.2, independent of reverse bias over the range of 1 V to 4 V, and independent of temperature from 80 K to 300K, consistent with both the staircase theory and the Monte Carlo simulations [42] [40] [48]. The photocurrent increases beyond a bias of -4 V, likely due to carriers gaining energy in the graded bandgap region beyond the InAsSb and GaSb layers and

ionizing as they would in a conventional APD. These results are also consistent with those of the Monte Carlo simulation.

The dark current of the single-step staircase APD was found to be bulk-dominated. Figure 2-6(a) shows a plot of the dark current versus device area for devices ranging in size from 50 µm to 500 µm in diameter. The dark current increases quadratically with device diameter, indicating a bulk-dominated generation-recombination dark current mechanism. Further studies were performed in a low-temperature chamber, cooled by liquid nitrogen. Figure 2-6(b) shows the dark current density versus bias for a 50 µm diameter device cooled from 300 K to 80 K in steps of 20 K using liquid nitrogen. For low reverse biases below -2 V, the dark current density varies substantially with change in temperature, indicating generation-recombination as the dominant dark current mechanism. At higher biases, the dark current density is relatively temperature-independent, indicating tunneling as the dominant dark current mechanism.
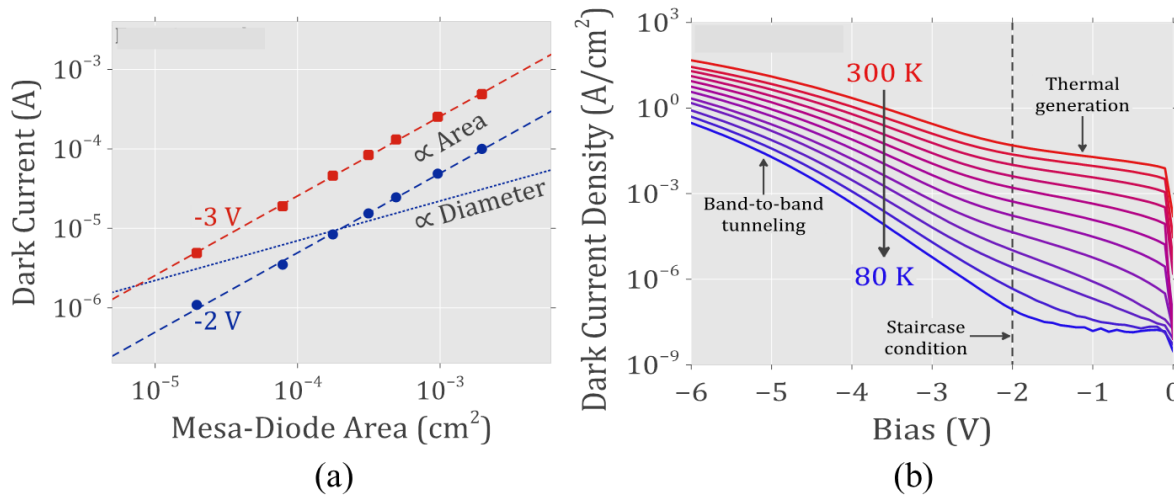
Figure 2-6: (a) The single step staircase APD dark current versus device area scales with area, indicating bulk-dominated dark current. (b) Additional temperature studies using liquid-nitrogen cooling reflect moderate dark current densities at room temperature to very low dark current densities for a cooled device. This temperature dependence is consistent with thermal generation at low reverse biases, and band-to-band tunneling at high reverse biases.

We also performed quantum efficiency measurements to verify that the increase in the photocurrent of the single-step staircase was not due to any enhanced absorption from the constriction point in the band diagram, where the bandgap is narrow. The results of this quantum efficiency measurement are shown in Figure 2-7. The single step staircase exhibits greater responsivity than the control for wavelengths above ~950 nm, due to absorption in the small-bandgap InAsSb region, as we expected. For a broad range of wavelengths shorter than 950 nm, however, the gain of 1.8 ± 0.2 remains approximately constant in the single-step device. These measurements confirm that the observed gain is a result of impact ionization rather than enhanced absorption.
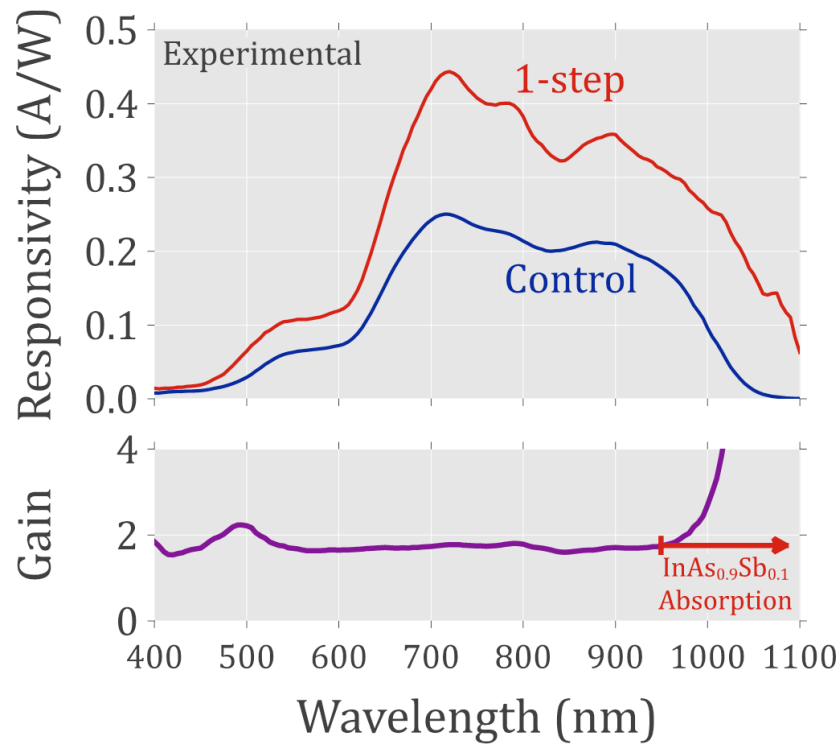
Figure 2-7: Responsivity measurements for the single-step staircase APD and control homojunction structure. The single-step staircase APD exhibited a gain of 1.8 ± 0.2 over a broad range of wavelengths below ~950 nm, verifying true gain from impact ionization and ruling out enhanced absorption in the InAsSb layer, which occurs above wavelengths of ~ 950 nm. Measurements were taken at 300 K.

We confirmed the low-noise characteristics of the multiplication gain by measuring the noise power as a function of bias. Since noise scales with gain-squared, we expected the noise of the staircase device to be 3.2× that of the control device. However, we found the noise was only 2 – 2.2× that of the control device, which, while advantageous, was unexpected, and thus will be the subject of future study. We note that this suppressed-noise phenomenon has been observed previously in impact-ionization engineered heterojunction APDs [49].

2.5 Chapter Summary

Through this study, we demonstrated a low-noise, single-step staircase APD based on the AlInAsSb material system, expanding on an initial design by Federico Capasso [41]. While Capasso's staircase APD failed due to insufficient band offsets in the AlGaAs/GaAs materials system, the large ratio of conduction-band discontinuity to the narrow bandgap InAsSb material provided sufficient energy to consistently generate impact ionizations at the stairstep point, resulting in highly deterministic, low noise operation. We hope to expand the staircase into multiple steps, giving gains of 4, 8, 16, etc., but we are currently limited by the material growth of a multi-step staircase. Since this is a new materials system, however, we became interested in characterizing AlInAsSb for use in other low-noise avalanche photodiodes.

Chapter 3 Low-noise $Al_{0.7}In_{0.3}As_{0.3}Sb_{0.7}$ Homojunction Photodiode

3.1 Introduction

In studying the $Al_xIn_{1-x}As_ySb_{1-y}$ material system for its use in a staircase APD, I became interested in the avalanche characteristics of the control devices. Recall that the control devices for the staircase APD were simply homojunction photodiodes grown from $Al_{0.7}In_{0.3}As_{0.3}Sb_{0.7}$. This material had never been grown before, spurring curiosity as to its usefulness in an APD. Additionally, our many staircase structures had yielded an array of control structures with i-regions of varying thicknesses. In this chapter, I report the study of a p-i-n structure APD fabricated from this material. These APDs offer the advantage of a high absorption coefficient resulting from their III-V compound direct bandgap composition. $Al_xIn_{1-x}As_ySb_{1-y}$ can be lattice-matched to GaSb for varying aluminum fractions, providing the flexibility to design complex structures to maximize performance and enable operation in different spectral regions [31]. In addition, these direct-bandgap APDs exhibit bulk excess noise comparable to Si without taking advantage of the dead-space effect in a thin multiplication region [50] [15] [51] [52].

3.2 Structure and Fabrication

A cross-sectional schematic of the $Al_{0.7}In_{0.3}As_{0.3}Sb_{0.7}$ device is shown in Figure 3-1. The structure includes a top GaSb layer to reduce contact resistance, improve contact adhesion, and protect the underlying Al-containing layers from oxidation. The device is a simple p-i-n structure. I fabricated devices according to the wet etch procedure outlined earlier in section 1.3.2.
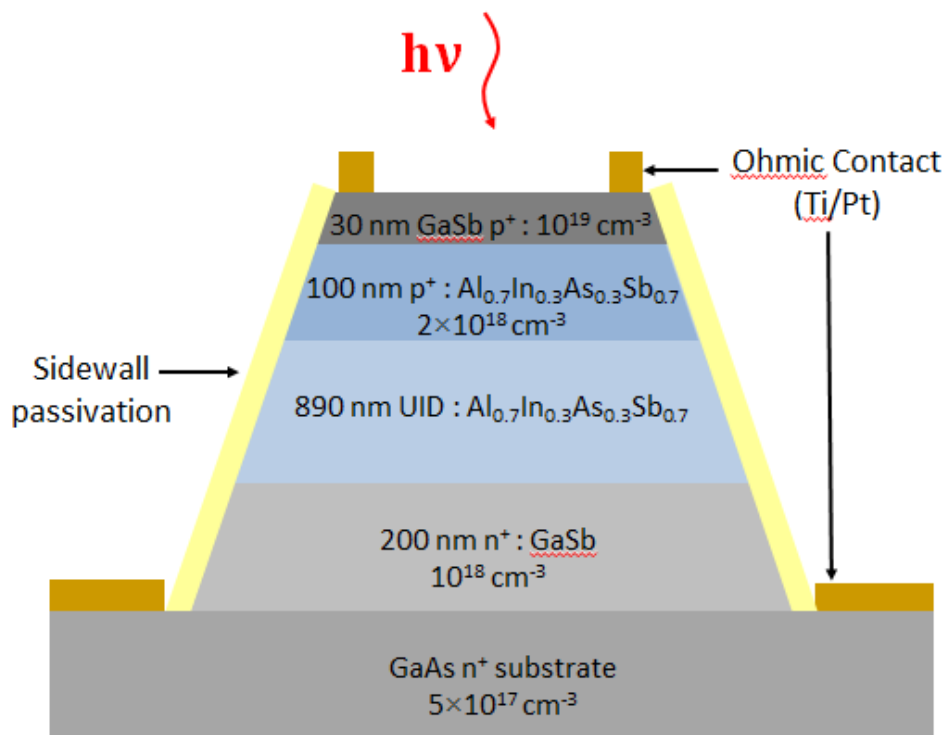
Figure 3-1: Cross-sectional schematic of $Al_{0.7}In_{0.3}As_{0.3}Sb_{0.7}$ avalanche photodiode.

3.3 Measurements

All measurements in this section were performed at room temperature, 300K. The current voltage characteristics are shown in Figure 3-2. The dark current was 4 nA (6×10^{-4} A/cm^2) at 90% of breakdown. The slight increase in photocurrent at low bias reflects the increase in depletion width in the n$^-$ layer. Capacitance-voltage measurements indicate this layer is fully depleted at -3 V, as shown in Figure 3-3. From -3 V and to -25 V, the photocurrent is relatively independent of the bias voltage; thus, the unity gain point of the device was designated as the photocurrent at -5 V bias. Breakdown occurred at a reverse bias of 40.5 V, corresponding to a peak electric field of ~530 kV/cm. The maximum stable gain reached before breakdown was 95.
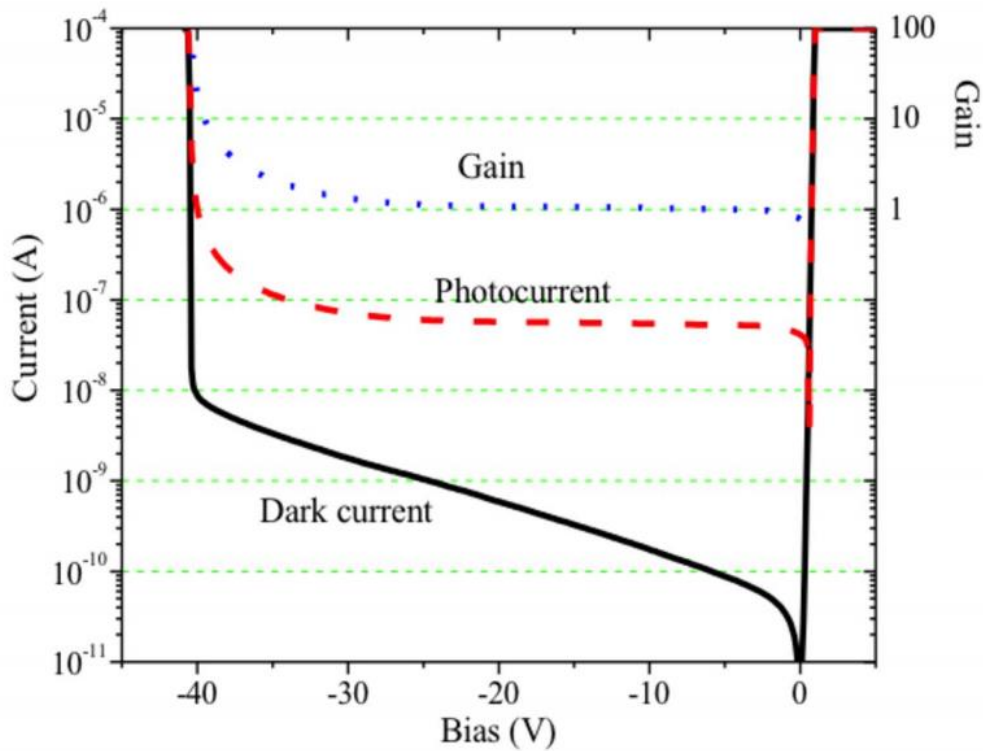
Figure 3-2: Dark current (solid line), photocurrent (dashed line), and gain (dotted line) versus bias for a 30 μm-diameter AlInAsSb avalanche photodiode.
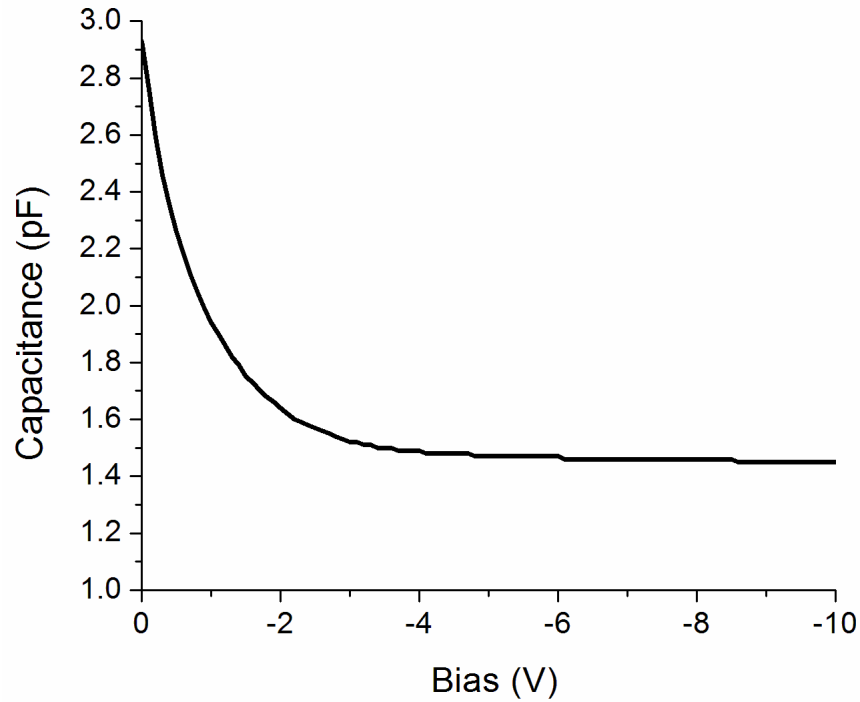
Figure 3-3: Measured capacitance versus bias of 100 um diameter $Al_{0.7}In_{0.3}As_{0.3}Sb_{0.7}$ device

  The total leakage current of the device can be expressed as the sum of surface leakage current and the multiplied dark current, as described in equation (1.2) in section 1.2.2 on dark current measurements. The dark current versus gain for a 30 µm-diameter device is shown in Figure 3-4. The linear fit corresponds to $I_{DS} \approx 6$ nA and $I_{DB} \approx 0.14$ nA. These measurements indicate that leakage is surface dominated; further studies of passivation techniques promise to push toward bulk leakage, further decreasing dark current values.
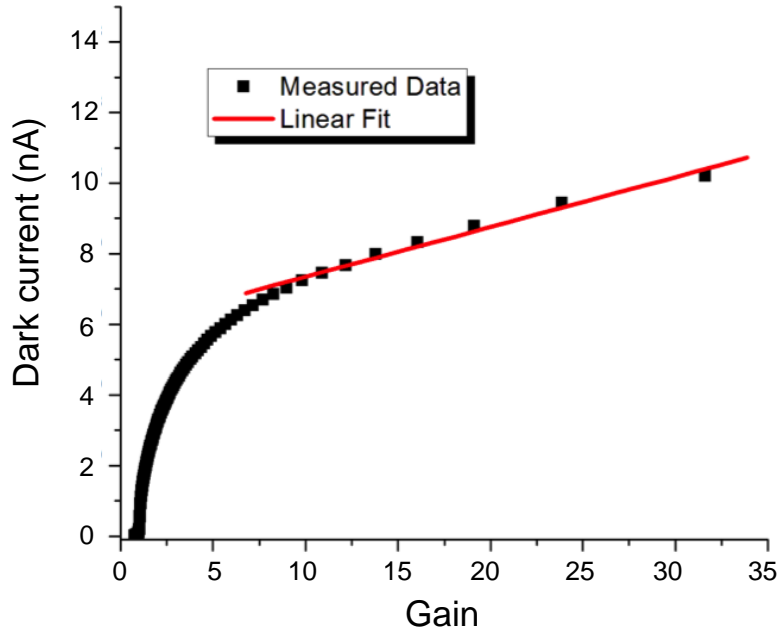
Figure 3-4: Dark current characteristics of 30 μm-diameter $Al_{0.7}In_{0.3}As_{0.3}Sb_{0.7}$ avalanche photodiode. The linear fit shows that the primary multiplied dark current is 6 nA, and the unmultiplied dark current, typically associated with surface leakage, is 0.14 nA

Figure 3-5 shows the external quantum efficiency versus wavelength at −5 V bias, the unity gain point of the device. Collection of electrons created by absorption in the GaSb top contact layer is poor due to surface recombination and a barrier at the $GaSb/Al_{0.7}In_{0.3}As_{0.3}Sb_{0.7}$ interface. Prior to removing the GaSb layer, the quantum efficiency is above 30% for wavelengths between 630 nm and 960 nm, peaking at 46% at 715 nm. After its removal, the efficiency increases as much as 20% from 500 nm to 850 nm, reaching ~68% near 700 nm. Note, however, that no anti-reflection coating has been added to these devices.

Assuming the absorption coefficient, currently unknown for this material system, is on the order of 10^4 cm^{-1} for visible wavelengths, since the air-semiconductor reflectivity without an antireflection coating is ~30%, a maximum efficiency of ~70% would be expected, which is close to the measured value. The long-wavelength cutoff is near 1.1 μm, which is similar to that of Si. However, silicon is an indirect bandgap material, while $Al_{0.7}In_{0.3}As_{0.3}Sb_{0.7}$ is a direct-

bandgap material. Thus, silicon APDs require long absorption regions to have high quantum efficiency, yielding a tradeoff between bandwidth and quantum efficiency in silicon photodiodes: B. Yang et. al. reported a high-speed Si APD with a bandwidth of 8 GHz, but the quantum efficiency was low, only about 11% [53]. M. Yang et. al. report a high quantum efficiency silicon APD, with a QE of about 68%, but the bandwidth was only 1.5 GHz [54].

Additionally, by changing the Al content in the $Al_x In_{1-x} As_y Sb_{1-y}$, the cutoff wavelength can be pushed beyond 1.6 μm, accommodating not only the 1.064 μm wavelength of Nd:YAG lasers, but also telecommunications wavelengths.
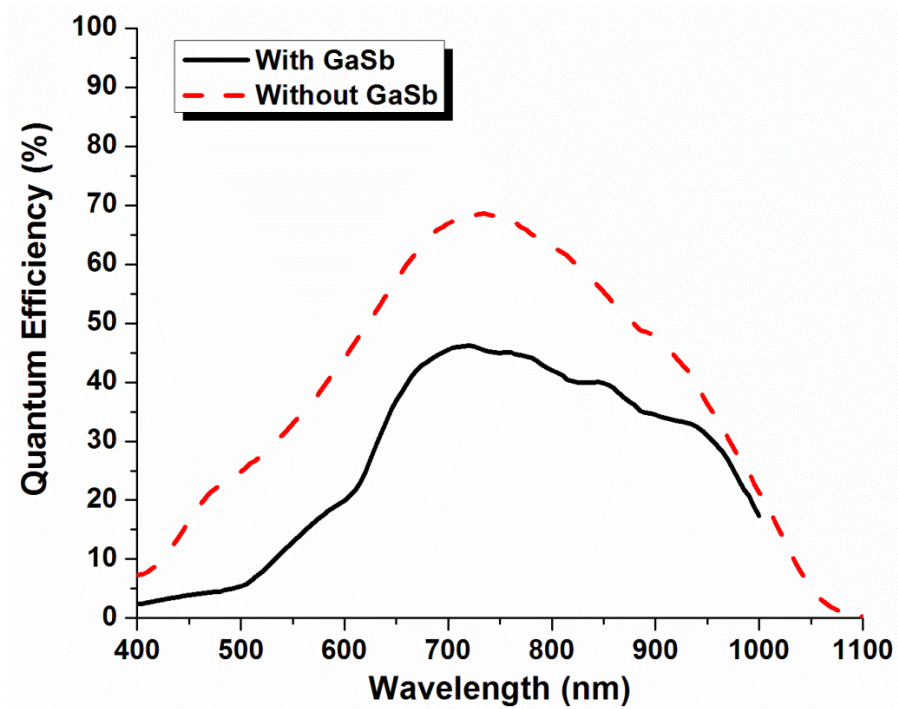
Figure 3-5: External quantum efficiency versus wavelength for devices with (solid black line) and without (dashed red line) the top GaSb layer.

The excess noise figure is shown as a function of the multiplication gain, for both an $Al_{0.7}In_{0.3}As_{0.3}Sb_{0.7}$ APD (■) and a Si APD (▲) in Figure 3-6, as measured by an HP 8970 noise figure meter. The solid lines are plots of the excess noise for k-values from 0 to 0.6 using the local-field model [13]. The measured $Al_{0.7}In_{0.3}As_{0.3}Sb_{0.7}$ APD excess noise corresponds to an

estimated k-value of 0.015 for the unity gain point at -5 V bias, and does not exceed 0.05 for

unity gain points chosen for biases up to -25 V, beyond which it is clear there is sufficient impact

ionization as to create gain.
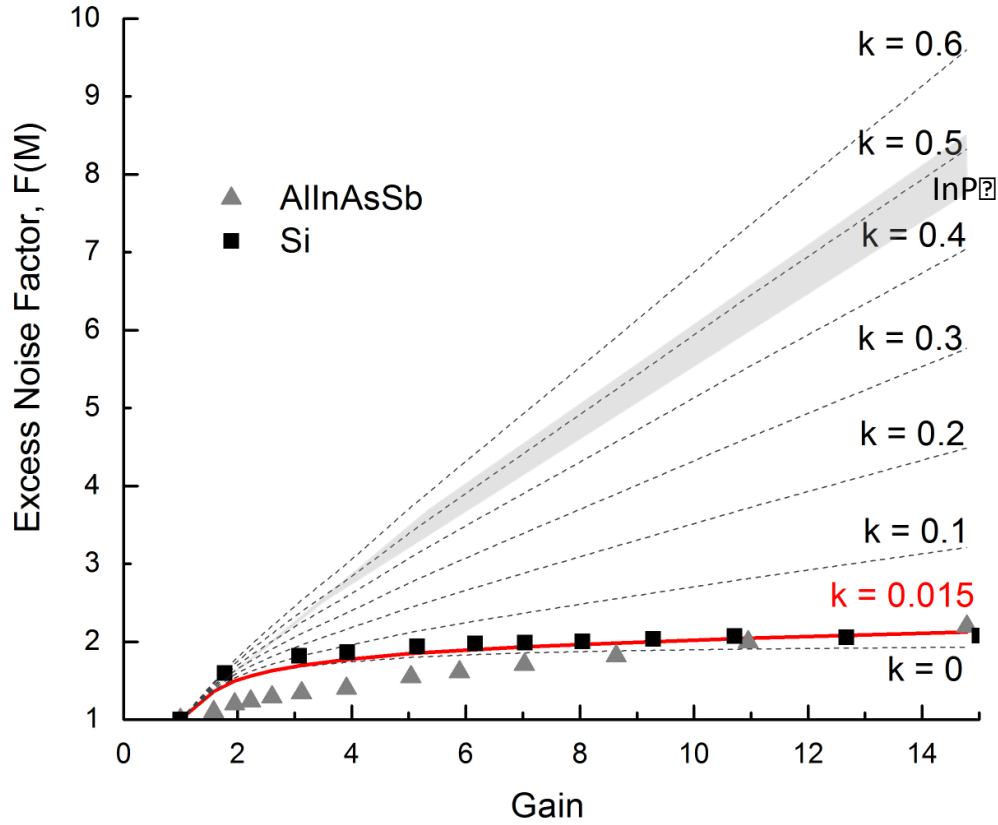
Figure 3-6: Measured excess noise factor versus gain for an $Al_{0.7}In_{0.3}As_{0.3}Sb_{0.7}$ APD (▲) and a Si APD (■). The solid lines are plots of the excess noise factor using the local field model for k-values from 0 to 0.5. Both the Si and $Al_{0.7}In_{0.3}As_{0.3}Sb_{0.7}$ APD are characterized by a k-value of 0.015. The shaded region for $k \geq 0.45$ denotes typical values for APDs that employ InP multiplication regions.

This k-value is comparable to the Si APD. For several decades, Si APDs have been the

standard for low noise; the k-values for commercial Si APDs fall between 0.02 and 0.06. InP is

the material most widely deployed for telecommunications APDs. InP typically exhibits k-values

between 0.45 and 0.52 [55] [56] [57], as denoted by the shaded region in Figure 3-6. These k-

values are for bulk materials; for high electric fields, as commonly found in the multiplication

regions of separate multiplication and absorption APDs, the k-values can be higher. Given the

relatively thick multiplication regions of the APDs reported here, I believe the measured k values reflect the bulk ionization characteristics of $Al_{0.7}In_{0.3}As_{0.3}Sb_{0.7}$. Low k-values have been observed for detectors manufactured from two of its constituent materials: InAs and InSb [47] [58] [59]. Additionally, previous studies have shown that the addition of Al to a material does not significantly increase its k-value, as with AlAsSb and InAlAs [20] [60]. Furthermore, initial Monte Carlo studies support the low k-value observed in measurements.

Given the measured k values of the $Al_{0.7}In_{0.3}As_{0.3}Sb_{0.7}$ APDs reported in this work, gain-bandwidth products comparable to those of Si, which have been reported to be as high as 340 GHz [61], were anticipated. However, our initial measurements of bandwidth for the $Al_{0.7}In_{0.3}As_{0.3}Sb_{0.7}$ devices gave a bandwidth of only 5 GHz at unity gain. By looking at the forward-biased current of this device, I extracted the value of the contact resistance, which was about 140 Ω. The capacitance of the 30 μm device was about 160 fF, yielding an RC-limited bandwidth of 5.2 GHz, according to equation 1.11. The transit-time-limited bandwidth should be substantially higher; however, in order to realize this bandwidth, the RC constant must be minimized. Since 30 μm is the minimum device size on our mask, and the value of the capacitance is relatively small, I focused on reducing the contact resistance.

The contact resistance of a device can be measured using TLM measurements, as described in section 1.2.1. I attempted to minimize contact resistance first by depositing varying thicknesses of various metals and alloying them across a range of temperatures. However, despite my efforts, the contact resistance did not decrease significantly. In these studies, I searched the literature for appropriate contact metals for GaSb, and found that my resistances were orders of magnitude higher than the literature [62]. This discrepancy led me to suspect that the GaSb p-contact layer was oxidizing. According to a literature search, our wafers, which, at

this point, had been on the shelf for over a year, exposed to air, likely had about 35-40 angstroms of GaSb oxide on them [63]. The removal of this oxidation would significantly improve the contact resistance of our devices. I performed a series of experiments in which I used different oxide removal treatments prescribed by literature [64] [65], primarily an HCl soak and a pre-mill prior to deposition, and repeated transmission line. A control device, with no treatment, showed a contact resistance of about 100 ohms. Both the HCl soak and pre-milling have shown promise in reducing contact resistance, but increasing the pre-mill and HCl soak times showed no significant effect on reducing contact resistance of these devices.

Treatment	$R_{contact}$
Control	102 Ω
5 min HCl soak	35 Ω
45 s pre-mill	35 Ω
5 min HCl + 45 s pre-mill	31 Ω
90 s pre-mill	39 Ω
5 min HCl + 90 s pre-mill	40 $\pm$ 2 Ω
180 s pre-mill	36 Ω
5 min HCl + 180 s pre-mill	35 Ω

At this point, I became concerned that the GaSb had fully oxidized, and in order to remove all the oxide from the wafer, I would need to remove the full thickness of GaSb, leaving only p-doped $Al_{0.7}In_{0.3}As_{0.3}Sb_{0.7}$ available as a contact layer, which has a wide bandgap that makes the formation of an ohmic contact challenging. To confirm my hypothesis, I defined circular mesas using photoresist and soaked the wafer in undiluted HCl for 3 minutes to remove oxidation. I then soaked the wafer in acetone to remove the photoresist, and observed the

material under a microscope, per the image in Figure 3-7. According to profilometer measurements, the mesa height of the wafer protected from the HCl etch ranges from 20 nm to 50nm, indicating that most if not all of the 30nm GaSb layer is fully oxidized. Additionally, profilometer measurements revealed the presence of deep pinholes, up to 150 nm in depth, indicating oxidation into the aluminum-containing layers below, likely from small lattice mismatches in the top GaSb layer during growth.
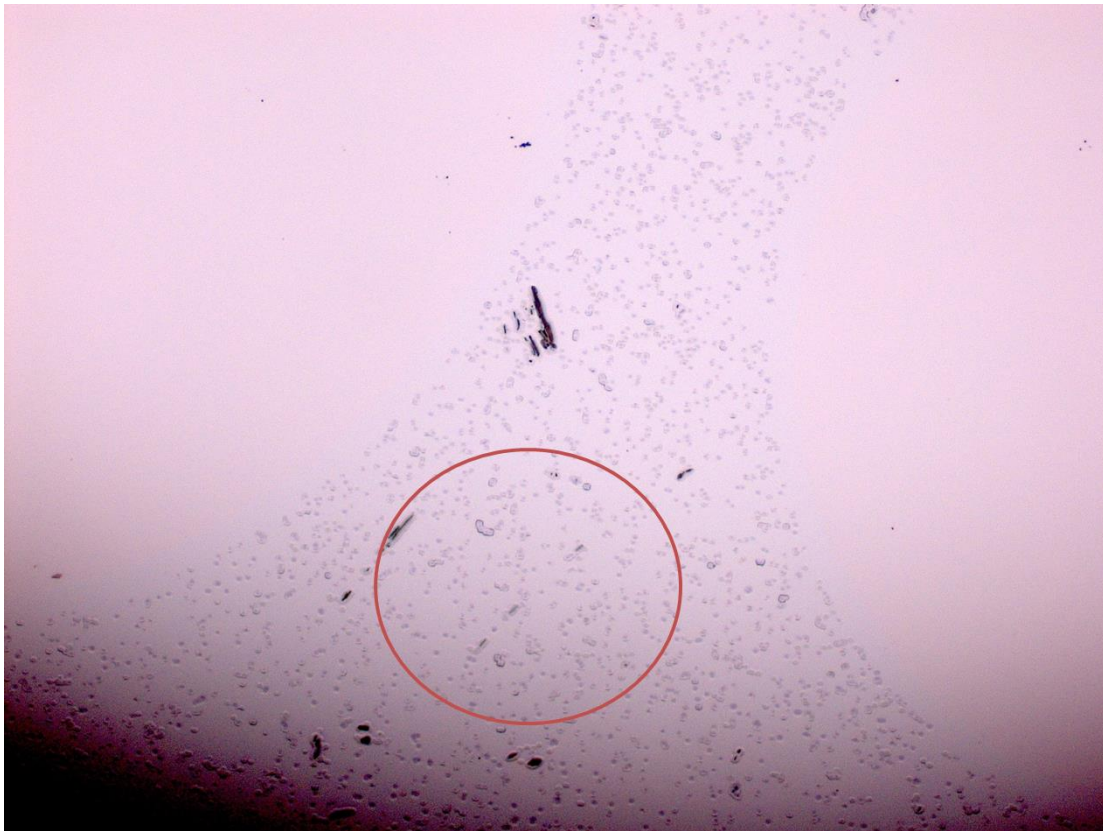
Figure 3-7: Wafer following HCl treatment. Circled area shows deep pinholes into AlInAsSb layer. Smooth, circular areas were covered in photoresist prior to HCl treatment.

Unfortunately, these results indicate that the available wafers cannot have lower resistance values, and thus, the devices will continue to be limited by the RC bandwidth. However, future growths of these homojunction APDs will be modified accordingly. One design will implement a significantly thicker layer of GaSb for the p-contact, a full 100 nm.

Additionally, oxidation could be mitigated through the use of an As cap or spun-on photoresist to protect the devices during transit and while on the shelf. Another option would be to use a different contact layer material, such as InGaAs. These are all candidates for future study, outlined in chapter 8.

3.4 Chapter Summary

I report low-noise avalanche gain from photodiodes composed of a previously uncharacterized alloy, $Al_{0.7}In_{0.3}As_{0.3}Sb_{0.7}$, grown on GaSb. The bandgap energy, and thus the cutoff wavelength, is similar to that of silicon. In addition, unlike other III-V avalanche photodiodes that operate in the visible or near infrared, the excess noise factor is comparable to or below that of silicon, with a k-value of approximately 0.015. However, there is a key difference between silicon and $Al_{0.7}In_{0.3}As_{0.3}Sb_{0.7}$: silicon is an indirect bandgap material, while $Al_{0.7}In_{0.3}As_{0.3}Sb_{0.7}$ is a direct-bandgap material. Silicon APDs require long absorption regions to have high quantum efficiency, sparking a huge tradeoff between bandwidth and quantum efficiency in silicon photodiodes. B. Yang et. al. reported a high-speed Si APD with a bandwidth of 8 GHz, but the quantum efficiency was low, only about 11% [53]. M. Yang et. al. report a high quantum efficiency silicon APD, with a QE of about 68%, but the bandwidth suffers greatly at only 1.5 GHz [54].

Since the bandgap of $Al_{0.7}In_{0.3}As_{0.3}Sb_{0.7}$ is direct, its absorption depth is 5 to 10 times shorter than indirect-bandgap silicon, potentially enabling significantly higher operating bandwidths while maintaining high quantum efficiency. Furthermore, the wide array of absorber regions compatible with GaSb substrates enables cutoff wavelengths ranging from 1 μm to 2 μm, which are detailed in the next chapter.

Chapter 4 $Al_xIn_{1-x}As_ySb_{1-y}$ Homojunction Photodiodes

4.1 Introduction

My studies of the $Al_{0.7}In_{0.3}As_{0.3}Sb_{0.7}$ homojunction structure gave promising results, leading us to design a series of $Al_xIn_{1-x}As_ySb_{1-y}$ (x = 0.3, 0.4, 0.5, 0.6, 0.7) p-i-n structures. Initial photoluminescence measurements of materials within the system promised to absorb at increasing energies with aluminum concentration, as shown in Figure 4-1. Aluminum concentrations equal to and above 30% were chosen, because these materials had not been grown previously as high quality materials. The 80% aluminum material was not characterized in this study, because the photoluminescence intensity drops sharply between 70% and 80% aluminum, suggesting a transition from a direct-bandgap material to an indirect-bandgap material.
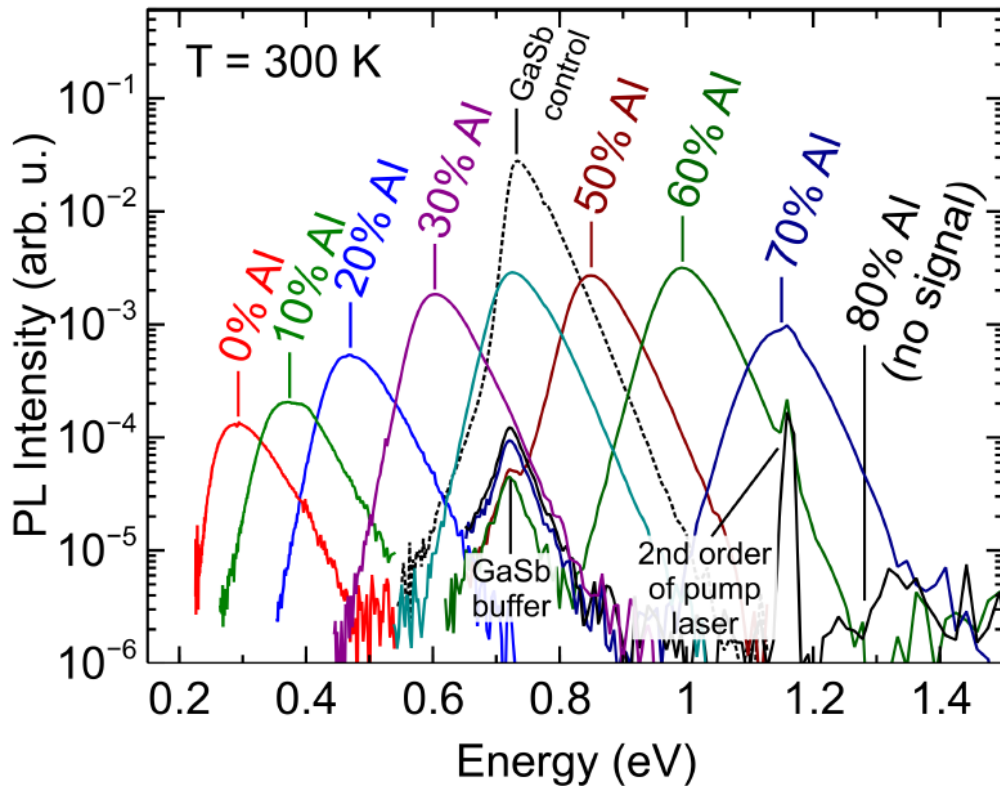
Figure 4-1: Photoluminescence spectra of AlInAsSb digital alloys on GaSb.

The homojunction structures were grown lattice-matched to GaSb substrates by Scott Maddox at the University of Texas. These APDs offer the advantages of III-V-compound direct-

bandgap materials with high absorption coefficients and a lattice-matched material system that provides the flexibility to design complex structures to maximize performance and enable operation in different spectral regions.

4.2 Structure and Fabrication

These devices follow the cross-sectional schematic shown in Figure 4-2, with a 900 nm thick i-region. Again, the top GaSb layer is used to reduce contact resistance, improve the contact adhesion, and to protect the underlying Al-containing layers from oxidation. I fabricated photodiodes according to the wet etch procedure outlined in Section 1.3.2.

Photons

SU-8 Coating

30 nm GaSb Na: 1×10^{19}

100 nm $Al_xIn_{1-x}As_ySb_{1-y}$ Na: 2×10^{18}

890 nm $Al_xIn_{1-x}As_ySb_{1-y}$ UID

200 nm GaSb Nd: 1×10^{18},

Ohmic Contact (Ti/Au)

GaAs n^+ substrate
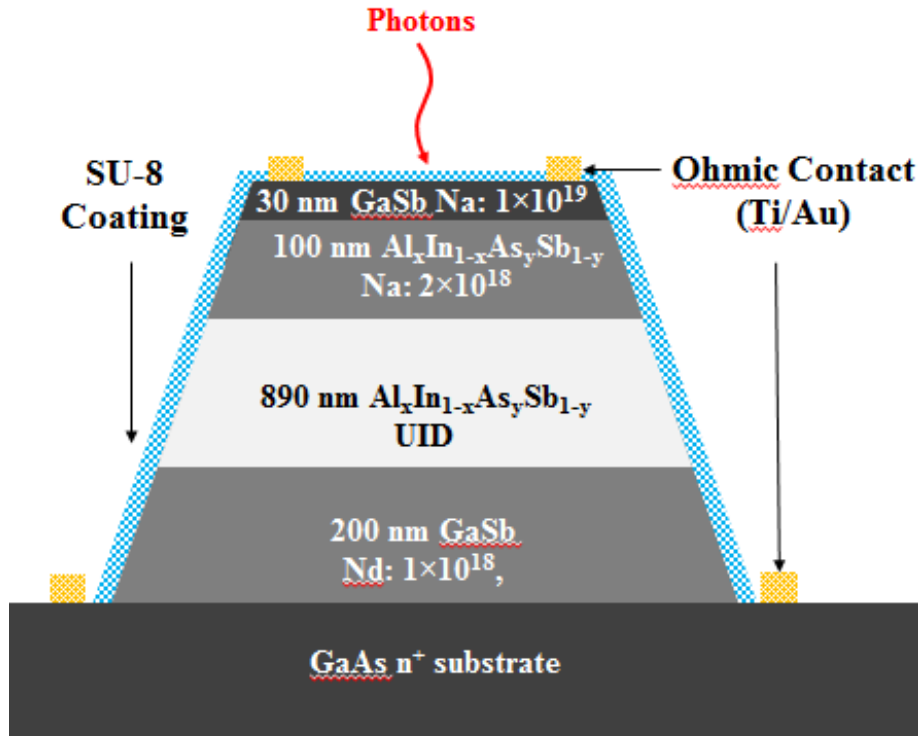
Figure 4-2: Cross-sectional schematic of $Al_xIn_{1-x}As_ySb_{1-y}$ APD.

4.3 Measurements

Figure 4-3 shows the dark current versus bias for 100 μm-diameter APDs of all five Al concentrations. Since the bandgap is dependent on the Al concentration [31], higher Al concentration APDs had lower dark current. Figure 4-4 shows dark current versus diameter for all compositions. For devices fabricated from materials with an Al concentration of 30%, 40%, and 50%, the dark currents increased quadratically with diameter, which suggests bulk-leakage-dominated dark currents. The 60% AlInAsSb APDs showed a mixture of quadratic and linear functions, implying that both bulk leakage and surface leakage contribute to dark current. The $Al_{0.7}In_{0.3}As_{0.3}Sb_{0.7}$ APDs exhibited a linear relationship between device diameter and dark current, suggesting surface leakage dominates; further study of passivation techniques promises to push the dark current down further, toward bulk leakage, in both 60% and 70% materials.
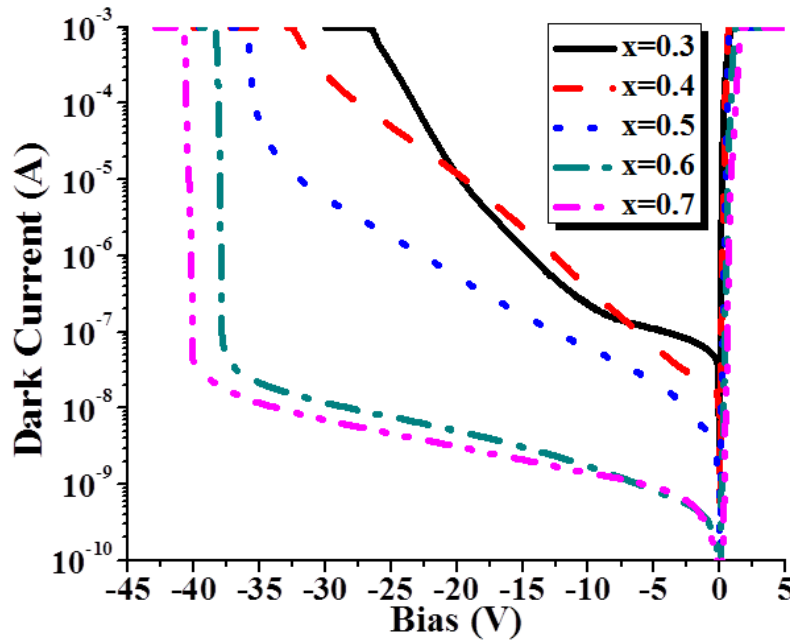
Figure 4-3: Dark currents versus bias voltage of $Al_xIn_{1-x}As_ySb_{1-y}$ APDs.
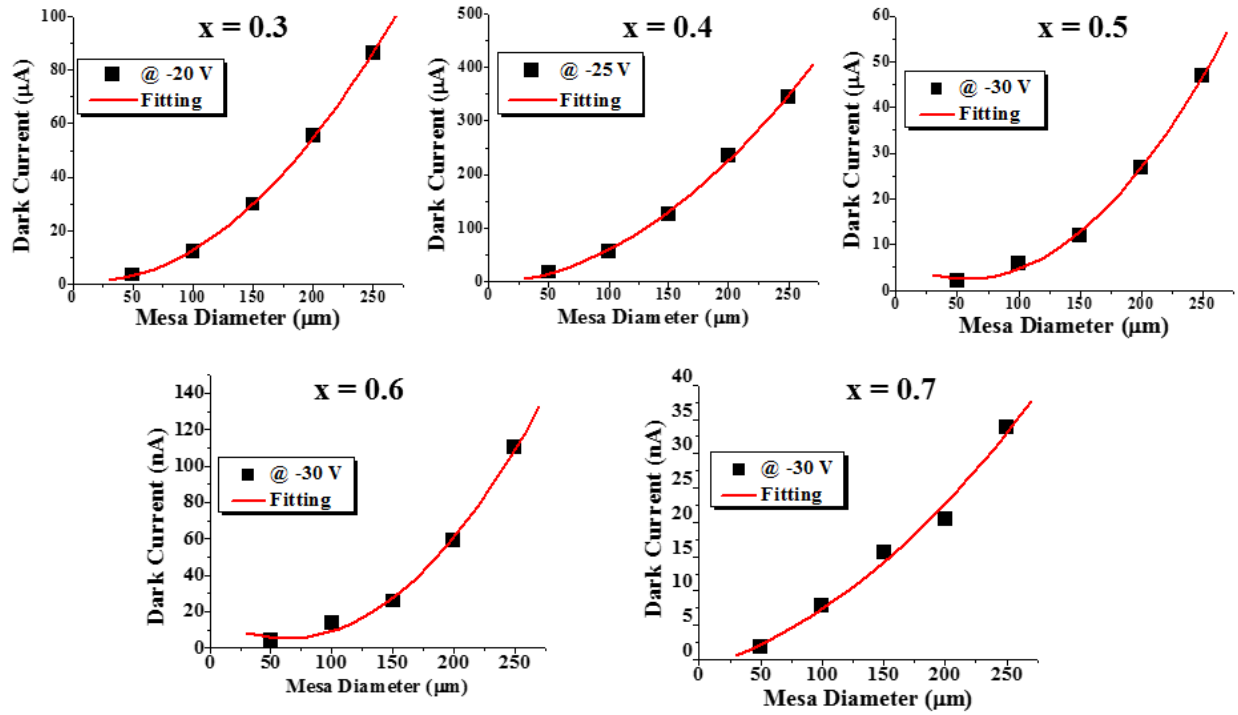
Figure 4-4: Dark current versus device diameter for AlInAsSb APDs. Results show that bulk leakage dominates for Al concentrations from 30% to 50%. However, the 60% Al material devices were neither fully linear nor quadratic, implying the dark current stems from a mixture of bulk and surface leakage. The $Al_{0.7}In_{0.3}As_{0.3}Sb_{0.7}$ material devices were dominated by surface leakage. Devices were measured at 300 K.

Figure 4-5 shows the capacitance-voltage measurements on 100 μm-diameter APDs. Since the i-regions of the homojunction APDs are unintentionally doped, the doping levels reflect the intrinsic impurities. The sharp drop in capacitance of $Al_{0.3}In_{0.7}As_{0.7}Sb_{0.3}$ and $Al_{0.4}In_{0.6}As_{0.6}Sb_{0.4}$ with respect to the slower capacitance drop in the other aluminum concentration devices suggests a lower intrinsic doping level in these two materials. Additionally, the capacitance is independent of voltage beyond a reverse bias of 5 V, indicating full depletion of the unintentionally doped i-region.
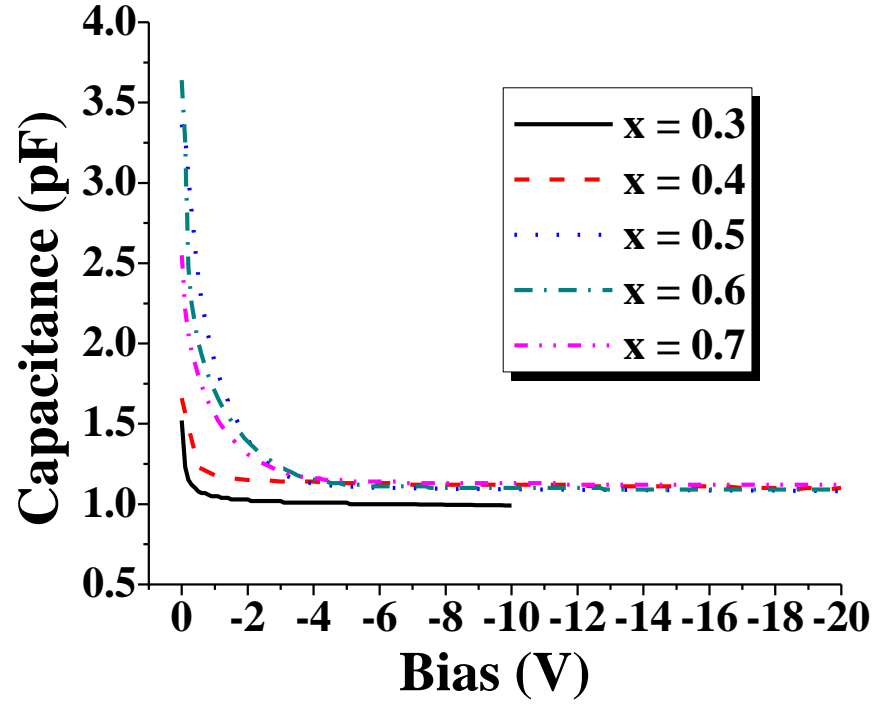
Figure 4-5: Measured capacitance versus bias for 100-um diameter homojunction structure $Al_xIn_{1-x}As_ySb_{1-y}$ APDs.

A 543-nm He-Ne CW laser was used to measure photocurrent and extract multiplication gain for all five devices. For these gain values, the unity gain point was taken as -5 V, a bias in a relatively flat region of the photocurrent versus bias curve, where the i-region is fully depleted. Gain values as high as 100 were achieved in 60% and 70% $Al_xIn_{1-x}As_ySb_{1-y}$, as shown in Figure 4-6. However, the 30%, 40% and 50% $Al_xIn_{1-x}As_ySb_{1-y}$ APDs failed to reach high, stable gains due to their higher dark currents.
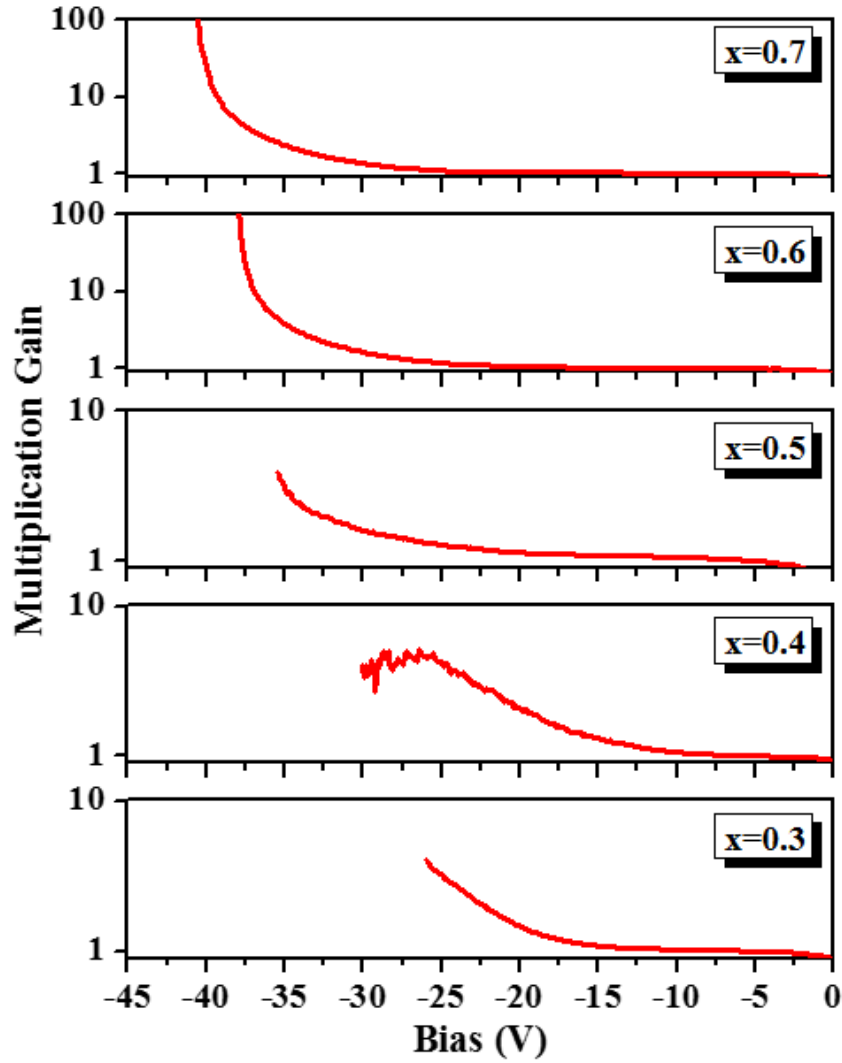
Figure 4-6: Multiplication gain versus bias for characteristic APDs fabricated from AlInAsSb system materials, measured at 300 K.

Next, we measured the external quantum efficiency for the devices across a range of wavelengths. For each material, we biased a 200 µm-diameter device to − 5V, using a measurement setup described in a Section 1.2.5. The measured data was referenced to a calibrated silicon photodiode. We first measured the quantum efficiency of the devices with the top GaSb layer. However, electron collection was poor, in part due to surface recombination, but also owing to a barrier at the GaSb/AlInAsSb interface. The GaSb was removed by soaking for a few seconds in AZ 400 MIF, a photoresist developer known to also etch GaSb [66]. After

removing the GaSb, the efficiency increased substantially, particularly in the $Al_{0.7}In_{0.3}As_{0.3}Sb_{0.7}$ structure, as much as 20% for wavelengths near the short-wavelength cutoff.

The results for the quantum efficiencies for all five materials with and without the top GaSb layer are shown in Figure 4-7 and Figure 4-8, respectively. We note that these devices do not have anti-reflection coatings. If the absorption coefficient (currently unknown for this material system) is on the order of 10^4 cm^{-1}, a maximum quantum efficiency value of 70% is expected, due to a 30% loss from to air-semiconductor reflectivity.
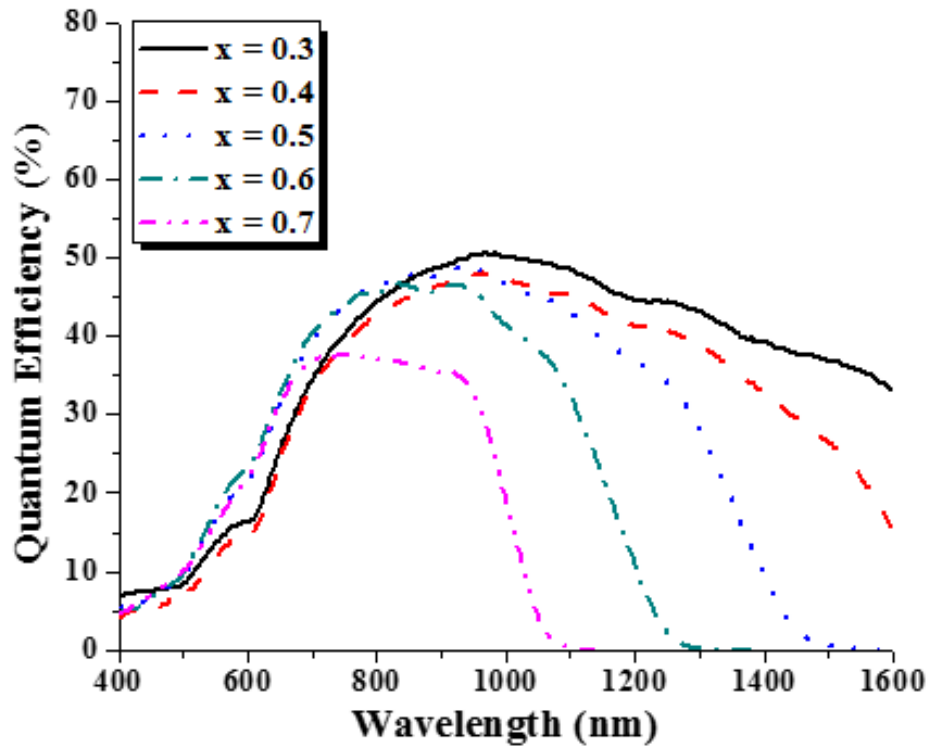
Figure 4-7: Measured external quantum efficiency of $Al_xIn_{1-x}As_ySb_{1-y}$ APDs with GaSb top layer. All data was measured with 200-μm APDs at 300 K.
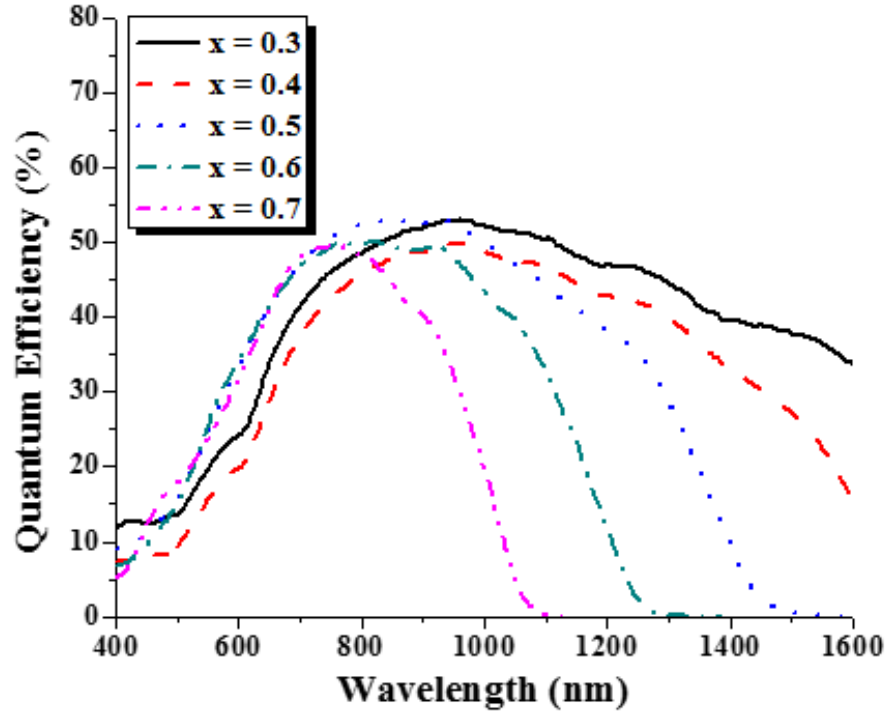
Figure 4-8: Measured external quantum efficiency of $Al_xIn_{1-x}As_ySb_{1-y}$ APDs without GaSb top layer. All data was measured with 200-μm APDs at 300 K.

Figure 4-9 shows the excess noise figure as a function of the multiplication gain for three of the five AlInAsSb APDs, as well as a calibrated Si APD. Measurements were performed using the system described in Section 1.2.4. The solid lines show plots of the excess noise for k-value ranging from 0 to 0.6 using the local-field model [13]. Measurements for the 30 and 40% AlInAsSb APD could not be performed due to dark current limitations of the noise figure meter, and measurements for the 50% AlInAsSb APD could not be performed at high multiplication gains for the same reason. The AlInAsSb APDs show excess noise factors that correspond to an estimated k-value of 0.01-0.05. As is clear from Figure 4-9, this k-value is comparable to that of Si, which has been the standard for low noise for several decades. The k-values for commercial Si APDs fall between 0.02 and 0.06, while InP typically exhibits k-values between 0.4 and 0.5, and InAlAs generally yields k value between 0.2 and 0.3, as denoted by the shaded regions.
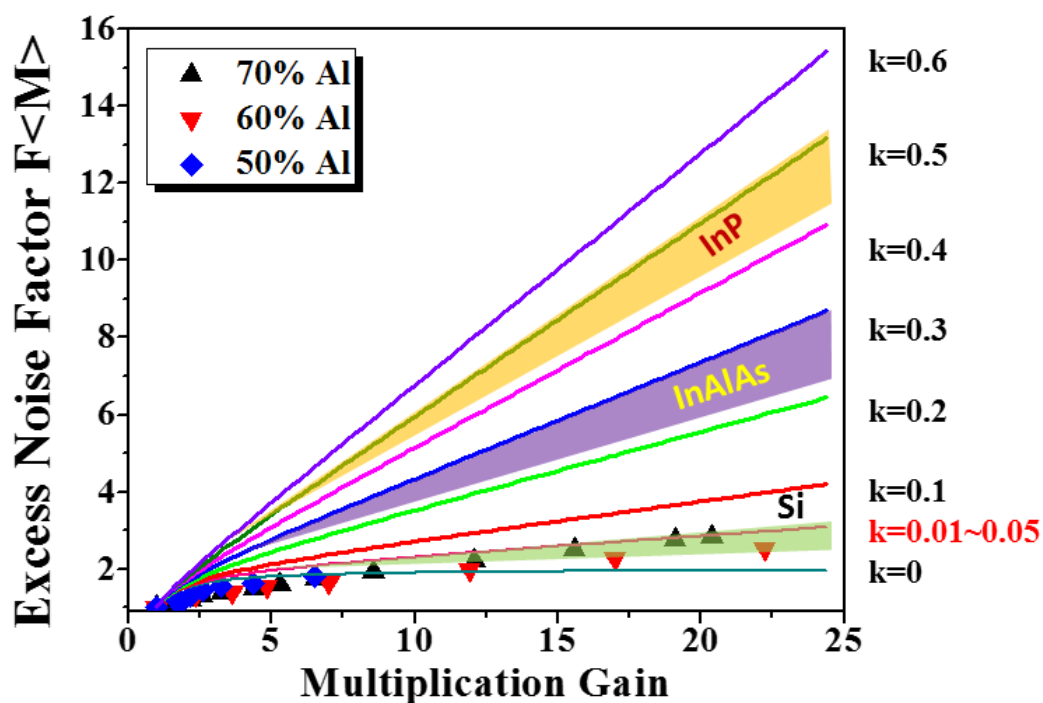
Figure 4-9: Measured excess noise factor versus gain for 50%, 60%, and 70% AlInAsSb APDs and a Si APD. Solid lines show the excess noise factor using the local field model for k-values from 0 to 0.6. The shaded region indicates typical values for APDs that employ InP, InAlAs, and Si multiplication regions.

4.4 Chapter Summary

$Al_xIn_{1-x}As_ySb_{1-y}$ materials offer low noise and high gain for a direct-bandgap material that can be lattice-matched to detect with sufficient optical response across wavelengths ranging from 0.4 μm to beyond 1.6 μm, covering most VCSELs, DFB lasers, solid-state lasers, and fiber lasers. By selecting a suitable Al concentration or combining multiple concentrations into a separate absorption, charge, and multiplication (SACM) APD. In a SACM APD, one material is used for absorption, another for multiplication; the two are separated by a charge layer to maintain low electric field in the absorption layer and high electric field in the multiplication region. Thus, one can easily build high-responsivity APDs for a desired wavelength for both optical communication and sensing applications. It is clear that the $Al_{0.7}In_{0.3}As_{0.3}Sb_{0.7}$ APDs exhibit excess noise comparable to Si and superior to InP [55] [56] [57]. In addition, this lattice-matched material system provides the flexibility to design complex structures to maximize performance and enable operation in different spectral regions. These qualities promise to create a potentially higher-speed device than Si, with lower noise than both InP and InAlAs, which could detect at telecommunications wavelengths.

Chapter 5 $Al_xIn_{1-x}As_ySb_{1-y}$ Separate Absorption, Charge, and Multiplication Avalanche Photodiodes

5.1 Introduction

There are three key components to creating a high-quality communications APD. First, the material chosen must have a low k-value in order to achieve low excess noise and high gain bandwidth product [8]. Second, the APD must have low dark current. Finally, and perhaps most obviously, is that the APD must operate at communications wavelengths, namely at 1550 nm for the lowest optical fiber loss.

Historically, silicon has been used for a wide variety of applications, but it is not a good candidate for communications wavelengths as its bandgap dictates a long-wavelength cutoff ~ 1μm. Some groups have used strained germanium as an absorber and silicon as the multiplication region [61] [67] [68] [32]. This approach works well in terms of keeping the excess noise low, but the lattice mismatch between the Ge and Si results in high trap densities, and thus high dark current. InAs has also been the focus of several studies, because it shows great promise for low excess noise, but it exhibits high dark current due to its low bandgap. InP and InAlAs have both been used as multiplication materials with InGaAs absorption regions [69] [70] [71] [72] [73] [20] [57] [74] [75] [76] [77] [78] [79] [80] [81] [82]. However, the high k-value of InP gives rise to high noise and limited gain-bandwidth products [55] [56] [57] [81] [82] [79] [80]. InAlAs provides a lower noise multiplication region, but still has relatively high dark current [73] [83] [57] [74] [75] [76] [77] [78].

Though some of the AlInAsSb homojunction structures have low-noise characteristics, the cutoff wavelength does not extend to the communications wavelengths. Homojunction structures of the 40% quaternary material can operate at communications wavelengths, but their narrow bandgap gives rise to excessive tunneling at the high electric fields required for impact

ionization. By combining the two materials, using a 40% AlInAsSb absorber to inject into a lattice-matched $Al_{0.7}In_{0.3}As_{0.3}Sb_{0.7}$ multiplication region, we designed separate absorption, charge, and multiplication (SACM) APDs from the $Al_xIn_{1-x}As_ySb_{1-y}$ materials system, in order to achieve low dark current, low noise, and operating wavelengths out to the short-wavelength infrared spectrum.

5.2 Structure and Fabrication
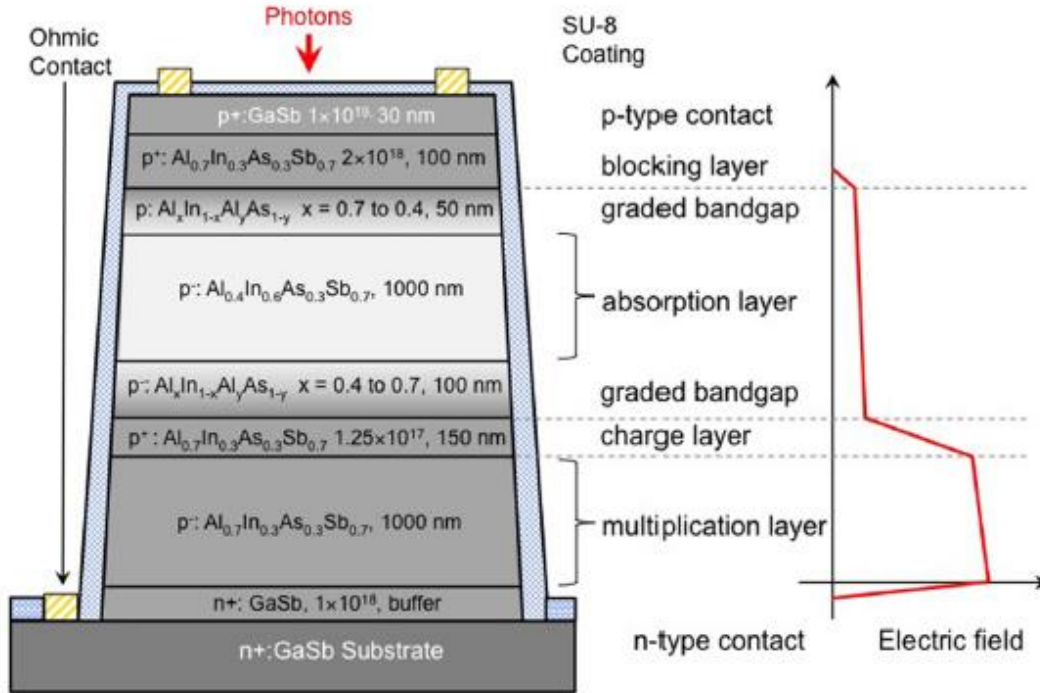
Figure 5-1: Schematic cross-section and electric field profile of $Al_xIn_{1-x}As_ySb_{1-y}$ SACM APD.

The structure of the SACM APD is shown in Figure 5-1. The top GaSb is used for p-contacts and to prevent oxidation in the underlying aluminum-containing layers. Beneath the p-type contact layer is a 100 nm p^+ $Al_{0.7}In_{0.3}As_{0.3}Sb_{0.7}$ blocking layer, graded to a p^- $Al_{0.6}In_{0.4}As_{0.4}Sb_{0.6}$ absorption layer, then back to a p^+ $Al_{0.7}In_{0.3}As_{0.3}Sb_{0.7}$ charge layer. Below the charge layer are a p^- $Al_{0.7}In_{0.3}As_{0.3}Sb_{0.7}$ multiplication layer, an n^+ GaSb buffer layer, and an n^+ GaSb substrate. Under reverse bias, owing to the charge layer, the electric field in the absorption layer is kept low enough to suppress tunneling, but high enough in the multiplication layer to initiate impact ionization events. Devices were grown and fabricated according to the standard process, but with N_2/Cl_2 inductive coupled plasma (ICP) dry etching instead of the conventional wet etching technique, using a SiO_2 hard mask to define mesas. Etching was followed by a surface-smoothing treatment of dilute bromine methanol.

5.3 Measurements

Figure 5-2a shows the photocurrent, dark current, and gain versus bias voltage of a 50 μm-diameter SACM APD. At 95% breakdown, the dark current is ~ 120 nA, which is approximately 100 times lower than that of Ge on Si APDs and comparable to that of AlInAs/InGaAs APDs [61] [67] [68] [32] [72] [20]. Gain values as high as 50 are observed before dark current inhibits further gain.

Using the values from the C-V measurement, I was able to calculate the depletion width versus bias as shown in Figure 5-2(b). The step in the photocurrent at a bias near -38 V occurs because the edge of the depletion region "punches through" to the absorbing layer, facilitating charge transport. The electric field is high enough to achieve gain prior to punchthrough, making it difficult to find a unity gain point and thus calculate the gain in the device. By fitting the excess noise using the algorithm reported by Liu et al. [84], the gain at punch-through was determined to be 1.7. This fit was confirmed by comparing responsivities with a homojunction $Al_{0.4}In_{0.4}As_{0.6}Sb_{0.4}$ photodiode that has the same absorption layer length (1000 nm), as well as measurements of the gain in an $Al_{0.7}In_{0.3}As_{0.3}Sb_{0.7}$ homojunction APD at the same electric field. The plot of dark current versus diameter in Figure 5-3 indicates that the dark current is dominated by surface leakage, implying that dark current could be further mitigated through finer-tuned processing steps.
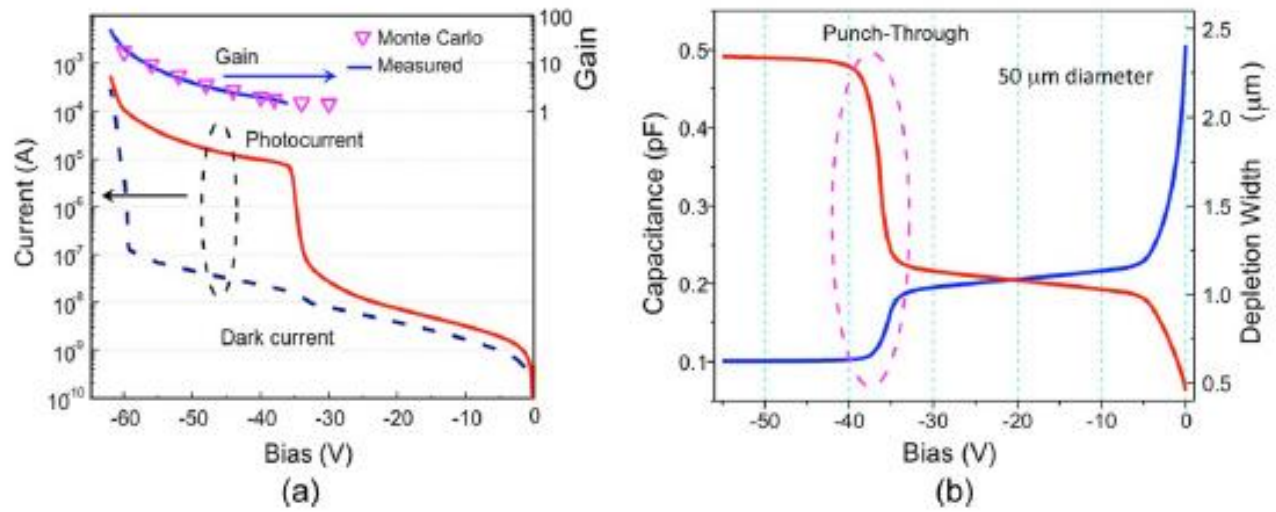
Figure 5-2: (a) Dark current, photocurrent, measurement and simulation data ($\triangledown$) of gain versus reverse bias of a 50 µm-diameter $Al_xIn_{1-x}As_ySb_{1-y}$ SACM APD at300K. The significant change of capacitance and depletion width at approximately 38V indicates that electric field has depleted the charge layer and entered into absorption layer.
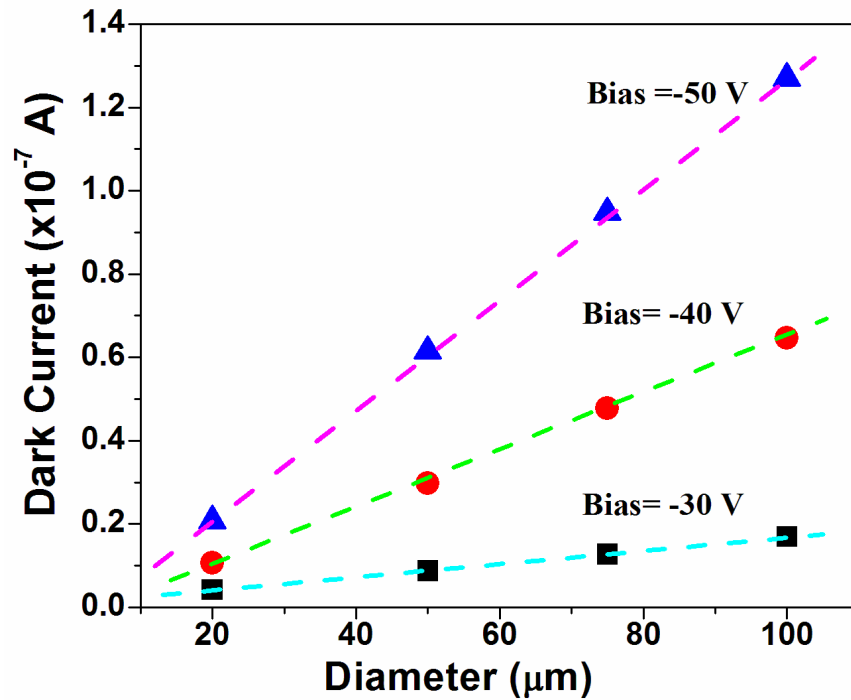
Figure 5-3: Dark current size dependence study of $Al_xIn_{1-x}As_ySb_{1-y}$ SACM APDs at 300K. Results show that dark current increases linearly with diameter for three different biases, indicating the dark current is dominated by surface leakage.

The normalized quantum efficiency for a 150 µm-diameter SACM APD was measured at a bias of -38 V, at room temperature, the results of which are shown in Figure 5-4. Again, as with our quantum efficiency measurements for the p-i-n structures, AZ 300 MIF developer was used to remove the top GaSb prior to measurement [33]. The optical cutoff wavelength for the device was above 1.6 µm. The device measured had no anti-reflection coating, with no back reflection, and an absorption layer of only 1000 nm, all of which could be addressed to improve quantum efficiency.
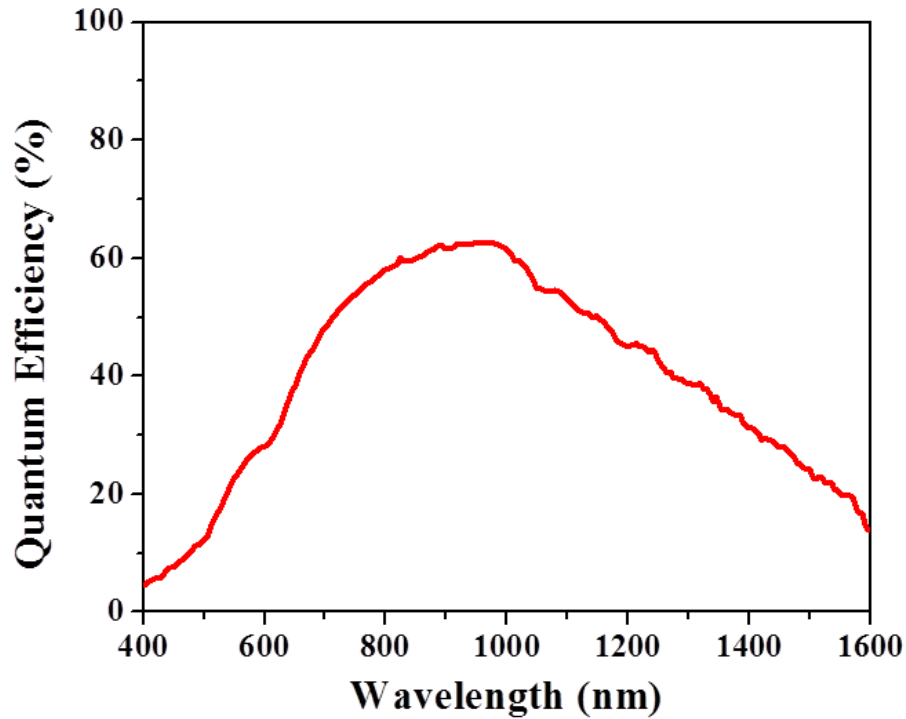
Figure 5-4: External quantum efficiency versus wavelength of a 150 µm-diameter $Al_xIn_{1-x}As_ySb_{1-y}$ SACM APD at 300 K.

The measured excess noise figure is shown as a function of gain in Figure 5-5 for both the SACM APD (▲) and a commercial Si APD (■), as well as solid lines, which plot the excess noise for k-values ranging from 0 to 0.6 according to the local-field model [13]. The measured

excess noise corresponds to an estimated k-value of 0.01, comparable to or less than that of a Si APD [85] [86].
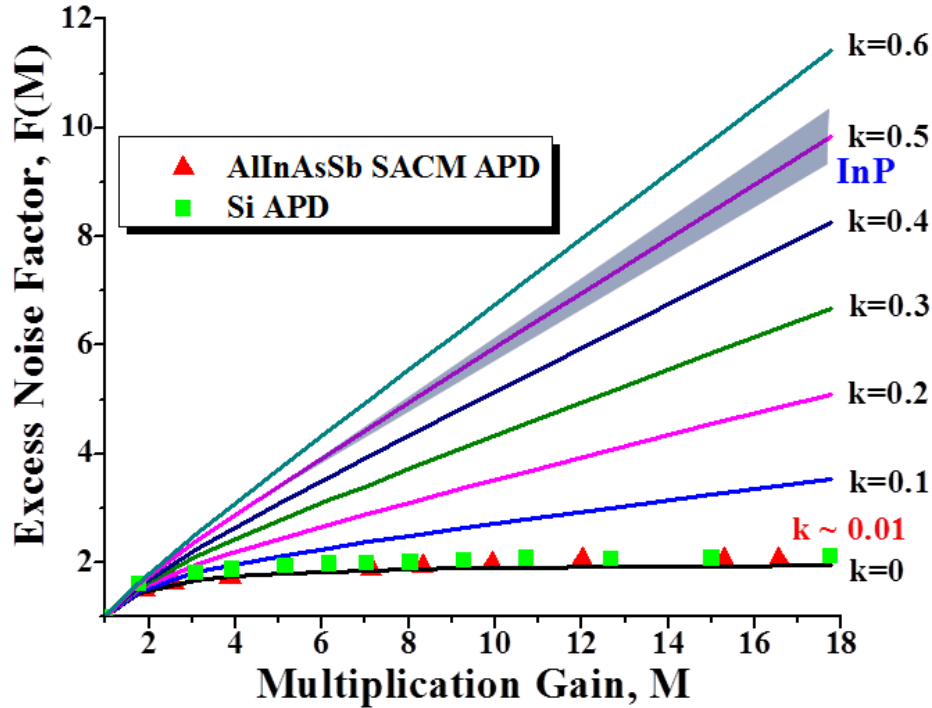
Figure 5-5: Measured excess noise versus gain for a 50 μm $Al_xIn_{1-x}As_ySb_{1-y}$ SACM APD (▲) and a commercial Si APD (■). The solid lines show the excess noise factor using the local field model for k-values from 0 to 0.6. The shaded region indicates typical values for APDs that employ InP multiplication regions.

We also performed preliminary bandwidth studies for the SACM structure, of which representative results are shown in Figure 5-6. Given the measured k values of the $Al_{0.7}In_{0.3}As_{0.3}Sb_{0.7}$ multiplication region reported in this work, we again expected gain-bandwidth products comparable to those of Si. These preliminary measurements, however, yielded bandwidths of only ~5.5 GHz at unity gain. Again, an investigation into the contact resistance of the device confirmed the bandwidth is RC-limited. Since the SACM devices oxidized at the same rate as the homojunction APDs, a series of simple HCl etches and imaging

showed pin holes similar to that reported in section 3.3. A proposed structure for future studies of

the SACM bandwidth is included in section 8.1.
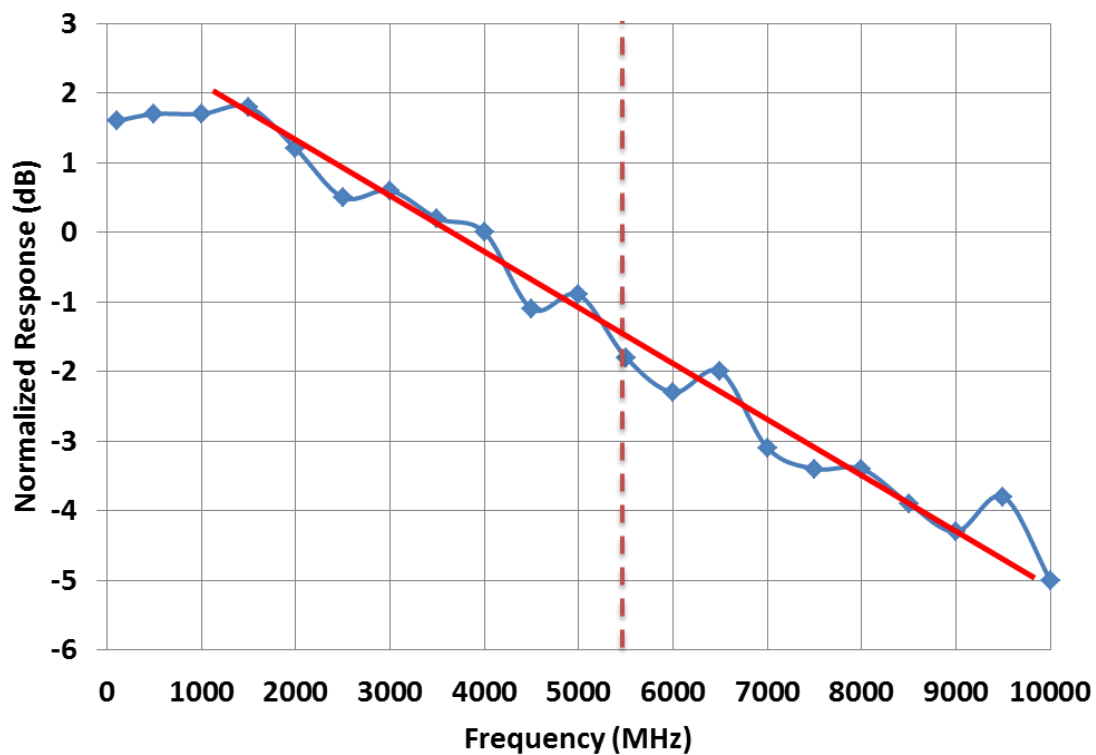
Figure 5-6: Normalized power versus frequency for a 50 μm diameter device. -3dB bandwidth is ~5.5 GHz.

5.4 Chapter Summary

Material Features	Si	Si (Ge)	InAs	InP (InGaAs)	InAlAs (InGaAs)	AlInAsSb (SACM)
Dark Current (Normalized with Gain)	~2 nA/cm²	~100 mA/cm²	~250 mA/cm²	~1 µA/cm²	~5 mA/cm²	220 µA/cm²
Excess Noise (k)	0.01~0.05	0.05~0.09	0	0.4~0.5	0.2~0.3	0.01~0.02
Spectra Response	UV~ 1.1 µm	Visible ~ 1.7 µm	Visible ~ >2 µm	Visible ~ 1.67 µm	Visible ~ 1.67 µm	>1.6 µm

Figure 5-7: Current state of the art for communications wavelength APDs.

A high-quality communications APD must exhibit low k-value, low dark current, and operate at communications wavelengths. The current state of the art for communications wavelength APDs is summarized in Figure 5-7. Silicon has been used for a wide variety of applications, but its bandgap dictates a long-wavelength cutoff ~ 1µm. Some groups have used strained germanium as an absorber, injecting carriers into a silicon layer for multiplication [61] [67] [68] [32]. This approach works well in terms of minimizing excess noise, but the lattice mismatch between the layers results high dark current. InAs, too, is a low excess noise material, and absorbs in the IR region, but it exhibits high dark current due to its low bandgap. InP and InAlAs have both been used as multiplication materials with InGaAs absorption regions [69] [70] [71] [72] [73] [20] [57] [74] [75] [76] [77] [78] [79] [80] [81] [82]. However, the high k-value of InP gives rise to high noise and limited gain-bandwidth products [87] [57] [55] [79] [80] [81] [82]. InAlAs provides a lower noise multiplication region, but still has relatively high dark current when grown with InGaAs [73] [20] [57] [74] [75] [76] [77] [78]. By combining the two materials, using a 40% AlInAsSb absorber to inject into a lattice-matched $Al_{0.7}In_{0.3}As_{0.3}Sb_{0.7}$

multiplication region, we created separate absorption, charge, and multiplication (SACM) APDs from the $Al_xIn_{1-x}As_ySb_{1-y}$ materials system, with low dark current, low noise, and operating wavelengths out to the short-wavelength infrared spectrum, filling a need in the telecommunications APD market. However, the RC-limitation of the bandwidth of this device requires future investigation into minimizing the contact resistance and taking the device to its transit time limit.

Chapter 6 Low-Noise, High Gain Tunneling Staircase Photodiode

6.1 Introduction

In addition to studying the AlInAsSb materials system in homojunction and SACM APDs, we extended our study of the staircase APD by creating a staircase device with two steps. The relationship between the number of steps in a staircase APD and its gain is quadratic, in theory. Each n-steps in a staircase APD, should provide a gain of 2 to the nth power. For example, a single step staircase should provide a gain of 2. Similarly, a staircase with two steps should provide a gain of 2^2, or 4, as shown by Figure 6-1. The first carrier will travel along the multiplication region, impact ionize at the first band offset, forming two carriers, both of which will travel to the second step, forming two more carriers, for a total of 4 carriers per one input. However, our initial results for our two-step staircase structure showed something somewhat startling – we observed gains much higher than expected. Though we initially expected this was due to a voltage dependent responsivity, we were able to rule that hypothesis out, and pursued another idea: field enhanced tunneling.
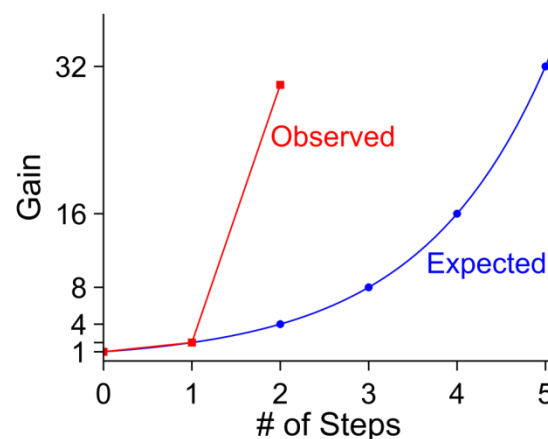
Figure 6-1: Measured scaling of staircase APDs with the number of steps (red), compared with the expected scaling (blue).

In the two-step structure we fabricated, though the device did not act as a traditional staircase APD, it did provide some interesting physics. Figure 6-2 illustrates the proposed device physics of this tunneling photodiode. Under reverse bias, the electric field begins to deplete the device from right to left, first flattening the step on the right, while the first step retains a valley in the conduction band. The absorption of photons generates electrons and holes, which drift in opposite directions according to the electric field across the device, but as the electrons drift into the top step, they are trapped in this valley. These trapped electrons create high negative space charge in this area, enhancing the field in the second step. This increased field allows electron to tunnel from the valence band of the bottom step into the conduction band. In essence, the device functions as a gateless tunneling phototransistor, where the top step localizes charge to tilt the field, hence tunneling, in the bottom step.
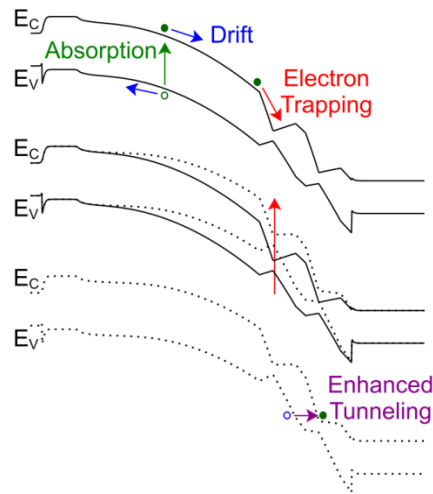
Figure 6-2: Illustration of the "photoconductive" gain mechanism under reverse bias. (top) Photogenerated electrons diffuse from the p-absorber and are captured in the top potential well and are trapped because the applied electric field is insufficient to reach the flatband "staircase" bias condition (Fig. 1b), leading to (middle) an increased field in the bottom staircase step, which triggers enhanced band-to-band tunneling in the bottom step (bottom).

6.2 Structure and Design
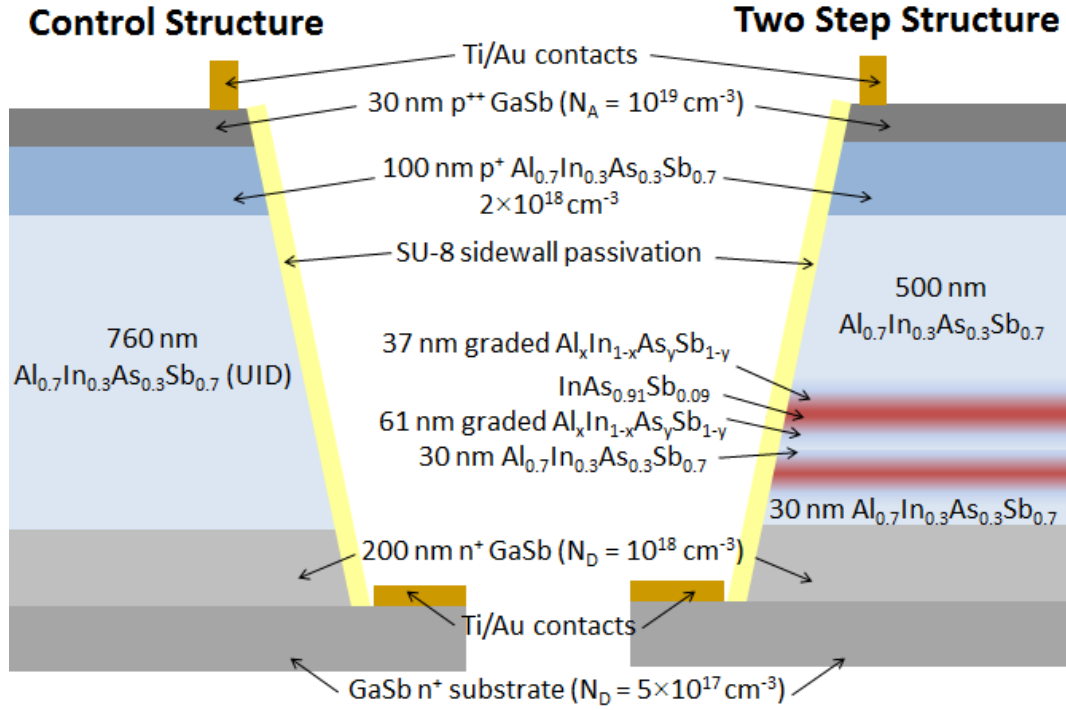
Figure 6-3: Cross-sectional schematic of AlInAsSb control structure (left) and two-step tunneling staircase (right).

The structure of the control and two-step tunneling devices are shown in Figure 6-3. Following growth, we also sent a sample of the wafer for SIMS analysis to confirm the concentrations of constituent materials, the results of which are shown in Figure 6-4. The control structure consists solely of the $Al_{0.7}In_{0.3}As_{0.3}Sb_{0.7}$, capped on either end with GaSb, on a GaSb substrate. The two step staircase structure features two constrictions at which the $Al_{0.7}In_{0.3}As_{0.3}Sb_{0.7}$ is graded down to $InAs_{0.91}Sb_{0.09}$, then back to $Al_{0.7}In_{0.3}As_{0.3}Sb_{0.7}$. Since the bandgap of InAsSb is smaller than that of $Al_{0.7}In_{0.3}As_{0.3}Sb_{0.7}$, this forms two constrictions in the band structure. The structures were grown and fabricated according to the processes outlined in chapter 1, using wet etching techniques.
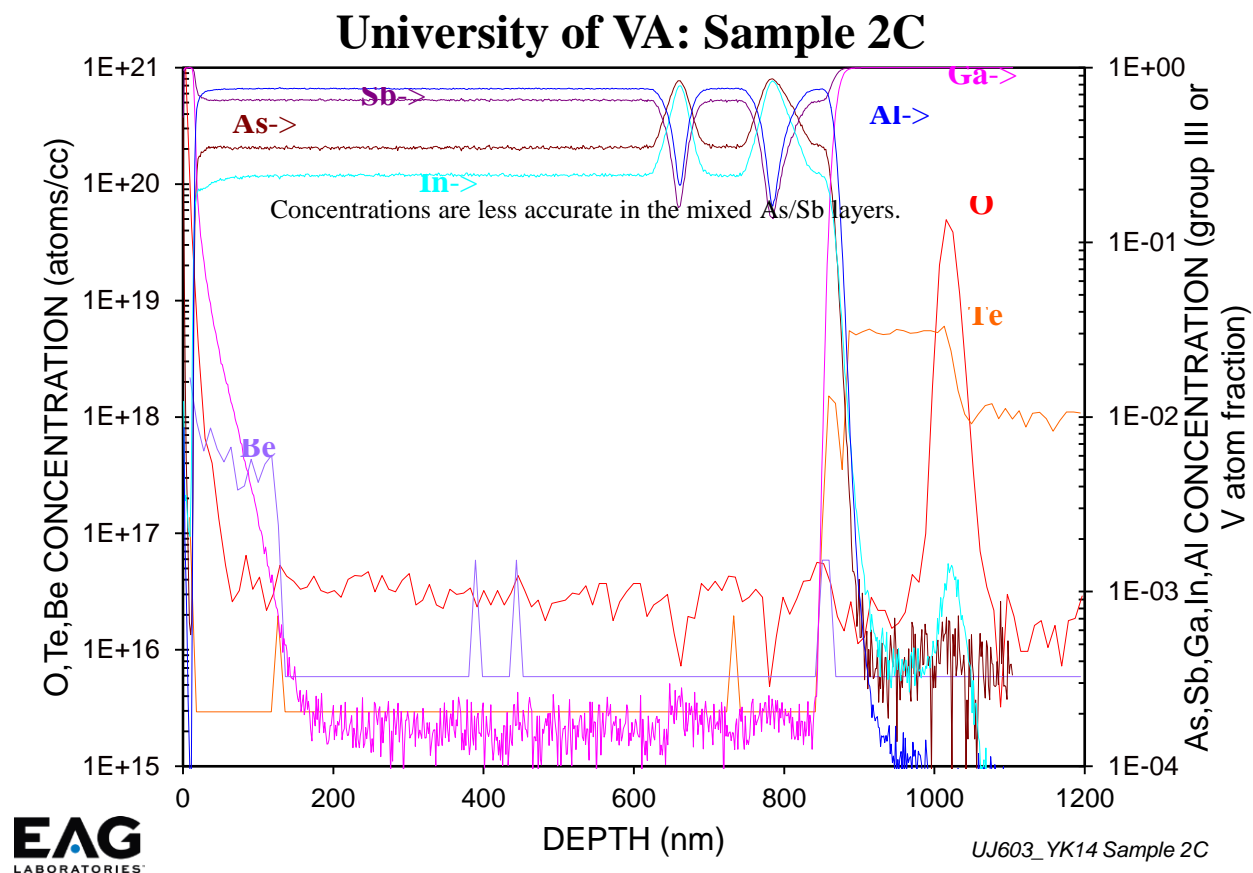
Figure 6-4: SIMS analysis of tunneling staircase structure.

6.3 Measurements

Figure 6-5 shows the dark current, photocurrent, and gain for a 100 μm-diameter two-step tunneling device measured at room temperature. The gain has been normalized according to the control structure, which features no constriction points. Gain is low until the reverse bias is about 2 V, at which point the energy band structure has bent sufficiently as to begin electron trapping, thus enhancing tunneling and gain, with a peak gain of ~28 at a reverse bias of ~3 V.
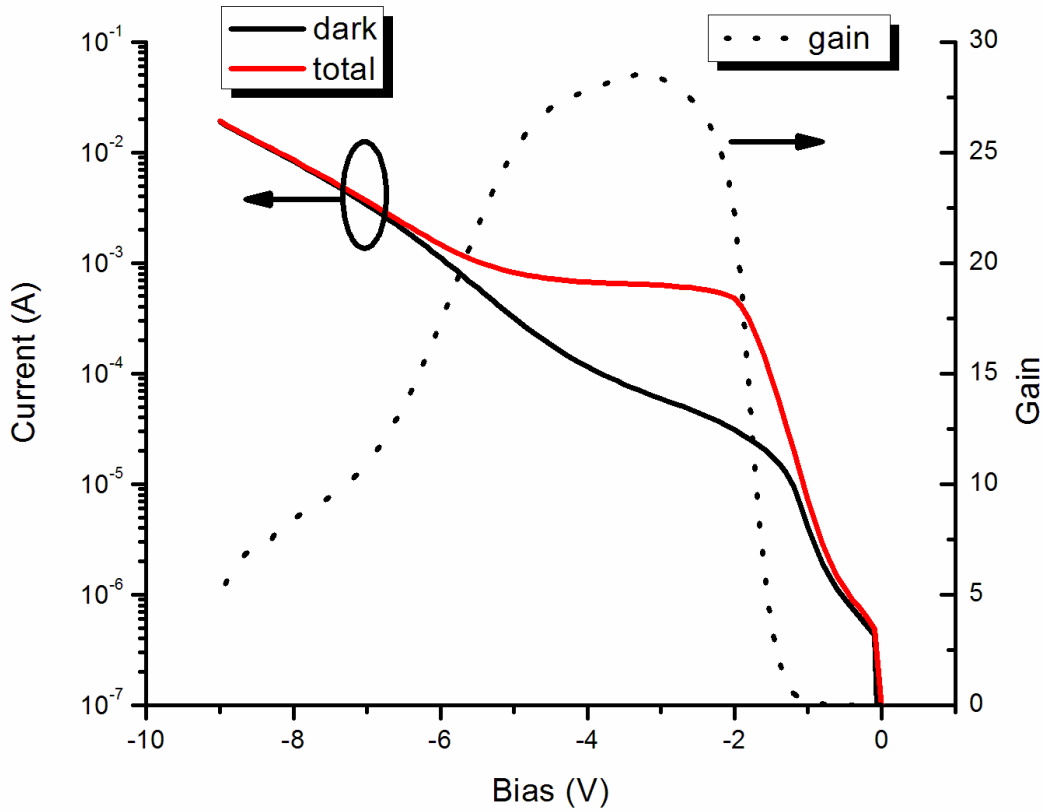
Figure 6-5: Current and gain versus bias for a 100 μm-diameter device measured at 300K. Gain is normalized to a control homojunction structure with no constrictions in bandgap, represented by the dotted line and corresponding to the right y-axis.

While the gain is high, the 3 dB bandwidth is relatively small, around a few MHz, as is shown in Figure 6-6. However, as the band structure tilts the electric field further, the bandwidth sharply increases, as electrons escape the trap more easily. However, this reduces the tunneling gain in the device; thus, gain decreases with increasing bandwidth.
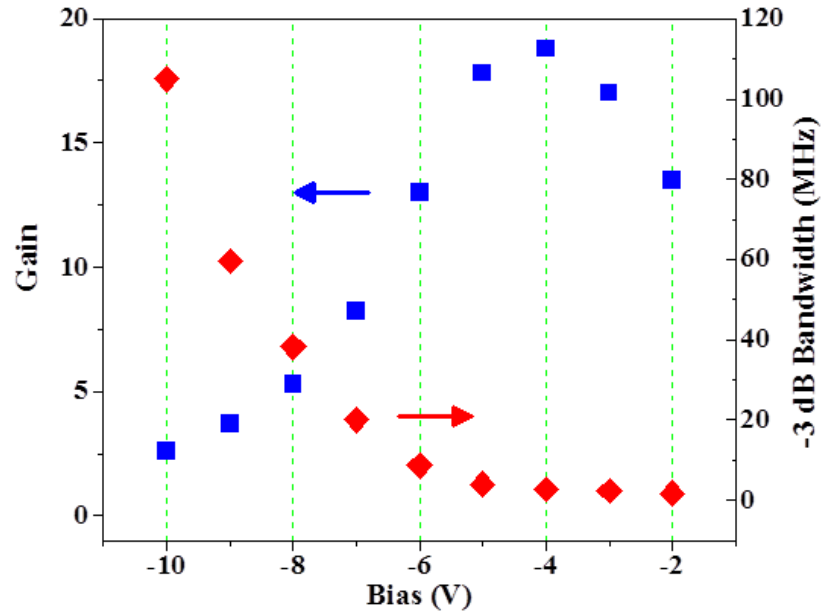
Figure 6-6: -3 dB bandwidth and gain versus bias for a 100 μm-diameter device measured at 300K.

In addition to gain and bandwidth measurements, we also measured the noise power and calculated their base noise power using the control structure, shown in Figure 6-7. For reverse biases below -7 V, the noise power was limited by the device bandwidth. However, once the bandwidth reached 10 MHz, we observed an excess noise factor of ~1.8, which is close to the excess noise of a device fabricated from a low k-value material.
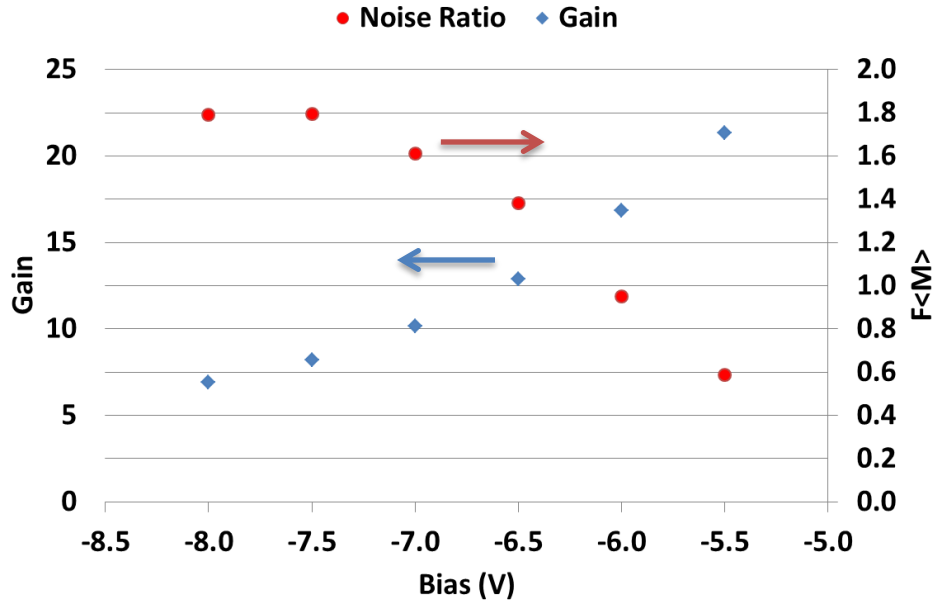
Figure 6-7: Excess noise and gain versus bias for a 100 μm-diameter device measured at 300K under illumination from a CW 542 nm laser. Noise power is limited by bandwidth for reverse biases above -7 V.

In order to test whether the source of the gain was truly from electron trapping and tunneling, rather than more established mechanisms, such as bias-dependent responsivity, we designed a structure with an increased rate of compositional grating, with the intent of increasing the electron trapping in the first step by forming a sharper well. The conceptual band diagram of this structure is shown in Figure 6-8(a). More trapped electrons would create a higher electric field and therefore more enhanced tunneling and higher gain. The gain versus bias results for the enhanced tunneling, two-step staircase device are shown in Figure 6-8(b) and Figure 6-9. Again, gain is low until the reverse bias is about 2 V, at which point the energy band structure has bent sufficiently as to begin electron trapping, thus enhancing tunneling and gain. Where the initial two-step device peaked at a gain of ~27, however, measurements of the more steeply graded structure show gain of 200x at only 2.5 V reverse bias, ~8x lower bias than the best competing III-V low-noise avalanche detectors [88].
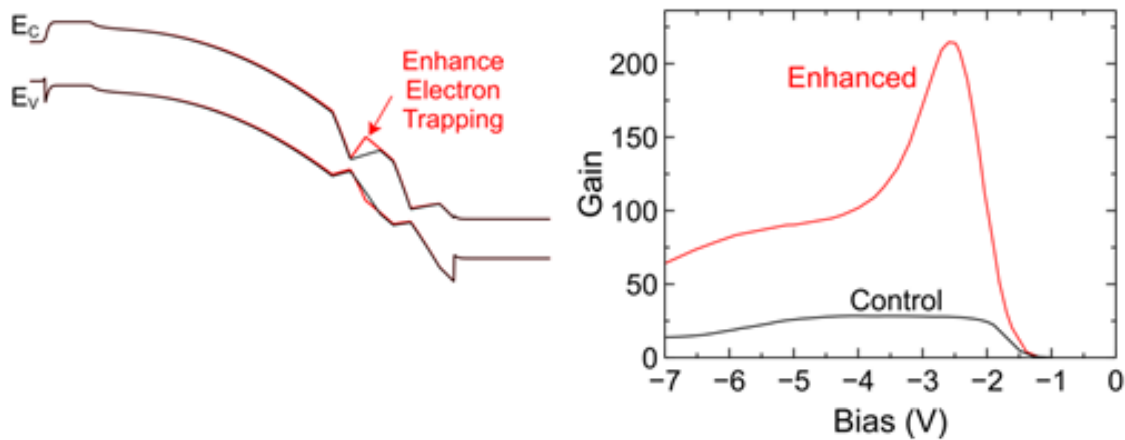
Figure 6-8: (a) Conceptual band diagram depicting sharpening of grading rate which enhanced the gain at low biases, as shown by (b) gain versus bias curve for control and enhanced gain tunneling staircase photodetector.
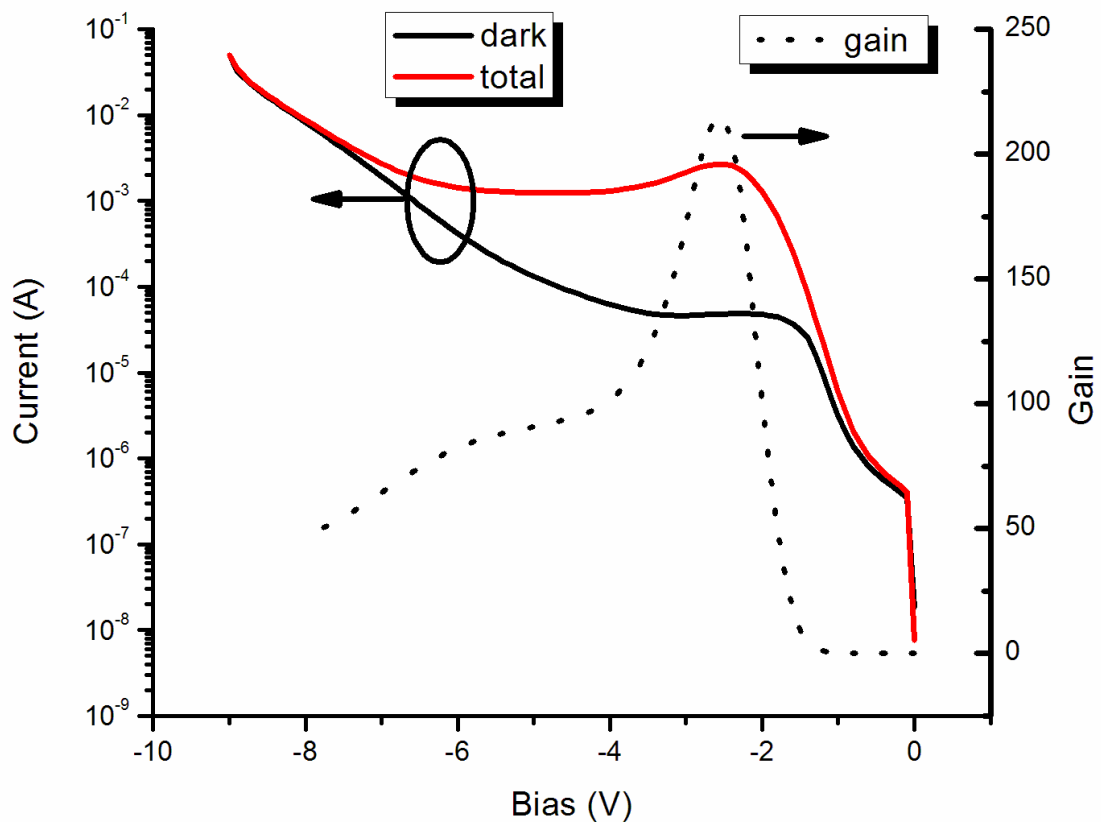
Figure 6-9: Current and gain versus bias for a 100 μm-diameter enhanced-tunneling device measured at 300K. Gain is normalized to a control homojunction structure with no constrictions in bandgap.

As with the initial two-step device, the bandwidth increases sharply with decreasing gain, as is shown in Figure 6-10. However, with the enhanced gain from the sharp grading, the 3-dB bandwidth was significantly lower than that of the original two-step structure. However, the device remains viable for certain imaging applications which do not require high speeds, and benefit from a power-efficient, low operating voltage and low noise, such as night vision imaging systems.
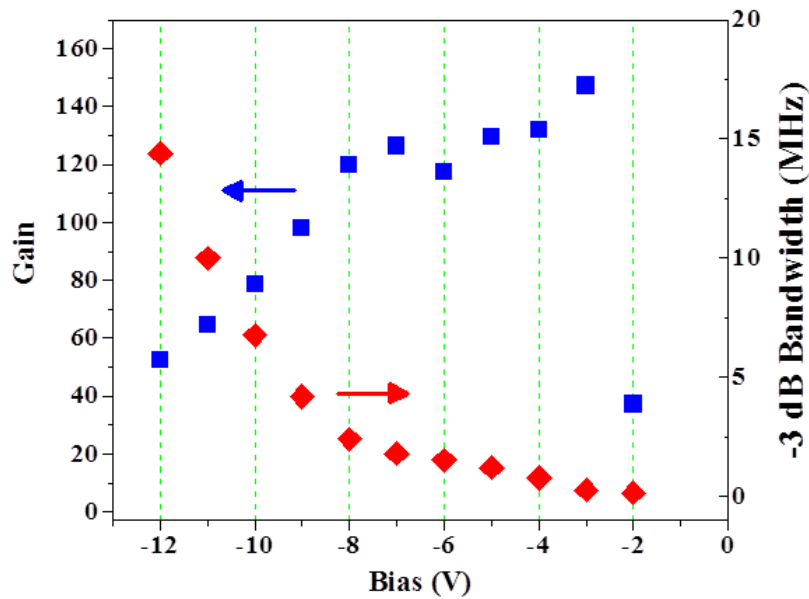
Figure 6-10: -3 dB bandwidth and gain versus bias for a 100 um-diameter enhanced tunneling device measured at 300K. As gain increases, bandwidth decreases sharply, due to a slow electron trap-and-release mechanism.

6.4 Chapter Summary

While the device fabricated was not a true two-step staircase APD, the device developed has beneficial applications in night vision imaging systems. Current microchannel plate architectures are bulky, power inefficient, noisy, and require hundreds of volts of bias, opening a market for a solid-state replacement. Preliminary noise and bandwidth measurements show very low excess multiplication noise for the tunneling staircase detector, as well as sufficient bandwidths for imaging applications, in a device which is simple to grow and is fabricated similarly to an InAs APD.

Chapter 7 Digital Alloy Studies

7.1 Introduction

As is noted earlier in this dissertation, previous growths of the AlInAsSb material lattice-matched to GaSb substrates have only reached aluminum concentrations as high as 30% as a random alloy, due to the presence of a wide miscibility gap. While Vaughn et. al. were able to use a digital alloy technique to push Al fractions up as high as 40%, photoluminescence was only observed in Al concentrations as high as 30%. Our collaborators at the University of Texas, however, were able to grow AlInAsSb quaternary material, lattice-matched to GaSb for Al fractions ranging from 0% to 80%.

In our studies of the quaternary material, we became interested not only in the material composition, but the digital nature of the material. Since the material is grown digitally, it consists of thin, repeating layers of binary materials. This repetition could be important for two reasons. First, the layers are so thin that they may produce a dead-space effect, squeezing the variance in gain to reduce excess noise. Second, the heterojunctions at the interfaces between the binary monolayers could act like small I^2E devices, providing additional energy to serve as a catalyst for impact ionization.

The $Al_xIn_{1-x}As_ySb_{1-y}$ quaternary material may be a low-noise material inherently, but its low noise may also exist because it is a digital alloy. If that is true, then another digital alloy may also exhibit lower noise than its random counterpart, thus giving rise to a new, universally-applicable method to suppress the excess noise of a material. Since the quaternary AlInAsSb material cannot be grown randomly at high aluminum concentrations, we elected to perform digital alloy versus random alloy studies on two different materials systems: InGaAs and AlInAs. By using

these materials systems, we hoped to develop a model for understanding the varying properties

of digital and random alloys, eventually drawing conclusions for the AlInAsSb quaternary.

7.2 Digital vs. Random InGaAs
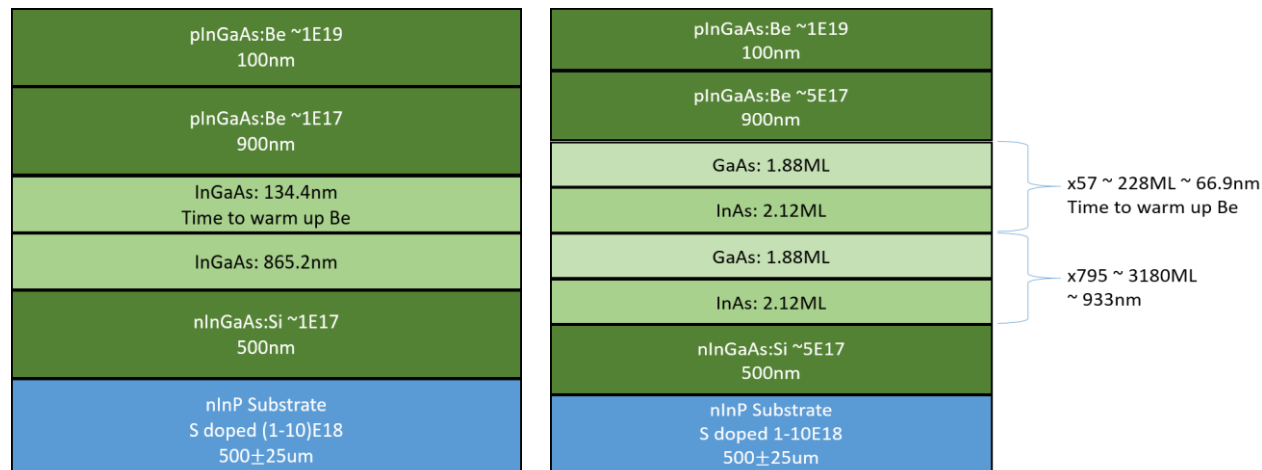
Figure 7-1: Initial structure design for InGaAs p-i-n homojunction detectors, with 4 ML digital structures and a random-alloy control structure.

Initially, our collaborators grew two structures: a random alloy control structure and a digital alloy structure with a period of 4 monolayers, in other words, about 2 monolayers each of GaAs and InAs. Both structures consisted of 900 nm p+ regions, followed by 1000 nm i-regions, and 500 nm n+ regions, on an n-InP substrate, as shown in Figure 7-1. While the current-voltage curves and capacitance-voltage measurements for this growth showed working APDs, the dark current, due primarily to tunneling, limited the noise measurement, as is shown in Figure 7-2 and Figure 7-3.

Since our noise figure meter is only accurate for dark currents up to 10 μA, noise measurements can only be performed up to gains that produce dark currents below this threshold. For the 4 ML device in particular, the device was not able to even reach a gain of 2 before the dark current went above 10 μA. Thus, we initially focused on longer digital alloy periods. In the next iteration of the design, we focused on digital alloy periods of 8 monolayers and 10 monolayers, as shown in Figure 7-4. I fabricated and tested the noise of these devices, but again

the dark current in the devices limited the gain I could measure, and thus the excess noise, which

prevented a fit to the k-value.
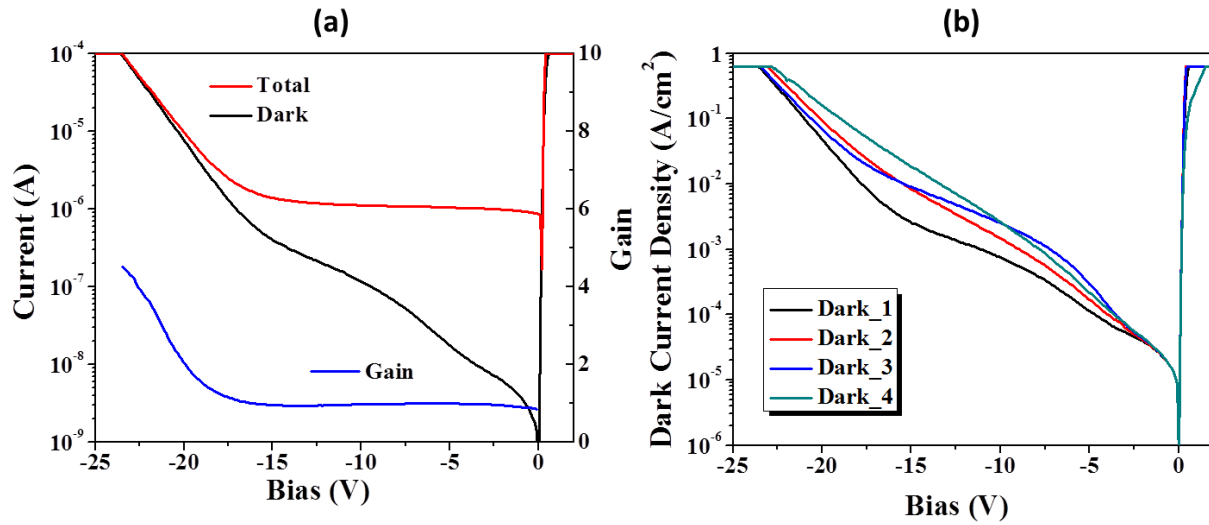
Figure 7-2: InGaAs control: randomly-grown alloy devices measured at 300 K. (a) Typical current versus bias curve for 100 μm diameter device under lamp illumination. Gain calculated from unity gain point of -5 V. (b) Dark current density versus bias for four different 100 μm diameter devices across the chip.
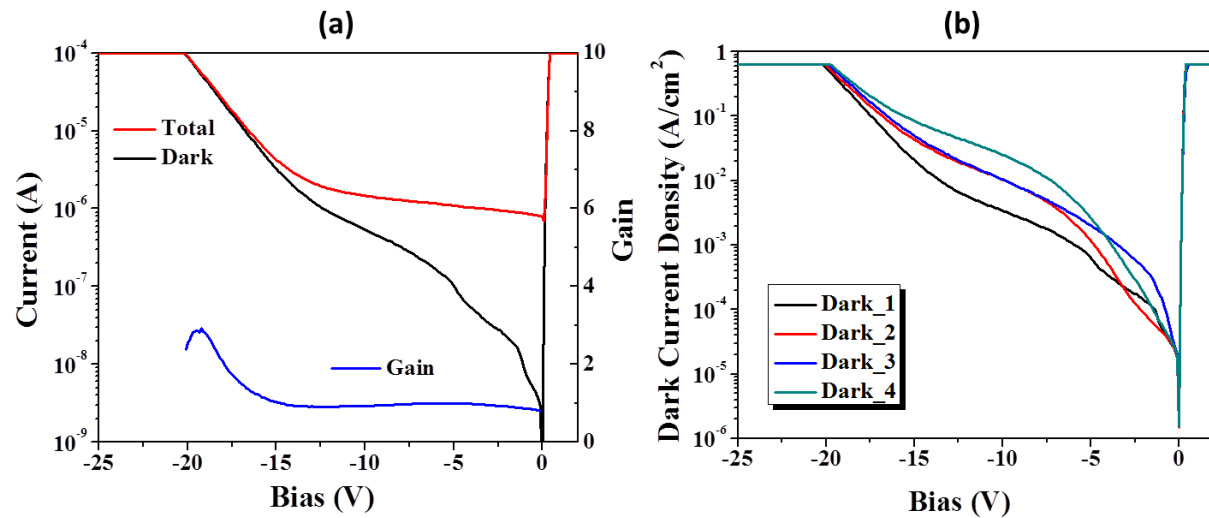
Figure 7-3: InGaAs 4 ML digital alloy devices measured at 300 K. (a) Typical current versus bias curve for 100 μm diameter device under lamp illumination. Gain calculated from unity gain point of -5 V. (b) Dark current density versus bias for four different 100 μm diameter devices across the chip.
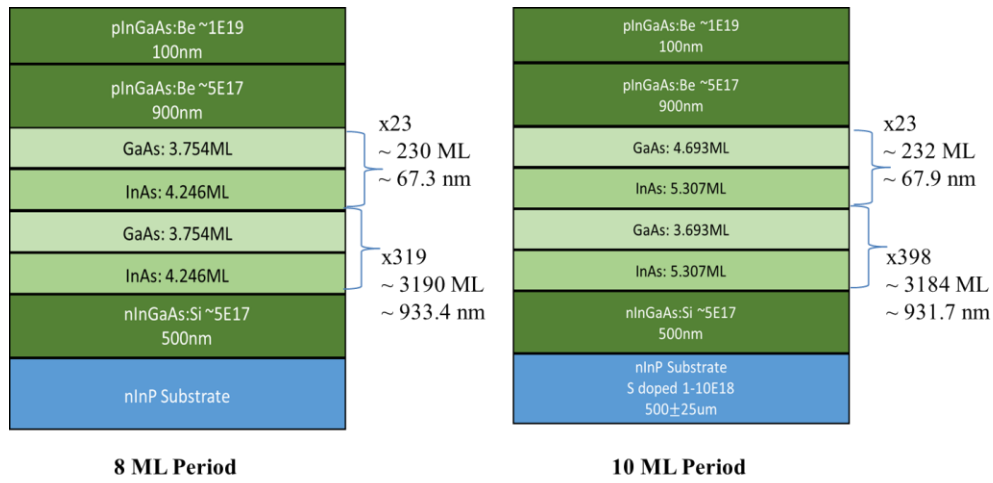
Figure 7-4: Second-iteration structure design for InGaAs p-i-n homojunction detectors, with digital alloy periods of 8 ML and 10 ML, and a random-alloy control structure.
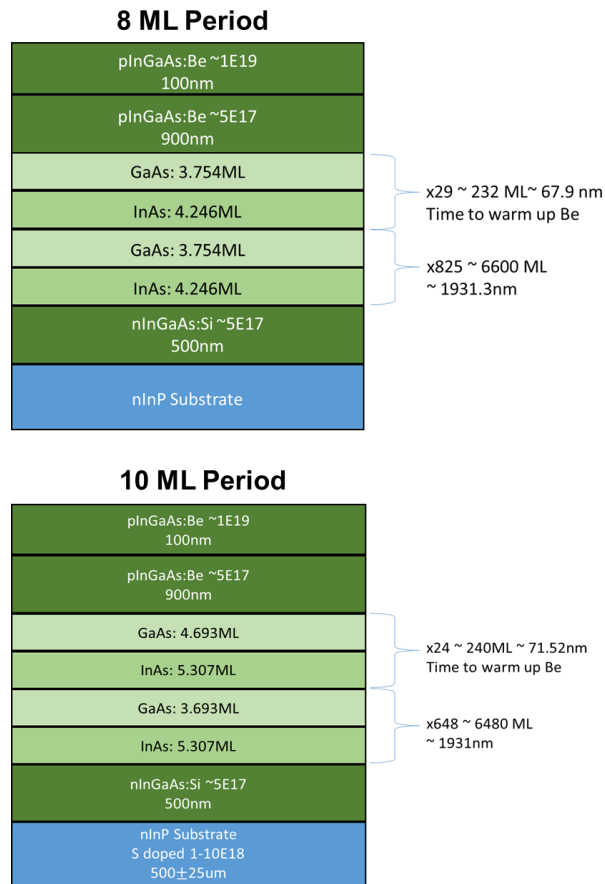
Figure 7-5: Third-iteration structure design for InGaAs p-i-n homojunction detectors, with digital alloy periods of 8 ML and 10 ML, but no random-alloy control structure counterpart. Devices were compared to literature from Y. L. Goh et al. [89]

In our third and final design iteration, we asked our collaborators at the University of Texas to grow a wafer with substantially thicker i-region to mitigate tunneling effects by reducing the electric field. Rather than grow a control structure, however, we elected to compare our results to the findings of Y. L. Goh et al. of the APD group at the University of Sheffield [90]. Ideally, we would have fabricated a 2 μm i-region random alloy homojunction device; however, we were limited by the growth quality of our wafers. As I stated, our noise figure meter fails to accurately measure noise when the dark current of a device exceeds 10 μA. For the initial structures, this dark current cutoff meant devices could be biased to gains of ~2. With the improved structure, however, and the longer i-region, the devices could be pushed to gains of ~3.5 before the dark current exceeded 10 μA, as shown in Figure 7-6.
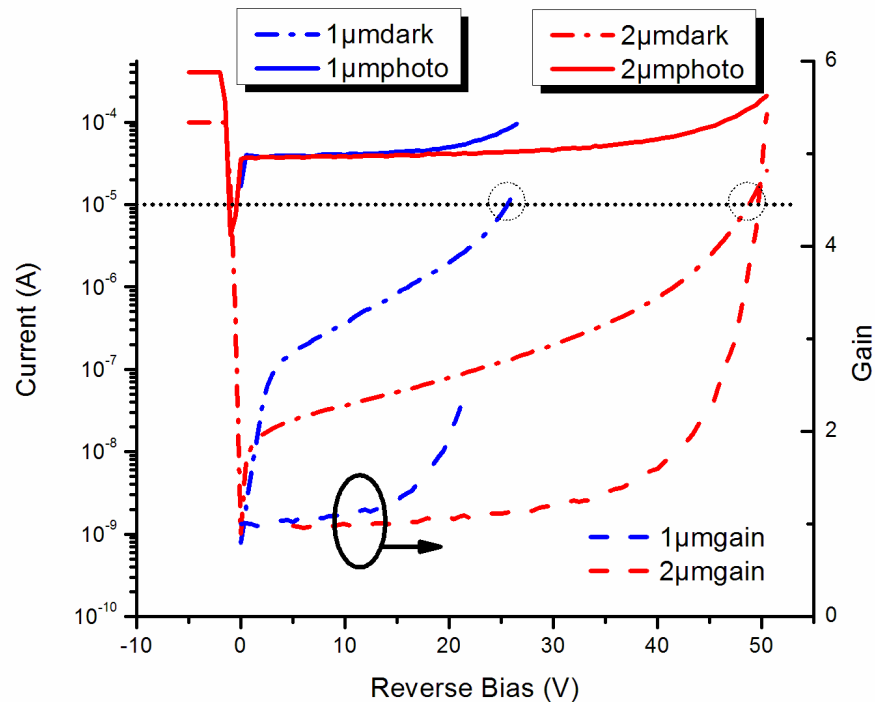
Figure 7-6: Current vs. reverse bias for 1 μm and 2 μm i-region 10 ML digital alloy devices. Blue curves represent devices with 1 μm i-region. Red curves represent devices with 2 μm i-region. Black dashed horizontal line shows dark current cutoff of 10 μA for noise figure meter. All devices measured have a diameter of 30 μm and were measured under lamp illumination at 300 K.

However, excess noise values measured from the InGaAs digital alloy devices did not correspond to lower noise than that of the random alloy InGaAs reported by Y. L. Goh et al., as is shown in Figure 7-7. For this material, the digital alloy appeared to have equal or slightly higher noise than that of the random alloy. This discrepancy may be due in part to the fact that the control devices are reported from literature, and may have shown more similar k-values had they been measured under the same conditions, using the same equipment.
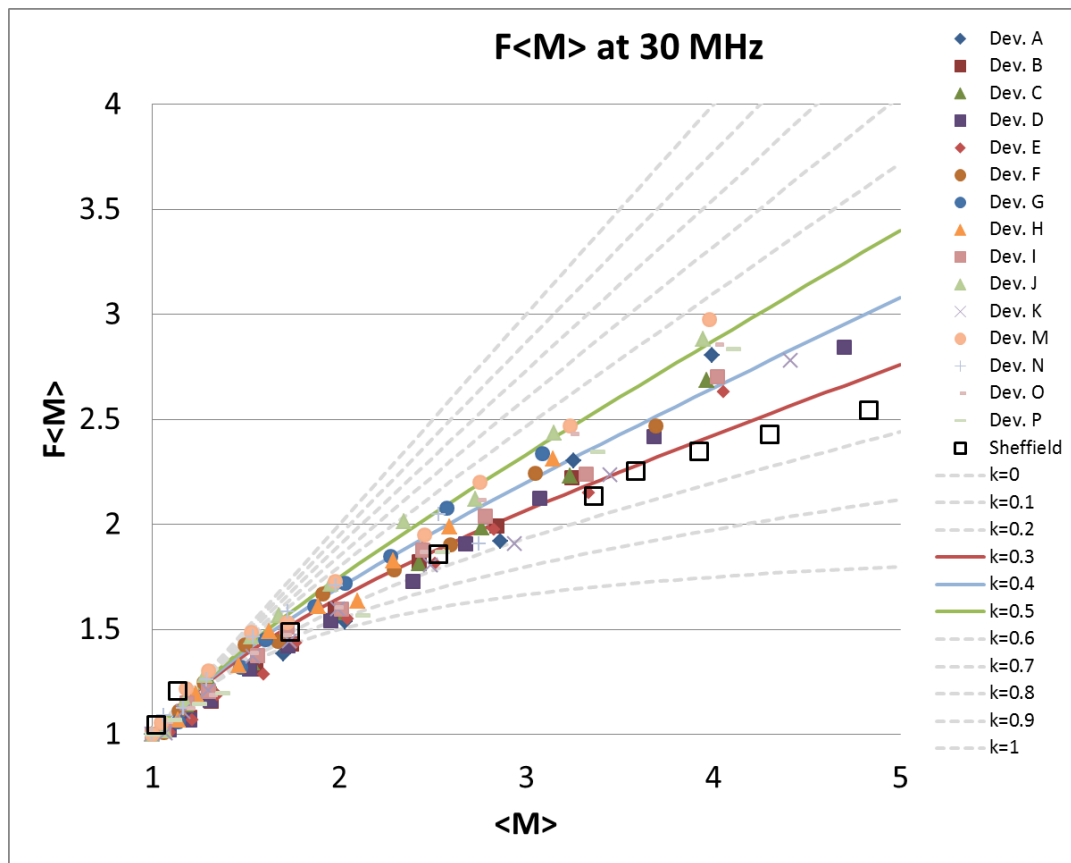
Figure 7-7: Excess noise versus gain for 16 different 30 µm-diameter, 2 µm i-region devices. Symbols "□" represent measurements from Y. L. Goh et al. at Sheffield [90]; all other symbols represent 8 ML digital alloy devices measured.

The quantum efficiency of the digital devices, on the other hand, yielded promising results. Figure 7-8 shows the quantum efficiency of the 8 ML, 10 ML, and control 1 µm i-region devices over a range of wavelengths from the second iteration of growths. Both the 8ML and

10ML digital alloy APDs exhibited higher quantum efficiencies out to longer wavelengths than the random alloy counterpart. Note that that the packaged InGaAs device used for calibration cuts off for wavelengths beyond 1.75 µm. Further investigation of the quantum efficiency will require another type of photodiode for calibration at longer wavelengths. In addition to measuring the quantum efficiency for these devices, we also probed the responsivity of the 1 µm i-region APDs at 2 µm wavelengths. Responsivity was low for the randomly grown 80 µm diameter InGaAs APD, approximately ~0.7 mA/W at unity gain. For the digitally grown APDs, however, the responsivity for 80 µm diameter devices at unity gain was significantly higher, ~5 mA/W for the 8ML devices and ~13 mA/W for the 10ML devices. While this responsivity is still very low, it shows promise for developing digitally-grown InGaAs detectors that can detect to wavelengths of 2 µm, a key wavelength for infrared detection, as many compounds, such as CO_2, have fundamental absorption bands in this wavelength range [91] [92] [93].
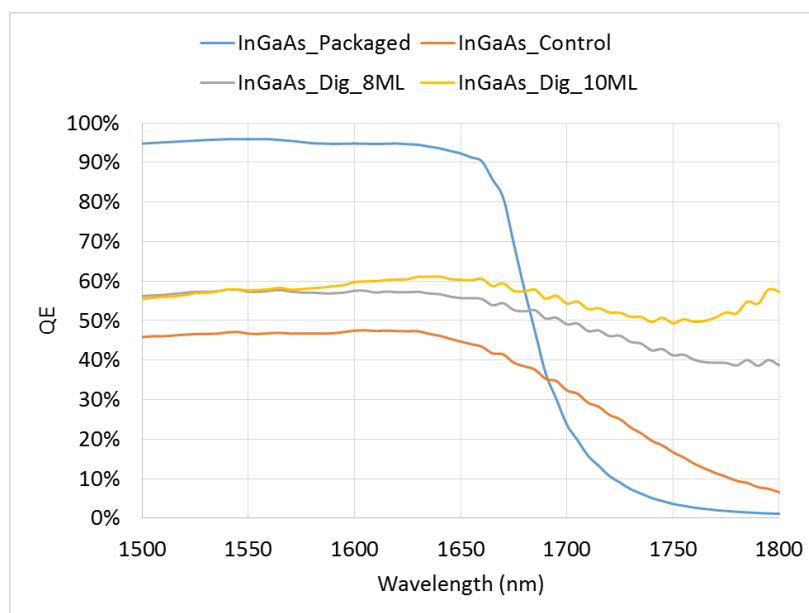
Figure 7-8: Measured external quantum efficiency of InGaAs digitally- and randomly-grown APDs with no anti-reflection coating. All devices have 1 µm i-region. Data was measured with 100 µm diameter devices at 300 K. Note that the packaged InGaAs device used for calibration cuts off for wavelengths beyond 1.75 µm. Further investigation will require another device for calibration for longer wavelengths.

7.3. Digital vs. Random Alloy InAlAs

The structure of the InAlAs structures is shown below. The material was grown digitally by MBE epitaxial growth at the University of Texas by Ann Kathryn Rockwell. Two distinct digital structures were grown – one with a period of 6 monolayers (ML), one with a period of 8 monolayers. To fabricate these devices, I defined circular mesas using a standard photolithography process, and etched using a $H_3PO_4:H_2O_2:H_2O$ (1:1:10) solution. An etching solution of $H_2SO_4:H_2O_2:H_2O$ (1:8:80) was also tested, but gave no significant performance enhancement in dark current or mesa quality. Titanium/gold contacts were deposited using e-beam evaporation. SU-8 was used as a passivation layer on the completed device. Figure 7-9 shows the cross-sectional structure of a device following fabrication.
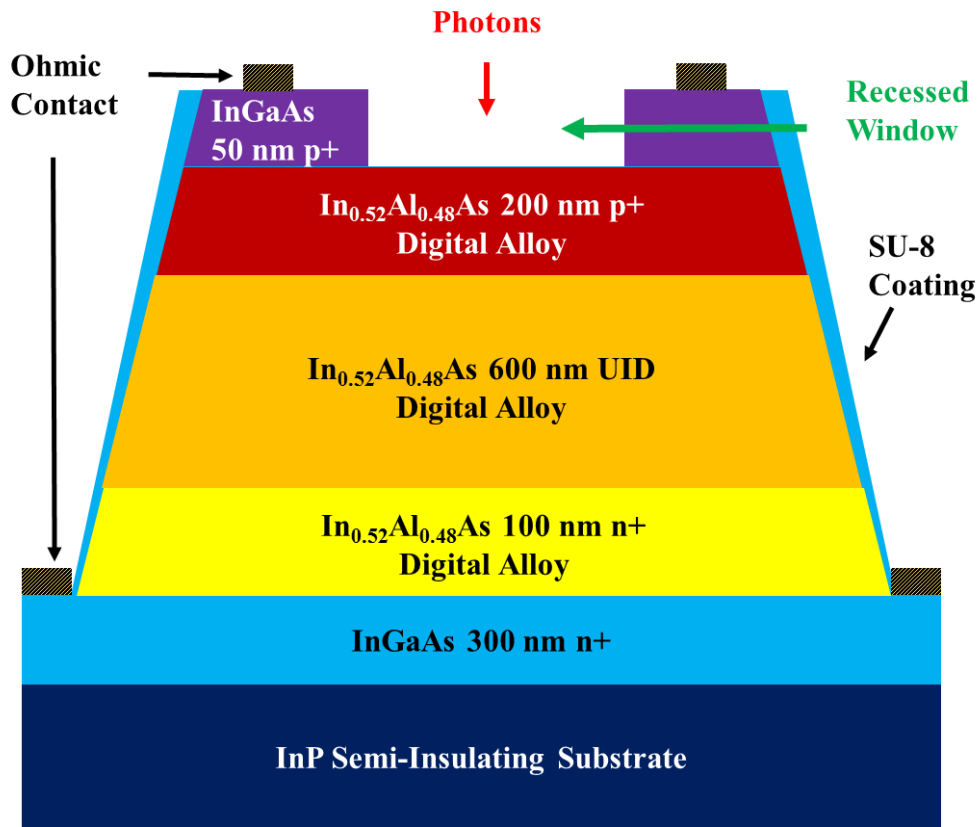
Figure 7-9: Cross-sectional schematic of digitally-grown InAlAs APD.

Figure 7-10 shows the dark current, photocurrent, and gain versus bias for 100 um diameter devices from both the 6 ML and 8 ML alloy structures. Dark current is slightly higher for the 8 ML devices, due perhaps to tunneling effects, but perhaps to effective bandgap, as is explained later in this section. Devices were able to reach gains as high as ~100 and ~87 at breakdown voltages of -34 V and -33 V for the 6 ML and 8 ML devices, respectively.
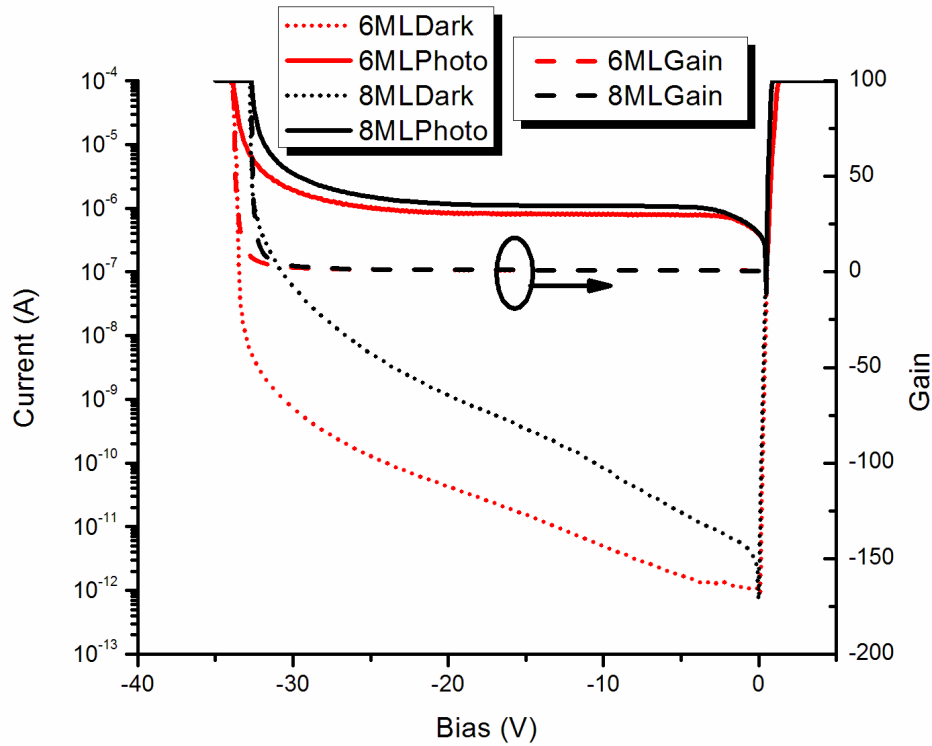
Figure 7-10: Current and gain vs. bias curves for 6 ML and 8 ML digital alloy AlInAs devices. Measured with 100 μm devices at 300K under white lamp illumination.

Next, we measured the noise of both of the digitally-grown devices. Our intent was to compare the noise of these devices to the noise of a control (random alloy) structure using the same noise set up. Typically, we prefer to measure excess noise to gains of at least 10, in order to fit an accurate k-value for the data. The noise values for the 6 ML and 8 ML digitally grown devices are shown in Figure 7-11 and Figure 7-12, plotted with measured noise values for a control device of the same structure according to C. Lenox et al. [20].

While we attempted to measure the noise of the random control devices grown by our collaborators at the University of Texas, we found the noise behaved unexpectedly; the excess noise consistently increased sharply at a gain around 4 or 5. We attempted to reduce the photo noise by measuring with an attenuated laser, thus at a lower light intensity, but this yielded no different results. We recently sent a sample of the control wafer for SIMS analysis, and have ordered a commercially-grown control wafer for fabrication this summer.
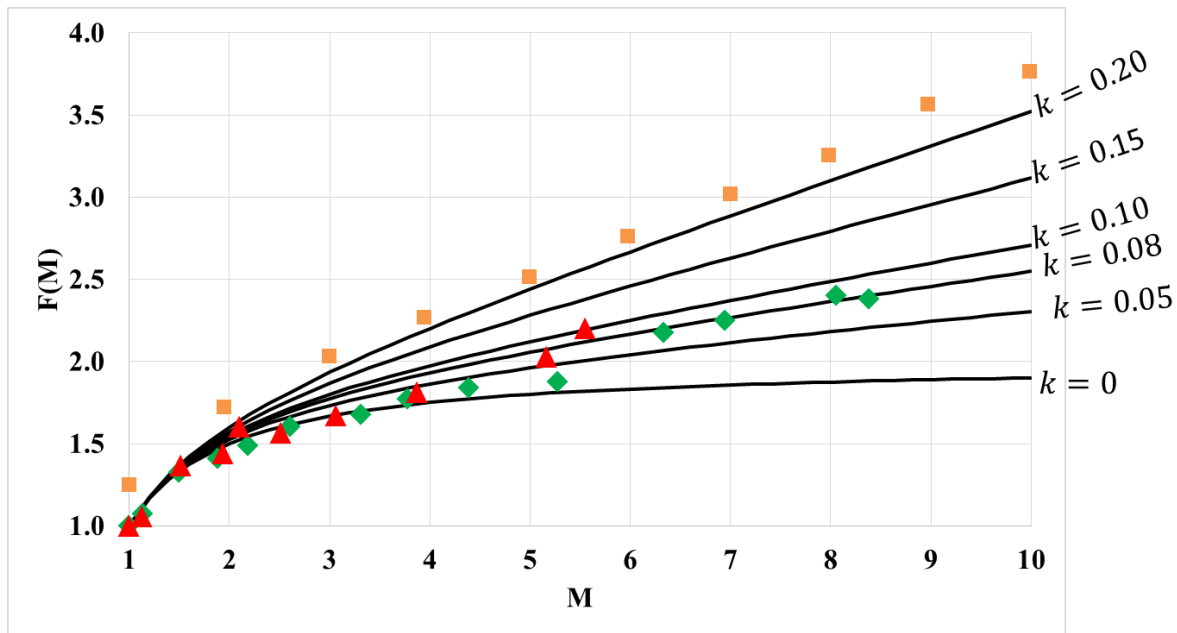
Figure 7-11: Measured excess noise factor versus gain for 6 ML and control AlInAs APDs illuminated with 542 nm CW laser. ▲: 6 ML digital device measured by electrical spectrum analyzer; ◆: 6 ML digital device measured by noise figure meter; ■: randomly grown device from **[20]**.
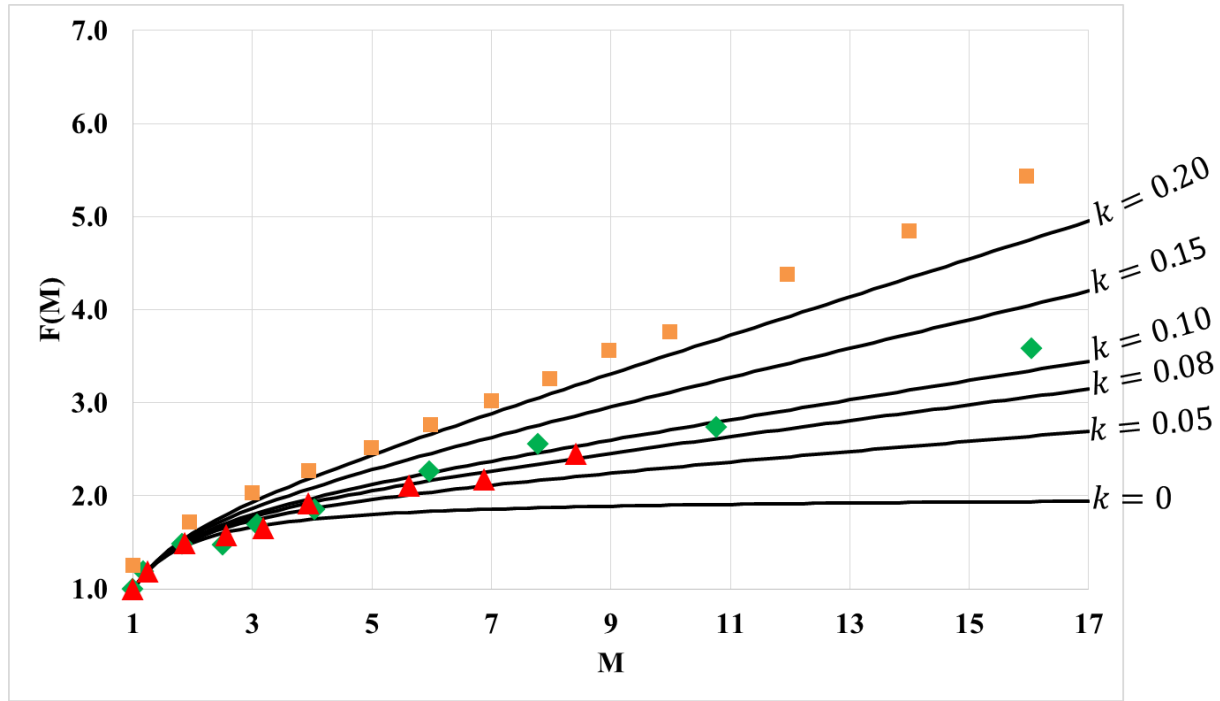
Figure 7-12: Measured excess noise factor versus gain for 8 ML and control AlInAs APDs illuminated with 542 nm CW laser. ▲: 8 ML digital device measured by electrical spectrum analyzer; ♦: 8 ML digital device measured by noise figure meter; ■: randomly grown device from **[20]**.

Figure 7-13 shows the external quantum efficiency as a function of the wavelength of incident light. Note that although the cutoff wavelength of the random alloy AlInAs APD is approximately 850 nm, with a bandgap of 1.46 eV, the cutoff wavelengths of both digitally-grown AlInAs APDs are substantially longer. The 6 ML device has a cutoff wavelength near 950 nm, corresponding to an effective bandgap of ~1.31 eV. The 8 ML device has an even longer cutoff wavelength at 1050 nm, corresponding to an effective bandgap of ~1.13 eV. This "tunable bandgap," where the digital alloy binary repetition rate can be modified to change the effective bandgap of the material, opens the door for studies in the field of effective bandgap engineering. These digital materials can absorb at wavelengths far beyond the cutoff of the random material, while still remaining lattice-matched to an InP substrate. InP is a widely-used

substrate for a wide range of optoelectronic devices, and thus, maintaining a lattice match while pushing to longer wavelength absorption provides a way to trade flexibly between the dark current within a device and the range of wavelengths to which it can respond.
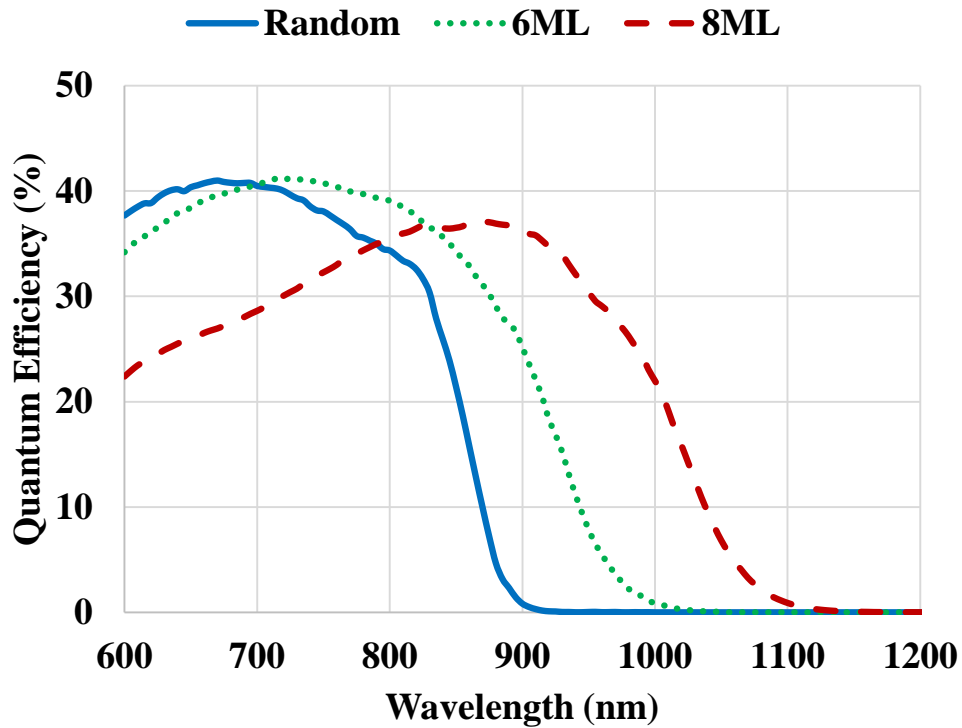

Figure 7-13: Measured external quantum efficiency of AlInAs digitally-grown APDs with no anti-reflection coating. Data was measured with 200 μm diameter APDs at 300 K. The top layer of InGaAs has not been removed for these devices.

7.4. Chapter Summary

We studied two different materials systems that were grown both digitally and randomly by MBE by our collaborators at the University of Texas, in order to determine whether a digitally-grown material inherently has any different characteristics from a random alloy. We saw slightly higher dark currents in the digitally-grown materials than their random counterparts. Additionally, the digitally-grown AlInAs material shows promise for lower noise values than the random alloy devices, though will be a subject of future study. Most notably, however, the detection wavelength range expands for digitally grown alloys, owing perhaps to a quasi-quantum well effect or superlattice structure in the band diagram, pushing detection into the short and mid wave infrared. These wavelengths have applications in the military, medical, industrial, and scientific communities, including temperature sensing, night vision imaging, gas detection, and astronomy.

By allowing a "tunable bandgap," where the thickness of repeating monolayers in a digital alloy can be modified to change the effective bandgap of the material, these digital materials can absorb at wavelengths far beyond the cutoff of the random material. This can be achieved while retaining lattice-match to an InP substrate, a widely-used substrate for optoelectronic devices, giving a flexible trade-off between the device dark current and the range of wavelengths to which it can respond.

Chapter 8 Future Work

8.1 AlInAsSb Device Re-growth

As is discussed in the sections on the $Al_{0.7}In_{0.3}As_{0.3}Sb_{0.7}$ p-i-n homojunction photodiode and the SACM AlInAsSb photodiode, the bandwidths of the devices we have fabricated are RC-limited, particularly by contact resistance. Since GaSb is prone to oxidation, and the wafers in our clean room have been stored on the shelf for over a year, the full thickness of the GaSb has oxidized, potentially due to the formation of lattice-relaxation-induced pin holes during growth. The oxidation has reached the AlInAsSb material, which, because of its aluminum content, is also prone to substantial oxidation. We have proposed the following structures to address this issue.
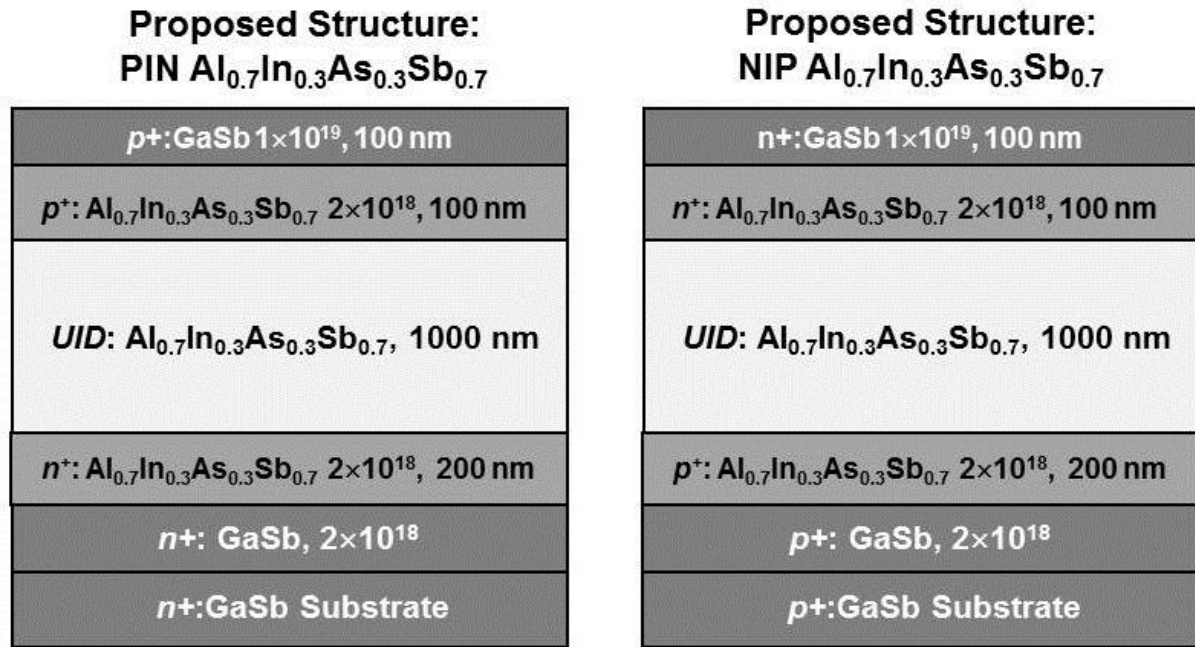
Figure 8-1: Proposed p-i-n and n-i-p $Al_{0.7}In_{0.3}As_{0.3}Sb_{0.7}$ structures for re-growth pending MBE repair at University of Texas.

Figure 8-1 shows the structures for two proposed p-i-n and n-i-p $Al_{0.7}In_{0.3}As_{0.3}Sb_{0.7}$ homojunction devices. One key change from the devices reported in chapter 3 is a thicker GaSb cap layer, which should be less prone to full thickness oxidation. Additionally, the n-i-p structure

can be used to study hole injection multiplication, which would enable determination of the electron and hole impact ionization coefficients, per methods demonstrated repeatedly by the University of Sheffield [94] [95] [96] [97] [98]. These two structures were sent to us in February of this year (2017), but the wafers suffered from poor crystal quality, and thus were insufficient for both bandwidth and noise studies.

Proposed Structure:
PIN $Al_{0.6}In_{0.4}As_{0.4}Sb_{0.6}$

$p+$:GaSb 1×10^{19}, 100 nm
p^+: $Al_{0.6}In_{0.4}As_{0.4}Sb_{0.6}$ 2×10^{18}, 100 nm
UID: $Al_{0.6}In_{0.4}As_{0.4}Sb_{0.6}$, 500 nm
n^+: $Al_{0.6}In_{0.4}As_{0.4}Sb_{0.6}$ 2×10^{18}, 200 nm
$n+$: GaSb, 2×10^{18}
$n+$:GaSb Substrate

Proposed Structure:
PIN $Al_{0.6}In_{0.4}As_{0.4}Sb_{0.6}$

$p+$:GaSb 1×10^{19}, 100 nm
p^+: $Al_{0.6}In_{0.4}As_{0.4}Sb_{0.6}$ 2×10^{18}, 100 nm
UID: $Al_{0.6}In_{0.4}As_{0.4}Sb_{0.6}$, 1500 nm
n^+: $Al_{0.6}In_{0.4}As_{0.4}Sb_{0.6}$ 2×10^{18}, 200 nm
$n+$: GaSb, 2×10^{18}
$n+$:GaSb Substrate

Figure 8-2: Proposed structures for p-i-n homojunction $Al_{0.6}In_{0.4}As_{0.4}Sb_{0.6}$ APDs pending MBE repair.

Figure 8-2 shows the structures for proposed p-i-n homojunction $Al_{0.6}In_{0.4}As_{0.4}Sb_{0.6}$ APDs. Again, the GaSb cap has been modified such that it is 100 nm thick. The $Al_{0.6}In_{0.4}As_{0.4}Sb_{0.6}$ APDs reported in chapter 4 were of particular interest because of their low k-value and dark current. In addition to this, however, we found these devices to reach high gains more consistently than their $Al_{0.7}In_{0.3}As_{0.3}Sb_{0.7}$ counterparts, and also exhibited lower surface leakage. Consequently, we designed these two structures with two different i-region thicknesses, to further our understanding of this material.

Initial SACM Structure (chapter 5)

p+:GaSb 1×10^19, 100 nm
p+: Al_{0.7}In_{0.3}As_{0.3}Sb_{0.7} 2×10^18, 100 nm
p+: Al_xIn_{1-x}Al_yAs_{1-y} x = 0.7 to 0.4, 50 nm
UID: Al_{0.4}In_{0.6}As_{0.6}Sb_{0.4}, 1000 nm
p+: Al_xIn_{1-x}Al_yAs_{1-y} x = 0.4 to 0.7, 50 nm
p: Al_{0.7}In_{0.3}As_{0.3}Sb_{0.7} 1.25×10^17, 150 nm
UID: Al_{0.7}In_{0.3}As_{0.3}Sb_{0.7}, 1000 nm
n+: GaSb, 1×10^18, buffer
n+:GaSb Substrate

Proposed SACM Structure

p+:GaSb 1×10^19, 100 nm	← p-type contact
p+: Al_{0.7}In_{0.3}As_{0.3}Sb_{0.7} 2×10^18, 100 nm	← blocking layer
p+: Al_xIn_{1-x}Al_yAs_{1-y} x = 0.7 to 0.4, 50 nm	← composition grading
UID: Al_{0.4}In_{0.6}As_{0.6}Sb_{0.4}, 1000 nm	absorption layer
p+: Al_xIn_{1-x}Al_yAs_{1-y} x = 0.4 to 0.7, 100 nm	← composition grading
p: Al_{0.7}In_{0.3}As_{0.3}Sb_{0.7} 1.25×10^17, 150 nm	← charge layer
UID: Al_{0.7}In_{0.3}As_{0.3}Sb_{0.7}, 400 nm	multiplication layer
n+: GaSb, 1×10^18, buffer	← n-type contact
n+:GaSb Substrate	

Figure 8-3: Initial SACM structure (see chapter 5) and proposed SACM structure for re-growth pending MBE repair.

Figure 8-3 shows the structure of a proposed SACM APD. This structure is similar to the SACM APD reported in chapter 5, but features a shorter multiplication region, which should improve its bandwidth and gain-bandwidth product. Additionally, the compositional grading layer from 40% to $Al_{0.7}In_{0.3}As_{0.3}Sb_{0.7}$ proposed in the new structure is a half the grading rate, and thus, twice is thickness, of the initial design. This structure is, in fact, a copy of a structure we designed initially during the growth of the first SACM structures, but the crystal quality and GaSb oxidation prevented further study. Another option would be to reduce the absorption layer by half and sacrifice quantum efficiency in the device in order to increase the bandwidth.

Proposed Structure:
100 nm GaSb Contact

$p+$: GaSb 1×10^{19}, 100 nm
p^+: $Al_{0.6}In_{0.4}As_{0.4}Sb_{0.6}$ 2×10^{18}, 200 nm
$n+$:GaSb Substrate

Proposed Structure:
100 nm InGaAs Contact

$p+$: InGaAs 1×10^{19}, 100 nm
p^+: $Al_{0.6}In_{0.4}As_{0.4}Sb_{0.6}$ 2×10^{18}, 200 nm
$n+$:GaSb Substrate

Proposed Structure:
200 nm GaSb Contact

$p+$: GaSb 1×10^{19}, 200 nm
p^+: $Al_{0.6}In_{0.4}As_{0.4}Sb_{0.6}$ 2×10^{18}, 200 nm
$n+$:GaSb Substrate
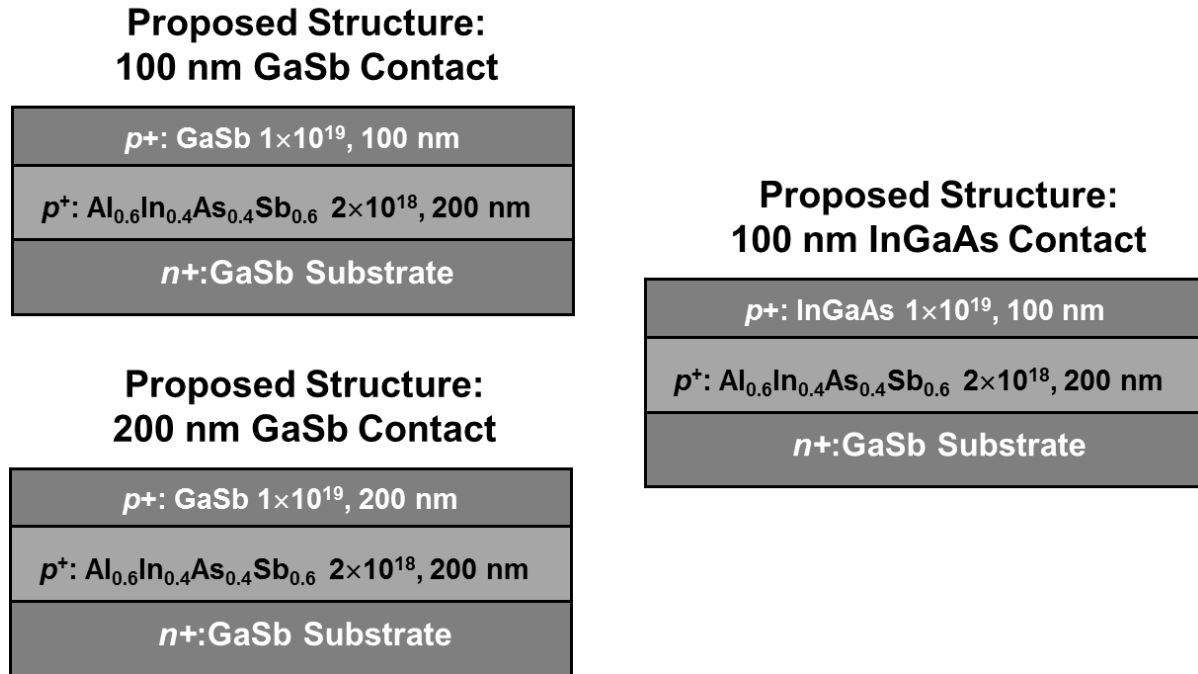
Figure 8-4: Proposed structures for studying and improving contact resistance in AlInAsSb-based devices.

In addition to these devices, we are also interested in improving contact resistance across all our devices. Relevant proposed structures for this are shown in Figure 8-4. These structures could be used to study the metals and alloying techniques that could minimize contact resistance, and thus allow measurements of the transit-time limited bandwidth, with the hope of eventually yielding a gain-bandwidth product that exceeds the current state of the art.

Beyond the re-growth of the digital alloy, we recently contacted a group at the University of Montpellier who published a paper in April 2017 reporting their successful MBE growth of random-alloy AlInAsSb on GaSb substrate [99]. They report photoluminescence spectra measurements for materials with aluminum concentrations as high at 75%. We hope to collaborate with them in the coming months on comparing the digitally-grown alloy to their random alloy. We have proposed the structure in Figure 8-5 to them, and they have agreed to begin growth within the next couple of months.

Proposed Structure:
PIN $Al_{0.6}In_{0.4}As_{0.4}Sb_{0.6}$

p+:GaSb 1×10^{19}, 100 nm
p+: $Al_{0.6}In_{0.4}As_{0.4}Sb_{0.6}$ 2×10^{18}, 100 nm
UID: $Al_{0.6}In_{0.4}As_{0.4}Sb_{0.6}$, 890 nm
n+: $Al_{0.6}In_{0.4}As_{0.4}Sb_{0.6}$ 2×10^{18}, 200 nm
n+: GaSb, 2×10^{18}
n+:GaSb Substrate

Figure 8-5: Proposed structure for random growth at the University of Montpellier.

Future studies may also investigate the receiver sensitivity of the 60% and 70% homojunction AlInAsSb devices at 850 nm, as well as the receiver sensitivity of the SACM devices at 1550 nm. Receiver sensitivity describes the minimum input signal required to produce an output value that satisfies a given signal-to-noise ratio. This figure of merit will help to put into context the quality of the APD, and how compares to APDs currently on the market and under research. We study this by generating a string of random 0s and 1s on a modulated laser. Our detector is then used to convert this optical signal back into an electrical signal, and we use a bit error rate module to detect the number of errors. If the bit error rate is below a given threshold (typically 10^{-9} or 10^{-12}), the signal-to-noise ratio is satisfied for this input power. We then reduce the optical power until the bit error rate is no longer satisfactory. Currently, we are seeking a low-noise transimpedance amplifier that can operate at high bit rates (10 Gbps) to amplify our detected signal so it is readable by the bit error rate module.

8.3 Single Photon Counting

Conventional APDs are operated in linear-mode, biased below the breakdown voltage. By pushing an APD into Geiger mode, the electric field in the device is so high that a single photon can achieve self-sustaining impact ionization and yield detectable gains. In addition to the linear-mode avalanche photodiodes I have discussed thus far in this dissertation, avalanche photodiodes have applications in the single-photon detection, including biological agent and marker detection [100] [101], quantum cryptography [102] [103], and light-detection and ranging (LIDAR) [104] [105] [106] [107], all of which have generated interest in high-speed, single photon detection technologies. While PMTs and superconducting single photon detectors (SSPDs) yield low noise and high sensitivity, there is also a market for single photon avalanche diodes (SPADs), which have a distinct advantage in cost, size, and a broad range of wavelength operations [108].

Future studies of the AlInAsSb materials system may lead to the development of single-photon counting APDs based on designs using these materials. The quaternary materials system enjoys the advantages of low noise detection across a broad spectrum of wavelengths, and additionally a direct-bandgap that yields higher quantum efficiencies. Initial testing is currently underway to determine the dark count probability and breakdown probability of some of our homojunction detectors.

Publications

Journal

M. Ren, S. J. Maddox, **M. E. Woodson**, Y. Chen, S. R. Bank, and J. C. Campbell, "Characteristics of $Al_xIn_{1-x}As_ySb_{1-y}$ (x:0.3~0.7) Avalanche Photodiodes," J. Lightwave Tech. vol. 35, no. 12, pp. 2380-2384.

M. Woodson, M. Ren, S. Maddox, Y. Chen, S. Bank, and J. Campbell, "Low-noise AlInAsSb avalanche photodiode," Appl. Phys. Lett. 108, 081102 (2016).

M. Ren, S. Maddox, **M. Woodson**, Y. Chen, S. Bank, and J. Campbell, "$Al_xIn_{1-x}As_ySb_{1-y}$ separate absorption, charge, and multiplication avalanche photodiodes," Appl. Phys. Lett. 108, 191108 (2016).

M. Ren, S. Maddox, Y. Chen, **M. Woodson**, J. Campbell and S. Bank, "$Al_xIn_{1-x}As_ySb_{1-y}$ /GaSb staircase avalanche photodiode," Appl. Phys. Lett. 108, 081101 (2016).

Conference

M. Ren, Y. Yuan, A. H. Jones, S. J. Maddox, **M. Woodson**, S. Bank, and J. Campbell, "Operation Stability Study of AlInAsSb Avalanche Photodiodes," in IEEE Photonics Conference (2017) (submitted May 2017).

M. Ren, S. J. Maddox, **M. Woodson**, Y. Chen, S. Bank, and J. Campbell, "$Al_xIn_{1-x}As_ySb_{1-y}$ Separate Absorption, Charge, and Multiplication Avalanche Photodiodes," in IEEE Photonics Conference (2016).

M. Ren, S. J. Maddox, **M. Woodson**, Y. Chen, S. Bank, and J. Campbell, "$Al_xIn_{1-x}As_ySb_{1-y}$ Separate Absorption, Charge, and Multiplication Avalanche Photodiodes," in Device Research Conference (2016).

M. Ren, S. J. Maddox, **M. Woodson**, Y. Chen, S. Bank, and J. Campbell, "Low-Noise High-Gain Tunneling Staircase Photodetector," in Device Research Conference (2016).

M. Ren, S. J. Maddox, **M. Woodson**, Y. Chen, S. Bank, and J. Campbell, "Low Excess Noise $Al_xIn_{1-x}As_ySb_{1-y}$ (x: 0.3~0.7) Avalanche Photodiodes," in Conference on Lasers and Electro-Optics, OSA Technical Digest (2016) (Optical Society of America, 2016)

S. Maddox, M. Ren, **M. Woodson**, S. Bank, and J. C. Campbell, "Recent progress in avalanche photodiodes for sensing in the IR spectrum," in SPIE (May 26, 2016).

M Ren, S Maddox, Y Chan, **M Woodson**, S Bank, JC Campbell, "Low excess noise AlInAsSb staircase avalanche photodiode," Device Research Conference (DRC), (2015).

A. Beling, J. Campbell, K. Li, Q. Li, Y. Wang, **M. Woodson**, X. Xie Z. Yang, "High-Power Photodiodes for Analog Applications," IEICE TRANSACTIONS on Electronics Vol.E98-C No.8 pp.764-768.

Works Cited

[1]   K. G. Coffman and A. M. Odlyzko, "Growth of the Internet," AT&T Labs - Research, 2001.

[2]   J. Murphy and M. Roser, "Internet," Our World in Data, 2015. [Online]. Available: https://ourworldindata.org/internet/. [Accessed 2017].

[3]   J. C. Campbell, "Recent advances in avalanche photodetectors," *IEEE Journal of Selected Topics in Quantum Electronics,* vol. 10, no. 4, pp. 777-787, 2004.

[4]   N. Bertone and W. R. Clark, "Avalanche photodiode arrays provide versatility in ultrasensitive applications," *Laser Focus World,* vol. 43, no. 9, pp. 69-73, 2007.

[5]   P. Mitra, J. D. Beck, M. R. Skokan, J. E. Robinson, J. Antoszewski, K. J. Winchester, A. J. Keating, T. Nguyen, K. K. M. Silva, C. A. Musca, J. M. Dell and L. Farone, "Adaptive focal plane array (AFPA) technologies for integrated infrared microsystems," in *SPIE*, 2006.

[6]   A. Tosi, N. Calandri, M. Sanzaro and F. Acerbi, "Low-noise, low-jitter, high detection efficiency InGaAs/InP single-photon avalanche diode," *IEEE Journal of Selected Topics in Quantum Electronics,* vol. 20, no. 6, 2014.

[7]   X. Jiang, M. Itzler, K. O'Donnell, M. Entwistle, M. Owens, K. Slomkowski and S. Rangwala, "InP-Based Single-Photon Detectors and Geiger-Mode APD Arrays for Quantum Communications Applications," *IEEE Journal of Selected Topics in Quantum Electronics,* vol. 21, no. 3, 2015.

[8]   R. B. Emmons, "Avalanche photodiode frequency response," *Journal of Applied Physics,* vol. 38, 1967.

[9]   K. Watase, "What is the Micro PMT?," Hamamatsu Photonics, May 2013. [Online]. Available: https://www.hamamatsu.com/us/en/community/optical_sensors/articles/intro_to_uPMT/index.html. [Accessed 2017].

[10]   K. Watase, "Photomultiplier Tubes: µPMT is key to high-performance portable devices," *Laser Focus World,* 1 5 2013.

[11]   "Optical Sensors," Hamamatsu, 2017. [Online]. Available: https://www.hamamatsu.com/us/en/product/category/3100/index.html.

[12]   "Detectors," Thor Labs, 2017. [Online]. Available:
       https://www.thorlabs.com/navigation.cfm?guide_id=36.

[13]   R. J. McIntyre, "Multiplication noise in uniform avalanche diodes," *IEEE Transactions on Electron Devices,* vol. 13, no. 1, pp. 164-168, 1966.

[14]   W. Sun, Theoretical Study and Monte Carlo Simulation of III-V Compound Low-Noise Photodiodes, Charlottesville: University of Virginia, 2014.

[15]   K. Li, S. Plimmer, J. David, R. Tozer, G. Rees, P. Robson, C. Button and J. Clark, "Low avalanche noise characteristics in thin InP p/sup +/-i-n/sup +/ diodes with electron initiated multiplication," *IEEE Photonics Technology Letters,* vol. 11, no. 3, pp. 364-366, 199.

[16]   P. Yuan, C. C. Hansing, K. A. Anselm, C. V. Lenox, H. Nie, J. A. L. Holmes, B. .. Streetman and J. C. Campbell, "Impact ionization characteristics of III-V semiconductors for a wide range of multiplication region thicknesses," *IEEE Journal of Quantum Electronics,* vol. 36, no. 2, pp. 198-204, 2000.

[17]   K. F. Li, D. S. Ong, J. P. R. David, G. J. Rees, R. C. Tozer, P. N. Robson and R. Grey, "Avalanche multiplication noise characteristics in thin GaAs p -i-n diodes," *IEEE Trans. Electron Dev.,* vol. 45, no. 10, pp. 2102-2107, 1998.

[18]   C. Hu, K. A. Anselm, B. G. Streetman and J. C. Campbell, "Noise characteristics of thin multiplication region GaAs avalanche photodiodes," *Applied Physics Letters,* vol. 69, no. 24, pp. 3734-3736, 1996.

[19]   D. S. Ong, K. F. Li, G. J. Rees, G. M. Dunn, J. P. R. David and P. N. Robson, "A Monte Carlo investigation of multiplication noise in thin p-i-n GaAs avalanche photodiodes," *IEEE Trans. Electron Dev.,* no. 1804-1810, p. 45, 1998.

[20]   C. Lenox, P. Yuan, H. Nie, O. Baklenov, C. Hansing, J. C. Campbell, J. A. L. Holmes and B. G. Streetman, "Thin multiplication region InAlAs homojunction avalanche photodiodes," *Applied Physics Letters,* vol. 73, 1998.

[21]   M. A. Saleh, M. M. Hayat, P. O. Sotirelis, A. L. Holmes, J. C. Campbell, B. Saleh and M. Teich, "Impact-ionization and noise characteristics of thin III-V avalanche photodiodes," *IEEE Trans. Electron Devices,* vol. 48, pp. 2722-2731, 2001.

[22]   B. K. Ng, J. P. R. David, R. C. Tozer, G. J. Rees, Y. Feng, J. H. Zhao and M. Weiner, "Nonlocal effects in thin 4H-SiC UV avalanche photodiodes," *IEEE Trans. Electron.*

Devices, vol. 50, pp. 1724-1732, 2003.

[23] P. Yuan, S. Wang, X. Sun, X. G. Zheng, J. A. L. Holmes and J. C. Campbell, "Avalanche photodiodes with an impact-ionization-engineered multiplication region," *IEEE Photonics Technology Letters,* vol. 12, pp. 1370-1372, 2000.

[24] S. Wang, R. Sidhu, X. G. Zheng, X. Li, X. Sun, J. A. L. Holmes and J. C. Campbell, "Low-noise avalanche photodiodes with graded impact-ionization-engineered multiplication region," *IEEE Photonics Technology Letters,* vol. 13, pp. 1346-1348, 2001.

[25] S. Wang, F. Ma, X. Li, R. Sidhu, X. G. Zheng, X. Sun, J. A. L. Holmes and J. C., "Ultra-low noise avalanche photodiodes with a "centered-well" multiplication region," *IEEE Journal of Quantum Electronics,* vol. 39, pp. 375-378, 2003.

[26] S. M. Sze and K. K. Ng, Physics of Semiconductor Devices (3rd Ed.), New York: Wiley, 2007.

[27] L. J. J. Tan, D. S. G. Ong, J. S. Ng, C. H. Tan, S. K. Jones, Y. Qian and J. P. R. David, "Temperature Dependence of Avalanche Breakdown in InP and InAlAs," *IEEE Journal of Quantum Electronics,* vol. 46, no. 8, 2010.

[28] A. N. Semenov, V. A. Solov'ev, B. Y. Meltser, Y. V. Terent'ev, L. G. Prokopova and S. V. Ivanov, "Molecular beam epitaxy of AlInAsSb alloys near the miscibility gap boundary," *Journal of Crystal Growth,* vol. 278, pp. 203-208, 2005.

[29] W. L. Sarney, S. P. Svensson, D. Wang, D. Donetsky, G. Kipshidze, L. Shterengas, Y. Lin and G. Belenky, "AlInAsSb for M-LWIR detectors," *Journal of Crystal Growth,* vol. 425, pp. 357-359 , 2015.

[30] G. Belenky, D. Wang, Y. Lin, D. Donetsky, G. Kipshidze, L. Shterengas, D. Westerfeld, W. L. Sarney and S. P. Svensson, "Metamorphic InAsSb/AlInAsSb heterostructures for optoelectronic applications," *Applied Physics Letters,* vol. 102, 2013.

[31] S. J. Maddox and B. S. R, "Broadly Tunable AlInAsSb Digital Alloys," *Journal of Crystal Growth & Design,* vol. 16, no. 7, pp. 3582-3586, 2016.

[32] L. G. Vaughn, L. R. Dawson, E. A. Pease, L. F. Lester, H. Xu, Y. Jiang and A. L. Gray, in *SPIE*, 2005.

[33] O. Dier, C. Lin, M. Grau and M.-C. Amann, "Selective and non-selective wet-chemical etchants for GaSb-based materials," *Semiconductor Science and Technology,* vol. 19, no. 11, 2004.

[34]   F. Ma, X. Li, J. C. Campbell, J. D. Beck, C.-F. Wan and M. A. Kinch, "Monte Carlo
        simulations of Hg0.7Cd0.3TeHg0.7Cd0.3Te avalanche photodiodes and resonance
        phenomenon in the multiplication noise," *Applied Physics Letters,* vol. 83, 2003.

[35]   C. K. Chia, "Numerical simulation of impact ionization in Ge/AlxGa1-xAs avalanche
        photodiodes," *Applied Physics Letters,* vol. 97, no. 7, 2010.

[36]   G. M. Dunn, R. Ghin, G. J. Reese, J. P. R. David, S. Plimmer and D. C. Herbert, "Monte
        Carlo simulation of high-field transport and impact ionization in AlGaAs p+in+ diode,"
        Semiconductor Sci. Technol., vol. 14, pp. 994-1000, 1999.

[37]   G. M. Dunn, G. J. Reese, J. P. R. David, S. Plimmer and D. C. Herbert, "Monte Carlo
        simulation of impact ionization and current multiplication in short GaAs p+in+ diodes,"
        Semiconductor Sci. Technol., vol. 12, pp. 111-120, 1997.

[38]   F. Ma, Monte Carlo Simulation of Gain, Noise, and Speed of Low-Noise and High-Speed
        Avalanche Photodiodes, Austin: University of Texas, 2003.

[39]   L. D. Keldysh, "Kinetic theory of impact ionization in semiconductors," *Soviet Phys.
        JETP,* vol. 37, no. 10, 1960.

[40]   F. Capasso, Tsang, W. T and G. F. Williams, "Staircase Solid-state Photomultipliiers and
        Avalanche Photodiodes with Enhanced Ionization Rates Ratio," *IEEE Transitions on
        Electron Devices,* 1982.

[41]   F. Capasso, "Avalanche Photodiodes with Enhanced Ionization Rates Ratio: Towards a
        Solid State Photomultiplier," *IEEE Transitions on Nuclear Science,* vol. 30, no. 1, pp.
        424-428, 1983.

[42]   M. Teich, K. Matsuo and B. E. A. Saleh, "Excess noise factors for conventional and
        superlattice avalanche photodiodes and photomultiplier tubes," *IEEE Journal of Quantum
        Electronics,* vol. 22, no. 8, pp. 1184-1193, 1986.

[43]   G. Ripamonti, F. Capasso, A. L. Hutchinson, D. J. Muehlner, J. F. Walker and R. J.
        Malik, "Realization of a staircase photodiode: Towards a solid-state photomultiplier,"
        Nuclear Instruments and Methods in Physics Research, vol. 288, no. 1, pp. 99-103, 1990.

[44]   M. Toivonen, A. Salokatve, M. Hovinen and M. Pessa, "GaAs/AlGaAs delta-doped
        staircase avalanche photodiode with separated absorption layer," *Electronics Letters,* vol.
        28, no. 1, 1992.

[45]   J. Bude and K. Hess, "Thresholds of impact ionization in semiconductors," *Journal of*

Applied Physics, vol. 72, 1992.

[46]   J. Xie, S. Xie, R. C. Tozer and C. H. Tan, "Excess Noise Characteristics of Thin AlAsSb APDs," *IEEE Transactions on Electron Devices,* vol. 59, no. 5, pp. 1475-1479, 2012.

[47]   R. D. Baertsch, "Noise and multiplication measurements in InSb avalanche photodiodes," *Journal of Applied Physics,* vol. 38, p. 4267, 1967.

[48]   K. Matsuo, M. C. Teich and B. E. A. Saleh, "Noise properties and time response of the staircase avalanche photodiode," *Journal of Lightwave Technologies,* vol. 3, no. 6, pp. 1223-1231, 1985.

[49]   F. Ma, S. Wang and J. C. Campbell, "Shot Noise Suppression in Avalanche Photodiodes," *Physics Review Letters,* vol. 95, 2005.

[50]   J. Campbell, S. Chandrasekhar, W. Tsang, G. Qua and B. Johnson, "Multiplication noise of wide-bandwidth InP/InGaAsP/InGaAs avalanche photodiodes," *Journal of Lightwave Technology,* vol. 7, no. 3, pp. 473-478, 1989.

[51]   Y. Okuto and C. R. Crowell, "Ionization coefficients in semiconductors: A nonlocalized property," *Physical Review B,* vol. 10, no. 10, 1974.

[52]   D. A. Ramirez, M. M. Hayat, A. S. Huntington and G. M. Williams, "Non-Local Model for the Spatial Distribution of Impact Ionization Events in Avalanche Photodiodes," *IEEE Photonics Technology Letters,* vol. 26, no. 1, pp. 25-28, 2014.

[53]   B. Yang, J. D. Schaub, S. M. Csutak, D. L. Rogers and J. C. Campbell, "10-Gb/s All-Silicon Optical Receiver," *IEEE Photonics Technology Letters,* vol. 15, no. 5, pp. 745-747, 2003.

[54]   M. Yang, K. Rim, D. L. Rogers, J. D. Schaub, J. J. Welser, D. M. Kuchta, D. C. Boyd, F. Rodier, P. A. Rabidoux, J. T. Marsh, A. D. Ticknor, Q. Yang, A. Upham and S. C. Ramac, "A high-speed, high-sensitivity silicon lateral trench photodetector," *IEEE Electron Device Letters ,* vol. 23, no. 7, pp. 395-397, 2002.

[55]   C. A. Amiento and S. H. Grooves, "Impact ionization in (100)-, (110)-, and (111)-oriented InP avalanche photodiodes," *Applied Physics Letters,* vol. 43, no. 2, 1983.

[56]   L. W. Cook, G. E. Bulman and G. E. Stillman, "Electron and hole ionization coefficients in InP determined by photomultiplication measurements," *Applied Physics Letters,* vol. 40, no. 7, 1982.

[57]   N. Li, R. Sidhu, X. Li, F. Ma, X. Zheng, S. Wang, G. Karve, S. Demiguel, J. Archie L. Holmes and Joe C. Campbell, "InGaAs/InAlAs avalanche photodiode with undepleted absorber," *Applied Physics Letters,* vol. 82, 2003.

[58]   S. J. Maddox, W. Sun, Z. Lu, H. P. Nair, J. C. Campbell and S. R. Bank, "Enhanced low-noise gain from InAs avalanche photodiodes with reduced dark current and background doping," *Applied Physics Letters,* vol. 101, 2012.

[59]   A. R. J. Marshall, C. H. Tan, M. J. Steer and J. P. R. David, "Extremely Low Excess Noise in InAs Electron Avalanche Photodiodes," *IEEE Photonics Technology Letters,* vol. 21, no. 13, pp. 866-868, 2009.

[60]   C. H. Tan and S. Xie, "AlAsSb Avalanche Photodiodes With a Sub-mV/K Temperature Coefficient of Breakdown Voltage," *IEEE Journal of Quantum Electronics,* vol. 47, no. 11, pp. 1391-1395, 2011.

[61]   Y. Kang, H.-D. Liu, M. Morse, M. J. Paniccia, M. Zadka, S. Litski, G. Sarid, A. Pauchard, Y.-H. Kuo, H.-W. Chen, W. S. Zaoui, J. E. Bowers, A. Beling, D. C. McIntosh, X. Zheng and J. C. Campbell, "Monolithic germanium/silicon avalanche photodiodes with 340 GHz gain–bandwidth product," *Nature Photonics,* vol. 3, pp. 59-63, 2009.

[62]   K. Ikossi, M. Foldenberg and J. Mittereder, "Metallization options and annealing temperatures for low contact resistance ohmic contacts to n-type GaSb," *Solid-State Electronics,* vol. 46, no. 10, pp. 1627-1631, 2002.

[63]   Y. Mizokawa, O. Komoda and S. Miyase, "Long-time air oxidation and oxide-substrate reactions on GaSb, GaAs and GaP at room temperature studied by X-ray photoelectron spectroscopy," *Thin Solid Films,* vol. 156, no. 1, pp. 127-143, 1988.

[64]   Z. Y. Liu, B. Hawkins and T. Kuech, "Chemical and structural characterization of GaSb(100) surfaces treated by HCl-based solutions and annealed in vacuum," *Journal of Vacuum Science and Technology B,* vol. 21, no. 1, 2003.

[65]   T. M. Tran, S. K. Patra, M. Breivik and B. O. Fimland, "Plasma-assisted oxide removal from p-type GaSb for low resistivity ohmic contacts," *Journal of Vacuum Science & Technology B, Nanotechnology and Microelectronics: Materials, Processing, Measurement, and Phenomena,* vol. 33, 2015.

[66]   O. Dier, C. Lin, M. Grau and M.-C. Amann, "Selective and non-selective wet-chemical etchants for GaSb-based materials," *Semiconductor Science and Technology,* vol. 19, no. 11, 2004.

[67]   Y. Kang, Z. Huang, Y. Saado, J. Campbell, A. Pauchard, J. Bowers and M. Paniccia, "High Performance Ge/Si Avalanche Photodiodes Development in Intel," in *Optical Fiber Communication Conference/National Fiber Optic Engineers Conference*, 2011.

[68]   N. Duan, T. Liow, A. Lim, L. Ding and G. Q. Lo, "310 GHz gain-bandwidth product Ge/Si avalanche photodetector for 1550 nm light detection," *Optics Express,* vol. 20, no. 10, pp. 11031-11036, 2012.

[69]   C. Y. Park, K. S. Hyun, S. K. Kang, M. K. Song, T. Y. Yoon, H. M. Kim, H. M. Park, S. C. Park, Y. H. Lee, C. Lee and J. B. Yoo, "High-performance InGaAs/InP avalanche photodiode for a 2.5 Gb s-1 optical receiver," *Optical and Quantum Electronics,* vol. 5, no. 553-559, p. 27, 1995.

[70]   G. Hasnain, W. Bi, S. Song, J. Anderson, N. Moll, C.-Y. Su, J. Hollenhorst, N. Baynes, I. Athroll, S. Amos and R. Ash, "Buried-mesa avalanche photodiodes," *IEEE Journal of Quantum Electronics ,* vol. 34, no. 12, pp. 2321-2326, 1998.

[71]   M. A. Itzler, K. K. Loi, S. McCoy, N. Codd and N. Komaba, "Manufacturable planar bulk-InP avalanche photodiodes for 10 Gb/s applications," in *LEOS '99 IEEE Lasers and Electro-Optics Society 12th Annual Meeting*, San Francisco, 1999.

[72]   M. Nada, Y. Muramoto, H. Yokoyama, T. Ishibashi and H. Matsuzaki, "Triple-mesa Avalanche Photodiode With Inverted P-Down Structure for Reliability and Stability," *Journal of Lightwave Technologies,* vol. 32, no. 8, pp. 1543-1548, 2014.

[73]   G. S. Kinsey, J. C. Campbell and A. G. Dentai, "Waveguide avalanche photodiode operating at 1.55 μm with a gain–bandwidth product of 320 GHz," *IEEE Photonics Technology Letters,* vol. 13, pp. 842-844, 2001.

[74]   E. Yagyu and e. al., "Recent advances in AlInAs avalanche photodiodes," *Proc. Opt. Fiber Commun.,* pp. 145-147, 2007.

[75]   T. Nakata and e. al., "An ultra high speed waveguide avalanche photodiode for 40 Gb s−1 optical receiver," *Proc. 27th European Conference on Optical Communications,* pp. 564-565, 2001.

[76]   A. Rouvie and e. al., "High gain bandwidth product over 140 GHz planar junction AlInAs avalanche photodiodes," *IEEE Photonics Technology Letters,* vol. 20, pp. 455-457, 2008.

[77]   K. Makita, T. Nakata, I. Watanabe and K. Taguchi, "High-frequency response limitation of high performance InAlGaAs/InAlAs superlattice avalanche photodiodes," *Electronics*

Letters, vol. 35, pp. 2228-2229, 1999.

[78]   M. Hayashi and e. al., "Microlens-integrated large-area InAlGaAs–InAlAs superlattice APDs for eye-safety 1.5 µm wavelength optical measurement use," *IEEE Photonics Technology Letters,* vol. 10, pp. 576-578, 1998.

[79]   J. C. Campbell, W. T. Tsang, G. J. Qua and B. C. Johnson, "High-speed InP/InGaAsP/InGaAs avalanche photodiodes grown by chemical beam epitaxy," *IEEE Journal of Quantum Electronics,* vol. 24, pp. 496-500, 1988.

[80]   N. Yasuoka, H. Kuwatsuka and M. Makiuchi, "Large multiplication-bandwidth products in APDs with a thin InP multiplication layer," in *Proc. 16th IEEE Annual Meeting of LEOS*, 2003.

[81]   W. R. e. a. Clark, "Reliable, high gain–bandwidth product InGaAs/InP avalanche photodiodes for 10 Gb s−1 receivers," *Proc. Opt. Fiber Commun.,* vol. 1, pp. 96-98, 1999.

[82]   D. S. e. a. Franco, "High-performance InGaAs–InP APDs on GaAs.," *IEEE Photonics Technology Letters,* vol. 82, pp. 873-874, 2005.

[83]   C. e. a. Lenox, "Resonant-cavity InGaAs–InAlAs avalanche photodiodes with gain–bandwidth product of 290 GHz," *IEEE Photonics Technology Letters,* vol. 11, pp. 1162-1164, 1999.

[84]   H. Liu, H. Pan, C. Hu, D. McIntosh, Z. Lu, J. C. Campbell, Y. Kang and M. Morse, "Avalanche photodiode punch-through gain determination through excess noise analysis," *Journal of Applied Physics,* vol. 106, 2009.

[85]   P. P. Webb, R. J. McIntyre and J. Conradi, "Properties of avalanche photodiodes," *RCA Review,* vol. 35, 1974.

[86]   V. M. Robbins, T. Wang, K. F. Brennan, K. Hess and G. E. Stillman, "Electron and hole impact ionization coefficients in (100) and in (111) Si," *Journal of Applied Physics,* vol. 58, 1985.

[87]   J. P. R. David and C. H. Tan, "Material Considerations for Avalanche Photodiodes," *IEEE Journal of Selected topics in quantum electronics,* vol. 14, no. 4, 2008.

[88]   W. Sun, Z. Lu, X. Zheng, J. C. Campbell, S. J. Maddox, H. P. Nair and S. Bank, "High-Gain InAs Avalanche Photodiodes," *IEEE Journal of Quantum Electronics,* vol. 49, no. 2, pp. 154-161, 2013.

[89]   Y. L. Goh, J. S. Ng, C. H. Tan, W. K. Ng and J. P. R. David, "Excess Noise Measurement
       in In0.53Ga0.47As," *IEEE Photonics Technology Letters,* vol. 17, no. 11, pp. 2412-2414,
       2005.

[90]   Y. L. Goh, J. S. Ng, C. H. Tan, W. K. Ng and J. P. R. David, "Excess Noise Measurement
       in 0.53Ga0.47As," *IEEE Photonics Technology Letters,* vol. 17, no. 11, pp. 2412-2414,
       2005.

[91]   G. L. Sentu, X. X. Xia, Q. C. Sun, J. S. Pelc, M. M. Fejer, Q. Zhang and J. W. Pan,
       "Upconversion single photon detection near 2μm," *Optics Letters,* vol. 28, 2013.

[92]   M. R. McCurdy, Y. Bakhirkin, G. Wysocki, R. Lewicki and F. K. Tittel, "Recent
       advances of laser-spectroscopy-based techniques for applications in breath analysis,"
       Journal of Breath Research, vol. 1, no. 1, 2007.

[93]   G. Ehret, C. Kiemle, M. Wirth, A. Amediek, A. Fix and S. Houweling, "Space-borne
       remote sensing of CO2, CH4, and N2O by integrated path differential absorption lidar: a
       sensitivity analysis," *Applied Physics B,* vol. 90, no. 3, pp. 593-608, 2008.

[94]   J. Xie, S. Xie, R. C. Tozer and C. H. Tan, "Excess Noise Characteristics of Thin AlAsSb
       APDs," *IEEE Transactions on Electron Devices,* vol. 59, no. 5, pp. 1475-1479, 2012.

[95]   J. E. Green, W. S. Loh, A. R. J. Marshall, B. K. Ng, R. C. Tozer, J. P. R. David, S. I.
       Soloviev and P. M. Sandvik, "Impact Ionization Coefficients in 4H-SiC by Ultralow
       Excess Noise Measurement," *IEEE Transactions on Electron Devices,* vol. 59, no. 4, pp.
       1030-1036, 2012.

[96]   J. S. L. Ong, J. S. Ng, A. B. Krysa and J. P. R. David, "Impact Ionization Coefficients in
       Al0.52In0.48P," *IEEE Electron Device Letters,* vol. 32, no. 11, pp. 1528-1530, 2011.

[97]   A. R. J. Marshall, P. Vines, P. J. Ker, J. P. R. David and C. H. Tan, "Avalanche
       Multiplication and Excess Noise in InAs Electron Avalanche Photodiodes at 77 K," *IEEE
       Journal of Quantum Electronics,* vol. 47, no. 6, pp. 858-864, 2011.

[98]   J. S. Ng, C. H. Tan, J. P. R. David, G. Hill and G. J. Rees, "Field dependence of impact
       ionization coefficients in In0.53Ga0.47As," *IEEE Transactions on Electron Devices,* vol.
       50, no. 4, pp. 901-905, 2003.

[99]   J. Tournet, Y. Rouillard and E. Tournié, "Growth and characterization of AlInAsSb layers
       lattice-matched to GaSb," *Journal of Crystal Growth,* 2017.

[100] G. A. Wilson and J. Brady, "Design considerations and signal processing algorithms for

laser-influenced fluorescence airborne pathogen sensors," in *SPIE*, 2004.

[101] L. Pasquardini and e. al., "SPAD aptasensor for the detection of circulating protein biomarkers," *Biosensors and Bioelectronics,* vol. 68, pp. 500-507, 2015.

[102] N. Gisin, G. Ribordy, W. Tittel and H. Zbinden, "Quantum cryptography," *Rev. Mod. Phys.,* vol. 74, no. 1, p. 145, 2002.

[103] A. Trifonov, D. Subacius, A. Berzanskis and A. Zavriyev, "Single photon counting at telecom wavelength and quantum key distribution," *J. Mod. Opt.,* vol. 51, no. 9, pp. 1399-1415, 2004.

[104] G. Buller and A. Wallace, "Ranging and Three-Dimensional Imaging Using Time-Correlated Single-Photon Counting and Point-by-Point Acquisition," *IEEE J. Select. Topics Quantum Electron.,* vol. 13, no. 4, pp. 1006-1015, 2007.

[105] C. Niclass, D. Inoue, H. Matsubara and T. Ichikawa, "Development of automotive LIDAR," *Electronics and Communications in Japan,* vol. 98, no. 5, pp. 28-33, 2015.

[106] M. Ren, X. Gu, Y. Liang, W. Kong, E. Wu, G. Wu and H. Zeng, "Laser ranging at 1550 nm with 1-GHz sine-wave gated InGaAs/InP APD single-photon detector," *Optics Express,* vol. 19, no. 14, 2011.

[107] Y. Liang, J. Huang, M. Ren, B. Feng, X. Chen, E. Wu, G. Wu and H. Zeng, "1550-nm time-of-flight ranging system employing laser with multiple repetition rates for reducing the range ambiguity," *Optics Express,* vol. 22, no. 4, 2014.

[108] P. P. Webb and R. J. McIntyre, "Single photon detection with avalanche photodiodes," *Amer. Phys. Soc. Bull.,* vol. 15, no. 15, p. 813, 1970.

[109] J. Ng, C. Tan, J. David, G. Hill and G. Rees, "Field dependence of impact ionization coefficients in In0.53Ga0.47As," *IEEE Transactions on Electron Devices,* vol. 50, no. 4, pp. 901-905, 2003.

[110] S. Plimmer, J. David, D. Herbert, T.-W. Lee, G. Rees, P. Houston, R. Grey, P. Robson, A. Higgs and D. Wight, "Investigation of impact ionization in thin GaAs diodes," *IEEE Transactions on Electron Devices,* vol. 43, no. 7, pp. 1066-1072, 2002.

[111] R. Ghin, J. P. R. David, M. Hopkinson, M. A. Pate, G. J. Rees and P. N. Robson, "Impact ionization coefficients in GaInP p–i–n diodes," *Applied Physics Letters,* vol. 70, 1997.

[112] A. R. J. Marshall, C. H. Tan, M. J. Steer and J. P. R. David, "Electron dominated impact

ionization and avalanche gain characteristics in InAs photodiodes," *Applied Physics Letters,* vol. 93, 2008.

[113] N. J. Elton, "The Complex Refractive Index and Reflectometry Versus Ellipsometry," Surfoptic, 2007.

[115] C. H. Tan, S. Xie and J. Xie, "Low Noise Avalanche Photodiodes Incorporating a 40 nm AlAsSb Avalanche Region," *IEEE Journal of Quantum Electronics,* vol. 48, no. 1, pp. 36-41, 2012.